A strategy for achieving high performance and durability of double perovskite cathode materials in solid oxide fuel cells

Seonyoung Yoo

Department of Energy Engineering

Graduate school of UNIST

A strategy for achieving high performance and durability of double perovskite cathode materials in solid oxide fuel cells

A dissertation
submitted to the Graduate School of UNIST
in partial fulfillment of the
requirements for the degree of
Doctor of Philosophy

Seonyoung Yoo

07. 25. 2014
Approved by

_____

Advisor
Prof. Guntae Kim

A strategy for achieving high performance and durability of double perovskite cathode materials in solid oxide fuel cells

Seonyoung Yoo

This certifies that the dissertation of Seonyoung Yoo is approved.

07. 25. 2014

signature

_____

Advisor: Guntae Kim

signature

_____

Hyun-Kon Song

signature

_____

Soojin Park

signature

_____

Jinyoung Kim

signature

_____

Jong Shik Chung

Abstract

Solid oxide fuel cells (SOFCs) have been researched as new power generation devices on the basis of their high conversion efficiency, low emissions, and excellent fuel flexibility. The requirement for high operating temperature (800-1000 ^{o}C) of conventional SOFCs, however, leads to notable problems such as high costs and high rate of degradation due to the interactions between cell components during cell fabrication and/or operation. To overcome these problems, researchers have strived to lower the SOFC operating temperature toward an intermediate-temperature (IT) range (500-700 ^{o}C). One of the challenges for IT-SOFCs, however, is to develop cathode materials with sufficiently high electrocatalytic activity for oxygen reduction. Intensive research has thus been carried out to explore alternative cathode materials that achieve superior and stable electrochemical performance.

This dissertation focuses on the latter one with the aim to study a new cathode material for IT-SOFC applications. These materials thus can be presented as a promising IT-SOFC cathode material with remarkably stable performance and high power output.

I started with a brief overview of the critical issues relevant to overall solid oxide fuel cell in chapter 1 and then explained the experimental technique for electrochemical and thermodynamic properties in chapter 2. Finally, I introduced my research papers studying cathode for IT-SOFC as following,

1. Thermodynamic and electrical characteristics of $NdBaCo_2O_{5+\delta}$ at various oxidation and reduction states
2. Thermodynamic and Electrical Properties of Layered Perovskite $NdBaCo_{2-x}Fe_xO_{5+\delta}$ -YSZ (x = 0, 1) Composites for Intermediate Temperature SOFC Cathodes
3. Electrical Properties, Thermodynamic Behavior, and Defect Analysis of $La_{n+1}Ni_nO_{3n+1+\delta}$ Infiltrated into YSZ Scaffolds as Cathodes for Intermediate Temperature SOFCs
4. Comparative characterization of thermodynamic, electrical, and electrochemical properties of $Sm_{0.5}Sr_{0.5}Co_{1-x}Nb_xO_{3-\delta}$ (x = 0, 0.05, and 0.1) as cathode materials in intermediate temperature solid oxide fuel cells
5. Structural, electrical and electrochemical characteristics of $La_{0.1}Sr_{0.9}Co_{1-x}Nb_xO_{3-\delta}$ as a cathode material for intermediate temperature solid oxide fuel cells
6. Investigation of layered perovskite type $NdBa_{1-x}Sr_xCo_2O_{5+\delta}$ (x = 0, 0.25, 0.5, 0.75, and 1.0) cathodes for intermediate-temperature solid oxide fuel cells
7. A New Class of Double Perovskite Cathode for Low Temperature Solid Oxide Fuel Cells

Contents

List of figures

List of tables

Chapter 1. Introduction

1.1 Motivation Statements

Growing the clean alternative energy industry is key to enhancing the quality of life for individuals and societies.[1] Fossil fuels are not a renewable energy source however advanced and developing countries rely heavily on energy produced from these fuels. The ever-increasing demand and diminishing supply of fossil fuels will certainly cause problems for all countries in the future. In remote areas of developing countries, transmission and distribution of fossil fuel-generated energy can be difficult and expensive. Additionally, air pollution is an environmental problem which is caused by the use of fossil fuels, and results in the formation of NO_x and SO_x emissions.[2]

The critical technical barrier to the extensive application of various alternative energy technologies is the undesirable properties of the key materials. For example, alternative energy technologies such as solar, wind, nuclear, geothermal, hydroelectric, fuel cells, high-energy density batteries, and supercapacitors are being pursued intensively to address the impending energy problems and environmental concerns. Among them, fuel cells convert chemical energy directly into electrical energy continuously as long as the fuel and oxidant are supplied. The conventional power generators involving the conversion of fuel to heat, to mechanical energy, and then to electrical energy are limited by Carnot-cycle with a low efficiency of ~ 30 %. In contrast, fuel cells offer exceptionally high electrical efficiency (> 50 %) by eliminating the intermediate fuel to heat to mechanical energy conversion losses. Among all types of fuel cells, solid oxide fuel cells (SOFCs) offer great potential for the most efficient and cost-effective utilization of a wide multiplicity of fuel such as hydrocarbons, coal gas and gasified biomass.[3] To make SOFC technology affordable, however, the operating temperature must be reduced so that much less expensive materials can be used for other cell components and balance of plants.[4-13] The requirement for high operating temperature (800-1000 ^{o}C) of conventional SOFCs, however, leads to notable problems such as high costs and high rate of degradation due to the interactions between cell components during cell fabrication and/or operation. To overcome these problems, researchers have strived to lower the SOFC operating temperature toward an intermediate-temperature (IT) range (500-700 ^{o}C). One of the challenges for IT-SOFCs, however, is to develop cathode materials with sufficiently high electrocatalytic activity for oxygen reduction. Intensive research has thus been carried out to explore alternative cathode materials that achieve superior and stable electrochemical performance.[14-16]

1.2 Research Objectives

This manuscript concentrates on 1) advanced architectural designs of cathode for solid oxide fuel cells, impregnation, and 2) high-performance and durability with alternative cathode materials of solid oxide fuel cells, all to achieve the ultimate goal of dramatically increasing their power output.

1) To develop the new cathode materials for intermediate temperature solid oxide fuel cells (SOFCs)
2) To improve the electrochemical reaction site in cathode, try to use the electrode fabrication and modification by infiltration of active components into a porous scaffold
3) To overcome the weakness of simple perovskite in terms of structural stability and thermodynamic stability to alternate Co-rich materials
4) To compare the oxygen transport kinetics between simple and double perovskite oxide structure
5) To clarify the improved stability of cathode material by B site doping effect

1.3 General Introduction

1.3.1 The Basis of Fuel Cells

A fuel cell is an electrochemical device that provides efficient and clean power generation. Fuel cells will produce the mass product (electricity) as low as raw material (fuel) is supplied. While battery and fuel cell rely on electrochemistry to work, a fuel cells are not consumed when it produce electricity. This is the key difference between a fuel cell and battery. In fact fuel cells combine many of the advantages of both engines and batteries.

Since fuel cells produce electricity directly from chemical energy, they are often far more efficient than combustion engines. Fuel cells can be all solid state and mechanically ideal, meaning no moving parts. This yields the potential for highly efficient and long-lasting systems. A lack of moving parts also means that fuel cells are silent. Also, polluting products such as NO_x, SO_x, and particulate emissions are almost zero.

There are four types of fuel cells according to their electrolyte; they differ in operating temperature and power generation efficiency. While all fuel cell types are based upon the same underlying electrochemical principles, they all operate at different temperature regimens, in corporate different materials, and often differ in their fuel tolerance and performance properties.[17-19]

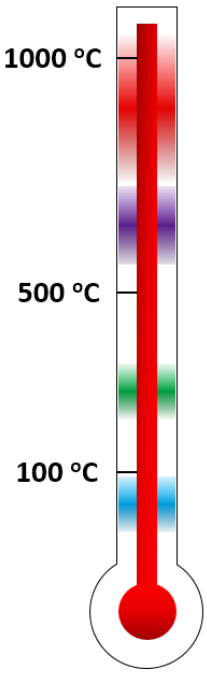

Operating temperature	Type of Fuel cell	Electrolyte	Power Generation Efficiency
700-1000 °C	Solid oxide type (SOFC)	Stabilized zirconia (Ceramic)	45-65 %
~650 °C	Molten carbonate type (MCFC)	Molten carbonate	45-50 %
~200 °C	Phosphoric-acid type (PAFC)	Phosphoric acid	35-42%
Room Temp. to 90 °C	Polymer electrolyte type (PEMFC)	Ion exchange membrane	35-40 %

Figure 1.1 Types of fuel cells

Solid oxide fuel cells (SOFCs) are appropriate for distributed on-site cogeneration of heat and power due to their unique operation and performance properties. The SOFC is an important enabling technology for future sustainable energy systems.

SOFCs basically consist of tree components of anode, electrolyte, and cathode. The fuel electrode must be able to suffer the highly reducing environment of the anode, while the air electrode must be able to endure the highly oxidizing environment of the cathode under a high operating temperature.[20-22]

1.3.2 Principles of SOFC operation

The schematic diagram in Figure 1.2 presents the basic operation of SOFC. SOFCs are the most efficient electrochemical devices yet invented for conversion of chemical fuels directly into electrical power. At the cathode, the oxygen reduction reaction (ORR) occurs by accepting electrons from the external circuit. The produced oxide ions (O^{2-}) pass through the ceramic electrolyte to the anode part and react with the protons produced by the oxidation of hydrogen or fuels to produce water and electrical energy. The hydrogen fuel oxidation reaction at the anode and the oxygen reduction reaction at the cathode occur at the three-phase boundary (TPB) site where the gas phase (hydrogen, air), electrode (electronic phase), electrolyte (ionic phase) are in contact as shown in Figure 1.3. Chemical energy is directly converted into electrical energy through this reaction. To enhance the active site, a porous electrode structure is employed while the dense electrolyte provides a physical barrier to prevent the direct mixing of fuel and air.

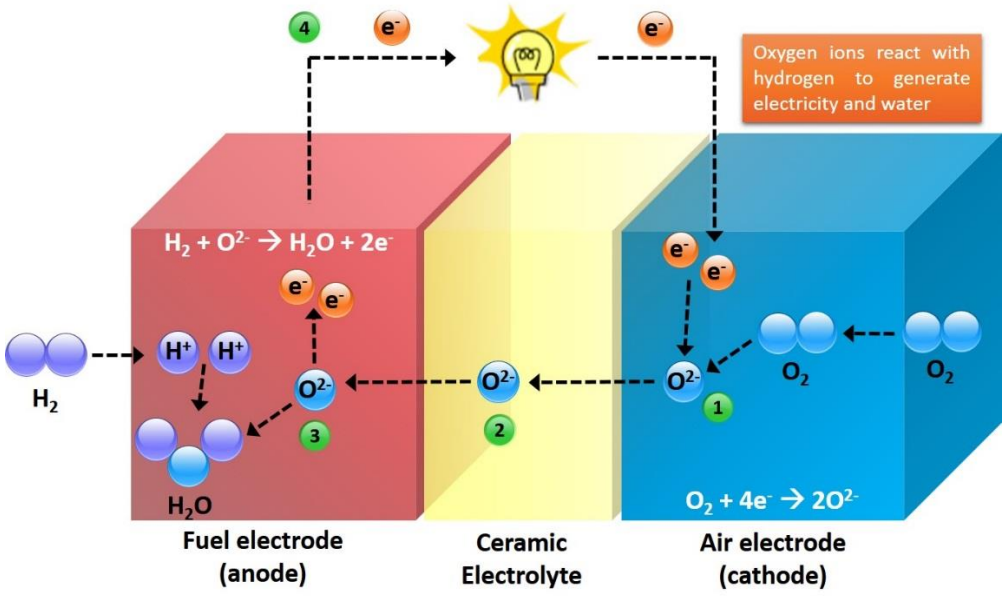

Figure 1.2 The schematic diagram of solid oxide fuel cell

The high operating temperatures (> 500 ºC) of SOFC, however, allow the use of inexpensive oxides or composites of metal oxides and cermet as catalysts instead of the expensive and scarcely available precious metal catalysts.[23] The requirement for high operating temperature (800-1000 ºC) of conventional SOFCs, however, leads to notable problems such as high costs and high rate of degradation due to the interactions between cell components during cell fabrication and/or operation. To overcome these problems, researchers have strived to lower the SOFC operating temperature toward an intermediate-temperature (IT) range (500-700 ºC). One of the challenges for IT-SOFCs, however, is to develop cathode materials with sufficiently high electrocatalytic activity for oxygen reduction. Intensive research has thus been carried out to explore alternative cathode materials that achieve superior and stable electrochemical performance.[13-15] Solution to improve the cell performance includes the use of alternative electrolyte and electrode materials. The overall cell reactions of fuel cells are given in equation as follow,

Anode reactions	$H_2 + O^{2-} \rightarrow H_2O + 2e^-$	(1.3.1)
Cathode reactions	$O2 + 4e^- \rightarrow 2O^{2-}$	(1.3.2)
Overall cell reactions	$H_2 + 1/2O_2 \rightarrow H_2O$	(1.3.3)

1.3.3 The Advantages and Challenges of SOFCs

SOFC employs ceramic and metal materials as electrodes and electrolyte and operate at high temperatures (> 500 ºC). The challenges for the SOFC society are to reduce cost and increase reliability. These challenges extend from the cell itself, to the stack interconnect and seals, to the balance of plant. The advantages and challenges of SOFC can be summarized as in Table 1.1.[12].

Table 1.1 The Advantages and Challenges of SOFCs

Advantages	Challenges
• Direct use of hydrocarbon fuels without requiring external fuel reforming • Use of less expensive catalyst as electrode • Higher energy conversion efficiency (> 60% for stand-alone, or over 80% while co-generating heat and power • Variety of applications ranging from small scale stationary power to hundreds of megawatts. • Elimination of corrosion problems encountered with liquid electrolytes • Reduction in CO2, NOx, and SOx emissions when hydrogen is used as a fuel	✓ Low oxide ion conductivity of yttria-stabilized zirconia electrolyte and slow oxygen reduction kinetics with the conventional cathode materials at intermediate operating temperatures (500 – 700 ºC) ✓ Chemical and mechanical durability problems of alternative electrolytes having higher oxide-ion conductivity at the intermediate temperatures ✓ Cycle operation and cold start cycles causing thermal stresses due to thermal expansion and contraction mismatches of the cell components ✓ Carbon cracking and poor tolerance to sulfur impurities with the conventional Ni-based anodes on using hydrocarbon fuels directly

1.4 Theoretical basics

1.4.1 Electrochemical Performance of SOFC

The performance of a fuel cell device can be summarized with a graph of its current-voltage characteristics. The current-voltage (*i*-V) curve, shows the voltage output of the fuel cell for a given current output.

An ideal fuel cell would supply any amount of current (as long as it is supplied with sufficient fuel), while maintaining a constant voltage determined by thermodynamics. However, the actual voltage output of a real fuel cell is less than the ideal thermodynamically predicted voltage. Furthermore, the more current that is drawn from a real fuel cell, the lower the voltage output of the cell, limiting the total power that can be delivered. The power (P) delivered by a fuel cell is given by the product of current and voltage:

$$P = i\,\mathrm{V} \tag{1.4.1}$$

A fuel cell power density curve, which gives the power density delivered by a fuel cell as a function of the current density, can be constructed from the information in a fuel cell *i*-V curve. The power density curve is produced by multiplying the voltage at each point on the *i*-V curve by the corresponding current density.[24]

The deviation of the practical cell voltage from the theoretical value is affected by several factors such as thickness of electrolyte, operating temperature, electrode/electrolyte materials, electrode morphology, and gas flow rate. The difference between the actual cell potential and theoretical potential is defined as polarization or over-potential (η).

$$\eta = E_{act} - E_{th} \tag{1.4.2}$$

A typical current-voltage (*i*-V) curve obtained in SOFC is indicated as shown in Fig. 1.3. The key factor to sign in this graph of cell voltage against current density are (1) the lower open circuit voltage compared to the theoretical value, (2) the fast initial drop in voltage, (3) the slow, linear voltage drop in the intermediate current region, and (4) the rapid voltage drop at higher current density. There are different kinds of polarization losses in fuel cell systems and are comprised of three contributions caused by the following factors.[25]

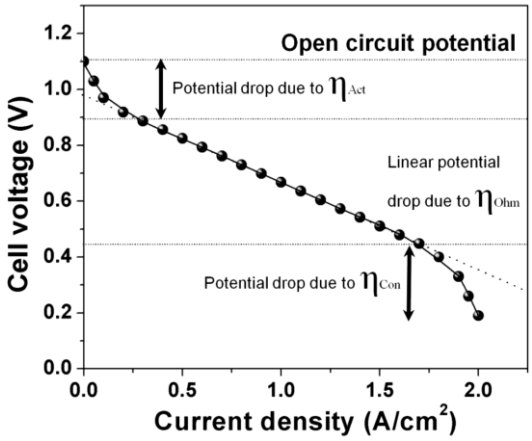

Figure 1.3 A typical current-voltage curve recorded in SOFC.[26]

- Kinetics of the electrochemical reaction (activation polarization, η_{Act})
- Internal electrical and ionic resistances (ohmic polarization, η_{ohm})
- Limitations in mass transport (concentration polarization, η_{con})

The activation polarization (η_{Act}) is basically related to the rate determining step, charge transfer or the surface exchange reactions in the electrode. For the electrode reaction to occur, the activation polarization can be understood as the overpotential consumed to provide the activation energy for the redox reactions in the electrode. The relationship between current density *i* and activation polarization η_{Act} can be expressed by the Butler-Volmer equation as[26]

$$i = i_0 \left[\exp\left(\frac{(1-\alpha)nF\eta_{Act}}{RT}\right) - \exp\left(\frac{-\alpha nF\eta_{Act}}{RT}\right)\right] \quad (1.4.3)$$

- i_0: the exchange current density
- α: the charge transfer coefficient
- η: the overpotential

When the irreversibility is small, Eqn. 1.4.3 can be written as the Tafel equation:

$$\eta_{Act} = a \pm b\log i \quad (1.4.4)$$

where *a* and *b* are constants and *b* is called the Tafel slope, indicating the catalytic activity; a smaller slope means better activity.

The ohmic polarization (η_{ohm}, known as *iR* drop) is related to the contact resistance between the cell components. It also includes ionic resistance in the electrolyte, electronic resistances in the electrodes, interfacial resistance between the electrodes and electrolyte, and wire resistance in the external circuit.

The concentration polarization (η_{con}) is from the change in concentration of the reactants at the surface of the electrodes as the fuel and oxidant are used. When the reactants cannot be provided fast enough to maintain the rate of the electrode reaction, exhaustion of reactants causes the concentration polarization. The concentration polarization (η_{con}) can be expressed as

$$\eta_{con} = \frac{RT}{nF}\ln\left(1 - \frac{i}{i_l}\right) \quad (1.4.5)$$

where i_l is the limiting current when the electrode reaction is completely governed by mass transfer.

The total polarization in the fuel cell system is the sum of three principal polarizations as[26,27]

$$\eta_{Total} = \eta_{Act} + \eta_{Ohm} + \eta_{Con} \quad (1.4.6)$$

1.4.2. The chemical thermodynamics of SOFCs

A SOFC is an electrochemical device which converts the Gibbs free enthalpy of the combustion reaction by a fuel and an oxidant gas directly into electricity. The first and the second law of thermodynamics allow the description of a reversible fuel cell, whereas in particular the second low governs the reversibility of the transport processes. The first law of the thermodynamics gives[28]

$$q + w = \Delta H \quad (1.4.7)$$

The molar reaction enthalpy ΔH of the oxidation consists of work and heat energy. The second law of thermodynamics applied on reversible processes yields

$$\oint \Delta S = 0 \rightarrow q = q_{rev} = T\,\Delta S \quad (1.4.8)$$

where the reversible heat exchange with the environment equalizes the generated reaction entropy, and we get

$$q_{rev} + w_{rev} = \Delta H \quad (1.4.9)$$

The reaction entropy is a result of the different opportunities of the species to save thermal energy between the absolute zero level of temperature and temperature level of the reactor.

Equations (1.4.7) and (1.4.8) give the molar reversible work, w_{rev}

$$w_{rev} = \Delta H - T\,\Delta S \tag{1.4.10}$$

Using the ambient temperature as a reference for the calculation of the Gibbs free enthalpy, ΔG, the reversible work of the reaction is equal to the Gibbs free enthalpy of the reaction

$$w_{rev} = \Delta G = \Delta H - T\,\Delta S \tag{1.4.11}$$

Based on the first and second laws of thermodynamics, the energy transfer from one form to another can be identified using thermodynamic potentials. From the first and the second laws of thermodynamics, an equation for internal energy (U) that is based on the variation of two independent variables of entropy *S* and volume *V* is derived where *p* is the pressure and *T* is temperature:[29]

$$dU = T\,dS - p\,dV \tag{1.4.12}$$

Note that $T\,dS$ represents the reversible heat transfer and $p\,dV$ is the mechanical work. The following equations show how the dependent variables (T and p) are related to variations in the independent variables (*S* and *V*):

$$\left(\frac{dU}{dS}\right)_v = T \tag{1.4.13}$$

$$\left(\frac{dU}{dS}\right)_s = -p \tag{1.4.14}$$

A conversion of U using a Legendre transform begins with defining the new thermodynamic potential $G\,(T, p)$ as follows:

$$G = U - \left(\frac{dU}{dS}\right)_v S - \left(\frac{dU}{dS}\right)_s V \tag{1.4.15}$$

From (1.4.13) and (1.4.14), we obtain

$$G = U - TS + pV \tag{1.4.16}$$

The variation of G results in

$$dG = dU - TdS - SdT + pdV + Vdp \tag{1.4.11}$$

Since $dU = T\,dS - p\,dV$,

$$dG = -SdT + Vdp \tag{1.4.12}$$

Analogously to eqn (1.3.9), the new thermodynamic potential H can be defined as

$$H = U - \left(\frac{dU}{dS}\right)_v \tag{1.4.13}$$

From (1.4.8), we obtain

$$H = U + pV \tag{1.4.14}$$

where H stands for enthalpy. Through differentiation, it is revealed that H is a function of S and p:

$$dH = dU + pdV + Vdp \tag{1.4.15}$$

$$dH = TdS + Vdp \tag{1.4.16}$$

Considering the overall reaction of SOFCs,

$$\mathrm{O_2} + \frac{1}{2}\mathrm{O_2} \rightarrow \mathrm{H_2O}$$

the difference in Gibbs free energy of formation of ΔG during the reaction can be given as

$$\Delta G = \Delta G_{\mathrm{H_2O}} - \Delta G_{\mathrm{H_2}} - \tfrac{1}{2}\Delta G_{\mathrm{O_2}} \tag{1.4.17}$$

If all the Gibbs free energy is consumed to electrical work, then

$$\Delta G = -nFE \tag{1.4.18}$$

where n and F represent number of electrons involved in the chemical reaction and the Faraday constant, respectively.

If the reactant and products are all in their standard conditions, the reversible standard potential E^0 of the electrochemical reaction is defined as[25]

$$E^0 = -\frac{\Delta G^0}{nF} \tag{1.4.19}$$

Here, the Gibbs free energy is dependent on the temperature by the relation

$$\Delta G = \Delta H - T\,\Delta S \tag{1.4.20}$$

Substitution of the standard condition values (T = 273.15 K, p = 1 atm) into (1.4.19) gives the standard electrode potential E^0

$$E^0 = (237900\ J\ mol^{-1})/(2 * 96485\ C\ mol^{-1}) = 1.23\ \text{V}$$

Beyond the standard condition, the theoretical reversible potential E_{th} can be derived by the Nernst equation as

$$E_{th} = E^0 - \left(\frac{RT}{2F}\right) \ln\left(\frac{p_{H_2O}}{p_{H_2} p_{O_2}^{\frac{1}{2}}}\right) \quad (1.4.21)$$

where R is the gas constant, T is the absolute temperature, p is the partial pressure of each gas.

1.4.3 Oxygen Reduction Reaction Mechanism in SOFC cathode

For understanding of ORR at a cathode, it should be known that ORR occurs only at electrochemical reaction site, typically called three phase boundary (TPB) where gas, the ionic conductor, and the electronic conductor are in contact. A schematic diagram of a TPB is shown in Fig. 1.4. The TPB concept is limited, because the oxygen reduction reaction also involves chemical adsorption, surface transport, and interfacial kinetics. The electrochemical reduction of the oxygen molecule as seen in (1.4.5.1) occurs in a series of elementary electrochemical process, which contain adsorption, dissociation, surface diffusion, and charge transfer, resulting in the production of oxygen ions.[30]

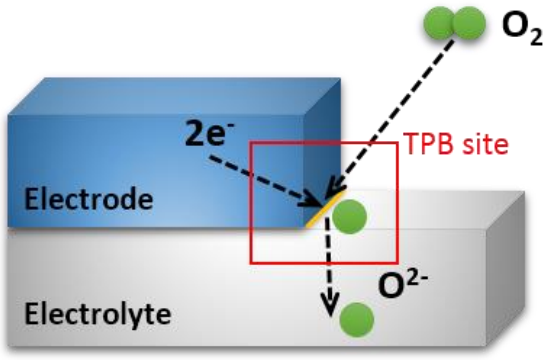

Figure 1.4 The schematic diagram showing three-phase boundary (TPB)

$$O_{2,gas} + 2V_O^{\bullet\bullet} + 4e' \rightarrow 2O_O^x \qquad (1.4.5.1)$$

where, in Kroger-Vink notation, $V_O^{\bullet\bullet}$ is a vacant oxygen site, and O_O^x is an oxygen ion on a regular oxygen site in the ionic conducting electrolyte lattice. As derived by (1.4.5.1), the ORR process requires the presence of oxygen and electrons as well as the possibility for generated oxide ions to be transported away from the reaction site into the bulk of the electrolyte. When the electrode material and the electrolyte material possess only electronic and ionic conductivity, respectively.

The cathode material should have a high electronic conductivity, a high catalytic activity for the ORR, chemical and structural stability at high temperatures and in oxidizing atmosphere, and compatibility with the other cell components.

A continuum model of the mechanism of the ORR at a porous mixed conducting cathode was introduced by Adler *et al*.[32] This ALS model provide a mechanism in which the oxygen molecule (gas phase) is reduced chemically at the gas/mixed conductor interface and is transported through the mixed conductor by solid state diffusion. The chemical exchange of oxygen at the gas/mixed conductor interface was considered as a non-charge transfer process. Adler presented the summary of oxygen reduction mechanisms on SOFC cathodes as following.

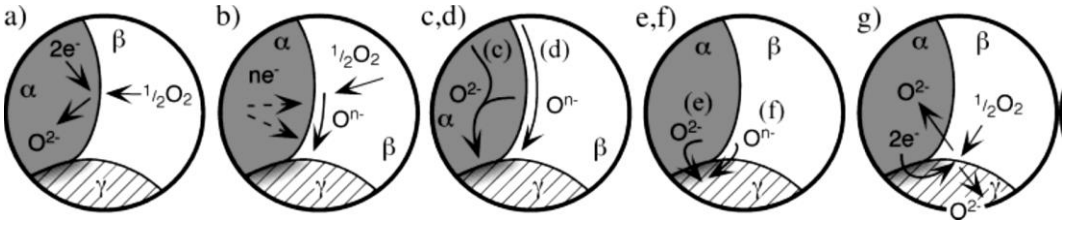

Figure 1.5 Some mechanisms thought to govern oxygen reduction in SOFC cathodes. Phases α, β, and γ refer to the electronic phase, gas phase, and ionic phase, respectively: (a) Incorporation of oxygen into the bulk of the electronic phase (if mixed conducting); (b) adsorption and/or partial reduction of oxygen on the surface of the electronic phase; (c) bulk or (d) surface transport of O^{2-} or O^{n-}, respectively, to the α/γ interface, (e) Electrochemical charge transfer of O^{2-} or (f) combinations of Onand e^-, respectively, across the α/γ interface, and (g) rates of one or more of these mechanisms wherein the electrolyte itself is active for generation and transport of electro-active oxygen species.[32]

1.4.4 Mass and Charge transport in mixed conducting oxides

We may first consider uncharged particles within an ionic solid. These particles are in equilibrium if their chemical potential, μ , is spatially constant, *i. e.*

$$\nabla \mu = 0 \tag{1.4.4.1}$$

The same condition applies for charged species in the absence of an electric field. The chemical potential is defined as the partial derivative of the Gibbs energy, G ($T,p,n_1,n_2,...$), with respect to the mole number, n_i, of particles of type *i*:

$$\mu_i = \left(\frac{\partial G}{\partial n_i} \right)_{p,T,n_{j \neq i}} \tag{1.4.4.2}$$

An alternative expression for the chemical potential is

$$\mu_i = \mu_i^0 + RT \ln a_i \tag{1.4.4.3}$$

The constant μ_i^0 is the standard chemical potential of particles *i* within the specific matrix, *R*, the gas constant and *T* the absolute temperature. The activity, a_i, can be replaced by the concentration, c_i, in cases where the distribution of the particles *i* is purely statistical (no interactions), which is normally fulfilled in "dilute" situations (*i.e.* low concentrations). A more general treatment considering also charged particles in non-zero electric fields allows the introduction of the electrochemical potential, $\tilde{\mu}$, defined as

$$\tilde{\mu} = \mu + ze\varphi \tag{1.4.4.4}$$

φ is the electrical potential, *z* the charge number of the respective particle, and *e* the elementary charge. Then, the more general condition for spatial equilibrium reads

$$\nabla \tilde{\mu} = 0 \tag{1.4.4.5}$$

If the gradient of the electrochemical potential is unequal to zero, a net particle flux, *J*, is expected, which - for not too high gradients - is given by

$$J_i = -\frac{\sigma_i}{z_i^2 e^2} \tilde{\nabla} \tilde{\mu}_i \tag{1.4.4.6}$$

Here σ denotes the electrical conductivity. Eq.1.4.6 is the fundamental transport equation which can be derived within the framework of linear irreversible thermodynamics[32,33]. It is very general with respect to the nature of the "particle" *i* (charged or neutral, electronic or ionic, particle or defect) and the driving force (chemical or electric). Well-known special cases of Eq.1.4.6 are Ohm´s law (for $\nabla \mu = 0$) and Fick´s law of diffusion (for $\nabla \varphi = 0$ and $a_i = c_i$). These relationships have a wide validity range, showing that the linear approximation is often a good description for transport phenomena in ionic solids. The electrical conductivity, σ_i, is proportional to the concentration, c_i, and the mobility, u_i, of particles *i*:

$$\sigma_i = |z_i| e u_i c_i \qquad (1.4.4.7)$$

When transport processes in solid compounds are considered, one particular type of particle is frequently much more mobile than the other(s). In such cases the partial lattice of the virtually immobile type of particle is chosen as the reference system.[33] For a mixed conducting material, the total conductivity, σ_{tot}, can be written as the sum over the partial conductivities of all electronic (electron) and ionic (ion) defects, provided that the charge carriers are transported independently of each other. In most cases, this is a good approximation.

$$\sigma_{tot} = \sigma_{electron} + \sigma_{ion} = \sum_i |z_{i,electron}| e u_{i,electron} c_{i,electron} + \sum_j |z_{j,ion}| e u_{j,ion} c_{j,ion} \quad (1.4.29)$$

A general way to obtain materials with high ionic conductivity is to increase their effective charge carrier concentration by aliovalent doping. ZrO_2 may be considered as an example, the material on which the phenomenon of ionic conduction in solids was discovered by Nernst in 1899[34] and theoretically explained by Wagner, C. in 1943[35]: If ZrO_2 is doped with metal oxides such as CaO, Y_2O_3 or Sc_2O_3, the di- or trivalent metal cations replace tetravalent zirconium ions in the ZrO_2 crystal lattice. For charge compensation, vacancies in the oxygen sublattice (and also, to a minor degree, electronic defects) are generated. Since typical dopant concentrations in solid state ionics are of the order of 10 %, a large number of oxygen vacancies is introduced into ZrO_2 by this procedure. The result is a material with a high ionic conductivity at elevated temperatures (*e.g.* 2.5×10^{-2} S cm^{-1} for 9 mol% Y_2O_3-ZrO_2 at 750℃[36]). The movement of ionic defects is a thermally activated hopping process. Empirically, a relationship

$$\sigma(T) \sim \exp\left(\frac{E_A}{kT}\right) \qquad (1.4.4.8)$$

is often found, with a typical activation energy of ~ 0.8 *eV* at higher temperatures. Besides temperature-dependent defect concentrations, the activation of the hopping process is the main reason for the strong temperature dependence of the ionic conductivity in many ceramic materials.

1.4.5 Perovskite type oxide as cathode material

The relevant characteristics of perovskite type oxides as SOFC cathodes, such as a simple and a double peroskite oxide, having general chemical formula of ABO_3 and $AA'B_2O_5$, respectively, will be introduced.

1.4.5.1 Simple perovskite oxides

The simple perovskite oxides, particularly mixed ionic and electronic conductors (MIECs) containing Mn, Fe, Co, and/or Ni with the capability to conduct oxygen ions and electrons simultaneously are strong candidates as IT-SOFC cathodes.[37-40] Among the various MIEC oxides, cobalt containing perovskite oxides such as $(La,Sr)CoO_3$ and $(Ba,Sr)CoO_3$ have attracted strong interest due to their high electrocatalytic activity for the oxygen reduction reaction.[41-43] The high catalytic activity of LSC can be explained by its high ionic conductivity with lower overpotential and high oxygen vacancy concentration, which facilitates rapid migration of oxygen species through the bulk as well as the surface of the electrode material. In addition, recent reports investigating Co-based perovskites, such as $Sm_{0.5}Sr_{0.5}CoO_{3-\delta}$ (SSC), have also garnered notable attention[44].

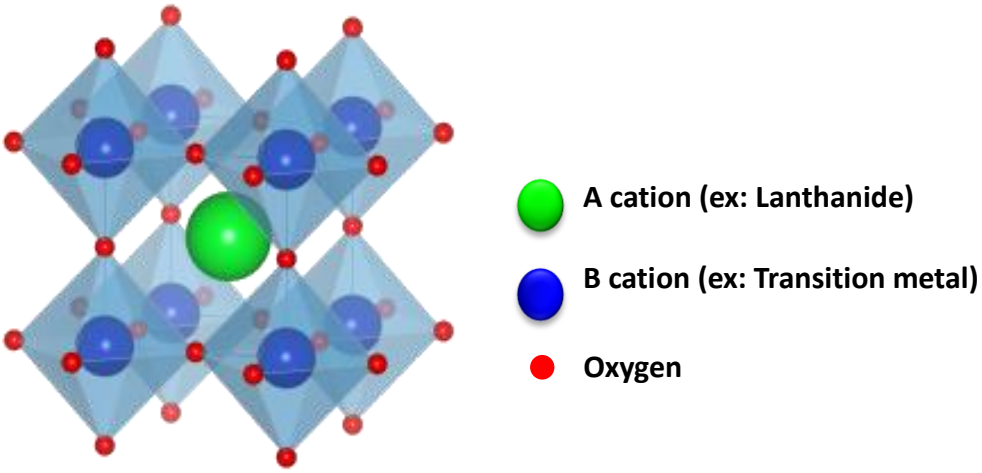

Figure 1.6 Crystal structure of a simple perovskite oxides

Due to their flexibility in terms of doping, perovskites with the general formula $ABO_{3-\delta}$, in which A and B are cations with a total charge of +6, are the most widely used SOFC cathode materials. The perovskite structure, in which A is the larger cation with 12-fold oxygen coordination and B is the smaller cation with 6-fold oxygen coordination, can be tailored by partial or total substitution of one or both cations, varying the materials

properties (in terms of electronic and ionic conductivity, TEC, and catalytic activity) to fulfill the stringent requirements for SOFC cathodes. The A site is usually occupied by a mixture of rare earth metals (typically La) and alkaline earth metals (such as Sr, Ca, and Ba), whereas the B site is occupied by one or several mixed-valence transition metal ions (such as Mn, Co, Fe, and Ni); the mixed valence provides the catalytic activity for the ORR[6→45]. Substitution of the A and/or B sites by aliovalent A' and/or B' cations (*e.g.*, partial substitution of La^{3+} with Sr^{2+}) can result in two different compensation mechanisms to maintain charge neutrality or in a combination of both mechanisms[88→46]. If the ionic compensation mechanism takes place, oxygen vacancies are created, which results in a variation in the ionic conductivity, which produce via the vacancy migration mechanism for perovskites. In contrast, if the electronic compensation mechanism occur, the Bn^{+} cations are oxidized/reduced, which directly affects the electronic properties of the material. The temperature and oxygen partial pressure (pO_2) also directly influence the oxidation state and oxygen vacancy concentration of the $ABO_{3-\delta}$ perovskites. Generally, as the temperature increases and pO_2 decreases, oxygen vacancies are formed (and δ increases), and the lower-oxidation states are favored.

Table 1.2 The most relevant materials properties for the main state-of-are SOFC cathodes

Family	Composition	TEC (K^{-1})	σ (S cm^{-1})	D^* (cm^2 s^{-1})	k^* (cm s^{-1})	References
			500-750 °C	600 °C	600 °C	
Perovskites	$La_{0.8}Sr_{0.2}MnO_{3-\delta}$	12.0×10^{-6}	120–130	5.2×10^{-18}[(a)]	1.5×10^{-11}[(a)]	47-49
	$La_{0.5}Sr_{0.5}CoO_{3-\delta}$	21.3×10^{-6}	1,300–1,800	2.6×10^{-9}	1.3×10^{-6}	49-51
	$La_{0.6}Sr_{0.4}Co_{0.2}Fe_{0.8}O_{3-\delta}$	15.3×10^{-6}	300–330	1.7×10^{-10}	1.1×10^{-7}	52,53
	$Ba_{0.5}Sr_{0.5}Co_{0.8}Fe_{0.2}O_{3-\delta}$	24×10^{-6}	30–35	3.3×10^{-7}	1.4×10^{-5}	54-56
Double Perovskites	$GdBaCo_2O_{5+\delta}$	16.4×10^{-6}	550–925	7.0×10^{-10}	3.1×10^{-7}	57,58
	$PrBaCo_2O_{5+\delta}$	24.6×10^{-6}	400–700	6.4×10^{-9}	2.8×10^{-7}	59-61
RP K_2NiF_4 Type	$Pr_2NiO_{4+\delta}$	13.6×10^{-6}	100–120	2.5×10^{-8}	5.1×10^{-7}	62
	$La_2NiO_{4+\delta}$	13.0×10^{-6}	55–65	8.7×10^{-9}	1.7×10^{-8}	62,63

(a) For $La_{0.8}Sr_{0.2}MnO_{3-\delta}$, D^* and k^* were extrapolated from high-temperature values.

Despite being the most attractive cathode materials for the intermediate-temperature range [64], LSCF-based cathodes severe efficiency degradation over time, typically at a rate of 0.05% per hour[65]. Among the proposed possible degradation mechanisms common to most of the studied MIEC perovskites are interaction between LSCF (LSC and BSCF) and

YSZ [66-69], Cr poisoning[70,71], sulfur poisoning, coarsening of the cathode microstructure, loss of conductivity, formation of an insulating silicate layer in humid atmosphere[72,73], and Sr surface segregation. The enrichment of Sr at the cathode surface may deactivate sites for ORR and hence increase cathode resistance[65]. Sr surface segregation occurs in many Sr-doping, state-of-the-art perovskite materials (*e.g.*, LSM, LSC, and LSCF), for which the Sr concentration increase and Sr surface segregation have been correlated with a surface activity decrease[72,74] and with the volatilization of Sr species[75].

1.4.5.2 Ruddlesden-Popper oxides

Layered A_2BO_4 oxides with a K_2NiF_4-type structure, known as the $n = 1$ Ruddlesden-Popper (RP) phase (the general formula for RP phases is $A_{n+1}B_nO_{3n+1}$), are among the most widely investigated alternatives to perovskites. Depending on A- and B-site doping, pO_2, and temperature, the oxygen content of these phases can be either hyper- or hypostoichiometric ($A_2BO_{4\pm\delta}$) and therefore results in the presence of oxygen interstitials or vacancies as point defect vehicles for oxygen diffusion. The great advantage of the structure, formed by perovskite ABO_3 and rock-salt AO layers alternated along the c-axis, is its ability to accommodate hyperstoichiometric oxygen in interstitial sites (in the rock-salt layers), providing ionic conductivity without the need for A-site aliovalent substitution. Alkaline earth–free (Sr- and Ba-free) materials can be advantageous for long-term stability, as avoiding a mixed A-site occupation may help decrease cation segregation and may largely reduce Cr and S poisoning ($SrCrO_4$ or $SrSO_4$ precipitates may block the active surface)[72].

Many theoretical and experimental studies have been devoted to the understanding of the oxygen migration pathways and to the measurement of the diffusion coefficients of these RP phases. A high anisotropy (of a factor of ~100) between the ab plane and c-axis oxygen diffusion was first measured for both hype rand hypostoichiometric cuprates ($La_2CuO_{4+\delta}$ and $La_{1.85}Sr_{0.15}CuO_{4-\delta}$)[76]; hyperstoichiometric compounds ($\delta > 0$) are of most interest for cathode applications due to their high oxygen diffusion coefficient. Recent MD simulations predicted highly anisotropic oxygen diffusion to occur via an interstitialcy mechanism for $La_2NiO_{4+\delta}$, $Pr_2NiO_{4+\delta}$, and $La_2CoO_{4+\delta}$ materials[77]; almost all the migration was predicted to take place along the *ab* plane. Despite a certain scatter in the theoretical and experimental E_a values, a very high anisotropy (of approximately three orders of magnitude) was very recently measured for $Pr_2NiO_{4+\delta}$, and $Nd_2NiO_{4+\delta}$, single crystals. Together, these research groups are attempting to replicate these measurements, as the reported c-axis diffusivity may have been overestimated due to experimental limitations. In

addition, an anisotropy in the surface exchange of between one and two orders in magnitude was also reported for all these RP compounds, as the ab-plane surface exchange coefficient is always the fastest one. Although a few studies have focused on the MIEC properties of the cobaltite (Ln_2CoO_4) and cuprate (Ln_2CuO_4) compositions, by far the most widely studied RP compounds for cathode applications are the $Ln_2NiO_{4+\delta}$ nickelates, with Ln = La, Nd, or Pr. In addition to the high diffusivity of the oxygen interstitial ions and good electrocatalytic properties, these compounds also possess a relatively low TEC that results in a good match with the common electrolyte materials (see Table 1.2). In this case, the property limiting the electrochemical performance of these RP phases seems to be their moderately low electronic conductivity. As for the case of the perovskite materials, a few recent studies have been devoted to the microstructural optimization of nickelate cathodes, resulting in low ASR values for (a) $La_2NiO_{4+\delta}$ (~1.2 Ωcm^2 at 600◦C) by using symmetrical cells of 3% yttria-doped zirconia together with yttria-doped CeO_2 (YDC) barrier layers[78] and (b) for $Nd_2NiO_{4+\delta}$ (~2 Ωcm^2 at 600◦C) by using YSZ together with a YDC barrier layer. However, after microstructure optimization, the best-performing nickelates are expected to be Pr-based nickelates and composites, as $Pr_2NiO_{4+\delta}$ presents the lowest polarization resistance[79], which is related to its superior electrochemical properties. For this composition, the best cell performance (400 $mWcm^{-2}$ at 600◦C) was obtained for an anode supported cell by using a Co-doped CGO layer between the cathode and a zirconia electrolyte However, for these RP phases, a careful selection of the electrolyte material and of the fabrication/operation temperature is required. For example, $La_2NiO_{4+\delta}$ reacts with YSZ and CGO at temperatures starting from 900◦C[80,81] but is stable with the LSGM electrolyte for up to 72 h at 1,000◦C. A CeO_2-based interface layer between the YSZ electrolyte and the cathode is also beneficial when $Pr_2NiO_{4+\delta}$ and$Nd_2NiO_{4+\delta}$ are used, as it helps to improve cell performance and to avoid degradation with time due to delamination problems[79].

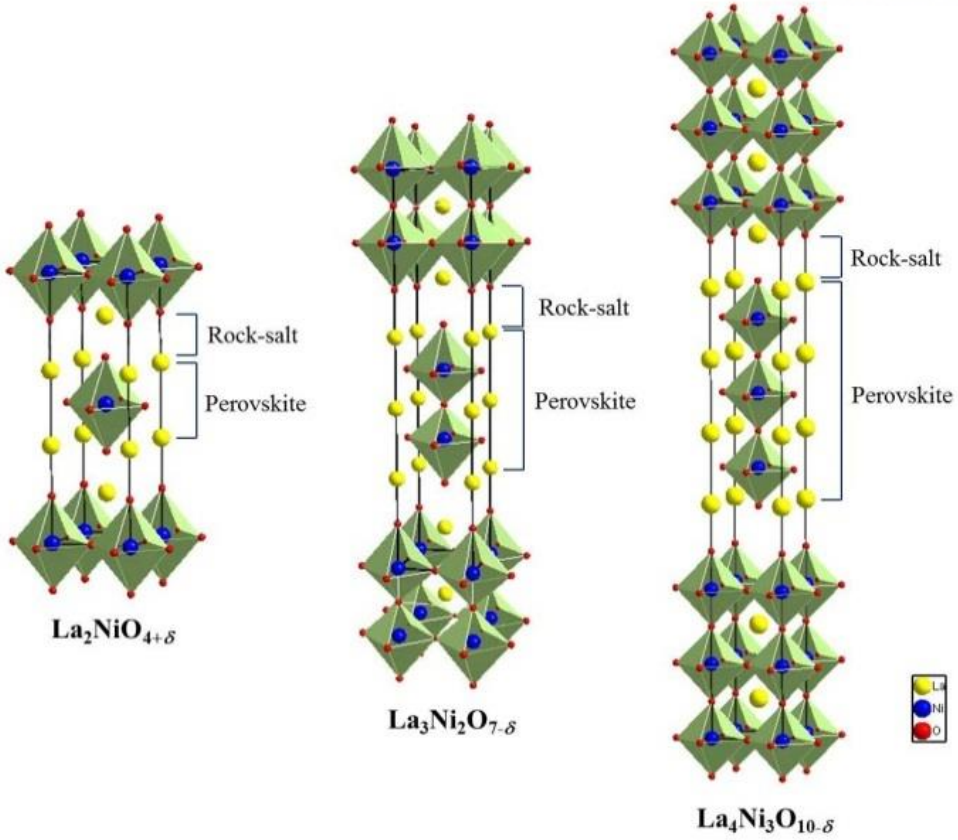

Figure 1.8 Crystal structure of Ruddlesden-Popper series; $La_{n+1}Ni_nO3_{n+1}$

1.4.5.3 Double perovskite oxide: A-site-ordered double perovskites

In recent times, a noble perovskite-related oxides, namely double perovskites with the general formula $AA'B_2O_{5+\delta}$ (with A = rare earth, A' = alkaline earth, and B = Co or Mn), has been proposed as next-generation intermediate-temperature cathodes. Starting from a normal perovskite structure, by 50% substitution of the A sites by lower-valence A' cations, one can obtain an ordered structure with the A and A' cations alternated along the c-direction. This A-site ordering is induced by the large size difference between the two aliovalent cations and results in enhanced oxygen diffusivity, as first demonstrated by Taskin *et al.* for $GdBaMn_2O_{5+\delta}$. The anisotropic oxygen transport in these compounds—whereby the oxygen ions move easily between the LnO and CoO_2 layers, but not in the BaO layers and then experimentally proven by isotopic exchange experiments for $PrBaCo_2O_{5+\delta}$(PBCO) polycrystalline samples and $GdBaCo_2O_{5+\delta}$ (GBCO). In addition, a combined theoretical and experimental work recently showed that the oxygen diffusion mechanism in $NdBaCo_2O_{5+\delta}$ is also anisotropic and occurs along a complex trajectory between the NdO and CoO_2 planes,

whereas the Ba-containing planes act as an oxygen diffusion barrier[82].

Recently, several groups have reported a class of layered perovskite oxides, based on their much higher chemical diffusion and surface exchange coefficients relative to those of ABO_3-type perovskite oxides[83-85]. The layered perovskite oxides can be described with the general formula $AA'B_2O_{5+\delta}$, with the A-site being a rare earth element, the A′ site an alkaline earth element, and the B-site a transition element. These oxides consist of sequential layers $[BO_2]$-[AO]-$[BO_2]$-[A′O] stacked along the *c*-axis.[86] This layered structure reduces the oxygen bonding strength in the [AO] layer and provides a disorder-free channel for ion motion, which enhances oxygen ion diffusivity.[87]

Based on these properties, layered perovskites such as $LnBaCo_2O_{5+\delta}$ (Ln = Pr, Nd, Sm, and Gd) perovskites have been studied for their capability for application as IT-SOFC cathode materials. Kim *et al*.[61] reported that $PrBaCo_2O_{5+\delta}$ (PBCO) offers rapid oxygen ion diffusivity and a surface exchange coefficient at the IT range. These characteristics have strong potential to improve the conductivity and catalytic activity for the ORR of layered perovskite oxides. In addition, several groups have reported that the substitution of Sr for Ba in $LnBaCo_2O_{5+\delta}$ can improve the conductivity and the catalytic activity for the ORR of layered perovskite oxides.[88,89] Kim *et al*.[83] demonstrated that Sr-doped layered perovskite materials are promising cathode materials for use in IT-SOFC applications. Our group has extensively studied a class of double perovskite oxides, $LnBaCo_2O_{5+\delta}$(Ln = Pr, Nd, Sm)[85-90], with the aim of exploiting their high electrical conductivity and high catalytic activity for the ORR. We have found that Sr doping into the Ba site enhanced the electrical conductivity and the ORR, improving the electrochemical cell performance dramatically.

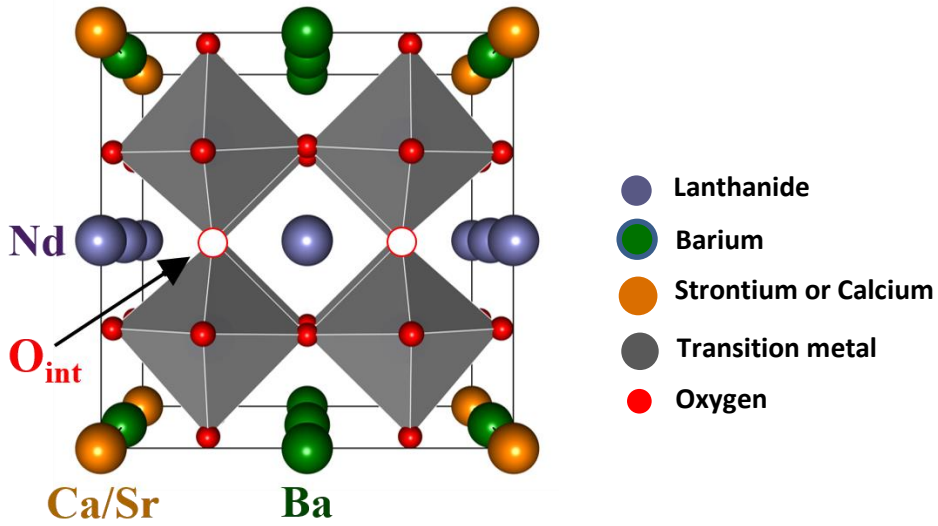

Figure 1.7 Crystal structure of a double perovskite oxides

Chapter 2. Experimental Techniques

2.1 Citric precursor synthesis and sample preparation

The various cathode materials presented in this dissertation were synthesized by citric precursor method. The conditions and procedures employed varied depending on the material system. While the general procedures are given in this Chapter, more details of the synthesis will be given in the relevant Chapters. Metal nitrate were used as the cationic sources, and citric acid and ethylene clygol as the monomers for formic the polymetric matrix. Metal nitrate of the appropriate composition ratio were dissolved in a mixture of citric acid and ethylene glycol (1:4 molar ratio). Stoichiometric amounts of metal nitrates were added into a beaker containing a suitable amount of concentrated nitric acid solution under continuous heating and stirring. An adequate amount of ethylene glycol was added into the beaker after the mixture was dissolved. After a viscous resin was formed, the mixture was heated around 300 ^{o}C. The resultant products were pre-calcined at 600 ^{o}C for 4 hours, ball-milled in acetone for 24 hours.[86]

The black powder were pressed in 18 mm diameter circular die at 200 bar, annealed at 1473 K for 12 hours, and then cooled down in air. The density of the sintered pellet was 90-95 % of theoretical density measured by the Archimedes method.

2.2 Cell fabrication

Symmetrical cells with a configuration of electrode | GDC | electrode were used for impedance spectroscopy. GDC powder was pressed into pellets of ~1 mm thick and sintered at 1350 ^{o}C for 4 hours in air to obtain a dense electrolyte membrane. Cathode slurries were then painted onto both surfaces of dense GDC electrolyte and fired at 1000 ^{o}C for 4 hours.

Ni-GDC anode-supported cells with a configuration of Ni-GDC | GDC | cathode were fabricated by a drop-coating method. NiO powder, GDC powder, and starch (weight ratio of 6:4:1.5) were mixed by ball milling in ethanol for 24 hours. After drying, the NiO-GDC mixture was pressed into a pellet (~0.6 mm thick and 15 mm diameter). Thin GDC electrolyte membranes were prepared by a refined particle suspension coating technique. A GDC suspension was prepared by dispersing GDC powders (Aldrich) in ethanol with a small amount of binder (polyvinyl Butyral, B-98) and dispersant (Triethanolamine, Alfa Aesar) at a ratio of 1:10. The GDC suspension was applied to a NiO-GDC anode support by drop-coating, followed by drying in air and subsequent co-sintering at 1400 ^{o}C for 5 hours.

2.3 Structure analysis

The materials synthesized were characterized by variety of techniques. A more general description of the techniques is provided in this chapter, and any specific information will be presented in the respective chapters.

X-ray powder diffraction (XRD) (Rigaku diffractometer, Cu Ka radiation) analysis was used to confirm the crystalline structures of samples. In situ XRD was also obtained from room to operating temperature (Bruker, D8 Advance). The microstructures and morphologies of LnBSCF cathode samples were observed using a field emission scanning electron microscope (SEM) (Nova SEM). The TEM images were acquired with JEOL JEM 2100F with a probe forming (STEM) Cs corrector at 200 kV. A thermogravimetric analysis (TGA) was carried out using a SDT-Q600 (TA instrument, USA). TGA experiments were performed from 100 ^{o}C to 900 ^{o}C with a heating/cooling rate of 2 ^{o}C min^{-1} in air. The room-temperature oxygen content values were determined by iodometric titration.

2.4 Electrical and electrochemical testing

Electrical conductivities of cathode materials were determined in air using a four-electrode measurement. All four electrodes were made of Ag wire and Ag paste. The current and voltage were controlled/measured using a potentiostat (BioLogic) in the temperature range of 100 to 750 ^{o}C with an interval of 50^{o}C.

For symmetrical cells, two Ag wires were attached to each of the two electrodes using Ag paste. Each cell was mounted on an alumina tube using a ceramic adhesive (Aremco, Ceramabond 552). Impedance spectra were recorded under OCV in a frequency range of 1 mHz to 500 kHz with ac perturbation of 14 mV in the temperature range of 500-650^{o}C.

For the single cell tests, each cell was mounted on an alumina tube using a ceramic adhesive. Humidified (with 3 vol% H_2O) H_2 was used as the fuel at a flow rate of 100 mL min^{-1} (passing through a water bubbler at 25^{o}C), whereas ambient air was supplied to cathode as the oxidant. Impedance spectra and *I-V* polarization curves were obtained with a BioLogic Potentiostat. The *I-V* polarization curves were recorded between 500 ^{o}C and 650 ^{o}C.

2.5 Redox property and oxygen nonstoichiometric property

The redox property and oxygen nonstoichiometry of cathodes were measured using coulometric titration (CT) as a function of the oxygen partial pressure, $p(O_2)$. Coulometric titration was used to

accurately quantify the oxidation/reduction state of a composite as a function of $p(O_2)$. It involves placing the oxide sample in a sealed container, separated from atmosphere by an O^{2-}-conducting membrane like yttria-stablized zirconia (YSZ). Electrodes on either side of the membrane are used to measure the potential across the membrane, and the potential can be related to the $p(O_2)$ through the Nernst Equation.

Current is applied to the isolated YSZ tube to pump oxygen out of the tube and wait until the samples in the tube to reach equilibrium. The magnitude of the current in amperes and the duration of the current in seconds can be used to determine the moles of the species removed from the system, O_2 in this case. The key component of our experimental setup in Fig. 2.1 is the yttria-stabilized zirconia (YSZ) tube (McDanel Advanced Ceramic Technologies, Z15410630) which was used both to electrochemically pump oxygen out of the system and to sense the equilibrium $p(O_2)$ inside the tube. Silver paste (SPI supplies, 05063-AB) was painted onto both sides of the YSZ tube to form the inside and outside electrodes. Pt wire was used as a lead wire to make electrical connections to the instruments. Half of the YSZ tube could be inserted into the furnace since the both ends of the tube were attached to a stainless-steel fitting with a Viton O-ring.[19]

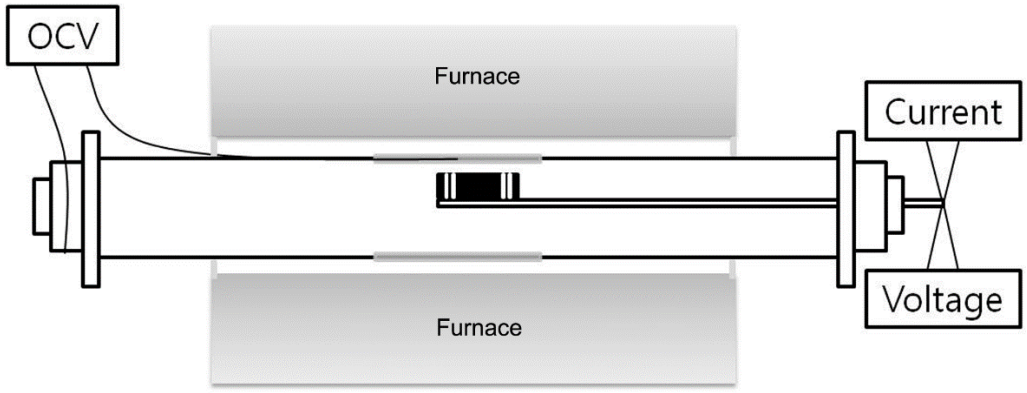

Figure 2.1 Schematic diagram of coulometric titration instrument.

Reference

1. Lewis, N.S.; Nocera, D.G.; *Proceedings of the National Academy of Sciences of the United States of America*, **2006**, *103*, 15729.
2. Dignon, J.; *Atmospheric Enviornment* **1992**, *26A*, 1157.
3. Zhan, Z. L.; Barnett, S. A.; An Octane-fueled solid oxide fuel cell. *Science*, **2005**, *308*, 844-847.
4. Liu, M.; Rational SOFC material design: new advances and tools. *Mater. Today* **2011**, *14*, 534-546.
5. Park, S. D.; Vohs, J. M.; Gorte, R. J.; Direct oxidation of hydrocarbones in a solid-oxide fuel cell. *Nature* **2000**, *404*, 265-267.
6. Wachsman, E. D.; Lee, K. T.; Lowering the temperature of solid oxide fuel cells. *Science* **2011**, *334*, 935-939.
7. Xia, C.; Liu. M.; Novel Cathodes for Low-Temperature Solid Oxide Fuel Cells. *Adv. Mater*. **2002**, *14*, 521-523.
8. Yang, L.; Choi, Y.M.; Qin, W.; Chen, H.; Blinn, K.; Liu, M.; Liu. P.; Bai, J.; Tyson, T. A.; Liu, M.; Promotion of water-mediated carbon removal by nanostructured barium oxide/nickel interfaces in solid oxide fuel cells. *Nat. Commun.* **2011**, *2*, 357-365.
9. Yang, L.; Wang, S.; Blinn, K.; Liu, M.; Liu, Z.; Cheng, Z.; Liu, M.; Enhanced Sulfur and Coking Tolerance of a Mixed Ion Conductor for SOFCs: $BaZr_{0.1}Ce_{0.7}Y_{0.2-x}Yb_xO_{3-\delta}$. *Science* **2009**, *326*, 126-129.
10. Singhal, S. C.; Advances in solid oxide fuel cell technology. *Soild State Ionics* **2000**, *135*, 305-313.
11. Huang, Y. H.; Dass, R. I.; Xing, Z. L; Goodenough, J. B.; Double perovskites as anode materials for solid-oxide fuel cells. *Science* **2006**, *312*, 254-257.
12. Mogensen, M.; Jensen, K. V.; Jorgensen, M. J.; Primdahl,S.; Progress in understanding SOFC electrodes. *Solid State Ionics* **2002**, *150*, 123-129
13. Steele, B. C. H.; Material science and engineering: The enabling technology for the commercialisation of fuel cell systems. *J. Mater. Sci.* **2001**, *36*, 1053-1068.
14. Horita, T.; Katsuhiko, Y.; Natsuko, S.; Harumi, Y.; André, W.; Ellen, I.-T.; Oxygen reduction mechamism at porous $La_{1-x}Sr_xCoO_{3-\delta}$ cathodes/$La_{0.8}Sr_{0.2}Ga_{0.8}Mg_{0.2}O_{2.8}$ electrolyte interface for solid oxide fuel cells. *Electrochim. Acta* **2001**, *46*, 1837-1845.
15. Adler, S. B.; Factors Governing Oxygen Reduction in Solid Oxide Fuel Cell Cathodes. *Chem. Rev*. **2004**, *104*, 4791-4843.
16. Señarís-Rodríguez, M. A.; Goodenough, J. B.; Magnetic Transport Properties of the System

La_{1-x} $Sr_xCoO_{3-\delta}$ ($0 < x \leq 0.50$). *J. Solid State Chem*. **1995**, *118*, 434-446.

17. Shao, Z. P; Haile, S. M.; A high-performance cathode for the next generation of solid-oxide fuel cells. *Nature* **2004**, *431*, 170-173.
18. Vohs, J.; Gorte, R.J.; High-Performance SOFC Cathodes Prepared by Infiltration, *Adv. Mater*. **2009**, *21*, 943-956.
19. Yoo, S.; Shin, J.; Kim, G.; Thermodynamic and electrical characteristics of $NdBaCo_2O_{5+\delta}$ at varous oxidation and reduction states, *J. Mater. Chem*. **2011**, *21*, 439-443.
20. Badwal, S.P.S.; Stability of solid oxide fuel cell components, Solid State Ionics **2001**, *143*, 39-46.
21. Fergus, J.W.; Hui, R.; Li, X.; Wilkinson, D.P.; Zhang, J.; Solid oxide fuel cells – Materials Properties and Performance: Taylor & Francis Group, CRC Press **2009**, pp 1-8.
22. Minh, N. Q.; Takahshi, T.; *Science and Technology of Ceramic Fuel Cells*, Elsevier Science B. V., Amsterdam, Netherlands **1995**, pp 4-8.
23. Singhal, S.C.; Advances in solid oxide fuel cell technology, Solid State Ionics 135 (2000) 305-313.
24. O'Hayre, R.; Cha, S.-W.; Colella, W.; Prinz, F.B.; Fuel Cell Fundamentals, 2nd Edition, John Wiley & Sons, INC. **2009**, pp 25-66.
25. Bard, A. J.; Faulkner, L.R.; Electrochemical Methods: Fundamentals and Applications, John Wiley & Sons, New York, **2000**.
26. Kim, Y.N.; *Doctoral thesis*, University of Texas at Austin, **2011**.
27. Yamamoto, O.; Takeda, Y.; Kanno, R.; Noda, N.; Perovskite-type oxides as oxygen electrodes for high temperature oxide fuel cells, *Solid State Ionics* **1987**, *22*, 241-246.
28. Bove, R.; Ubertini, S.; *Modeling Solid State Fuel Cells: Chapter 2. Thermodynamics of Fuel Cells; Springer* **2008**; pp 15-24.
29. Brett, C.M.A.; Brett, A.M.O.; *Electrochemistry: Principles, Methods, and Applications, Oxford University Press Inc.; New York; USA* **1993**; pp 14.
30. Dyer, C. K.; Moseley, P. T.; Ogumi, Z.; Rand, D.A.J.; Scrosati, B.; *Newnes, Encyclopedia of Electrochemical Power Sources* **2013**.
31. Schmalzried, H.; *Chemical Kinetics of Solids, Heinheim; Germany, VCH, Verlagsgesellschaft*, **1995**.
32. Rickert, H.; *Electrochemistry of Solids; Berlin; Germay; Springer-Verlag*.
33. Nernst, W.; *'Über die elektrolytische leitung faster Körper bei sehr hohen Temperaturen' Zeitschrift fur Elektrochemie*, 6, pp 41-43.
34. Wagner, C.; *'Über die Mechanismus der elektrischen Stromleitung im Nernststift' Die*

Naturwissenschaften, 31, pp 265-268.

35. Singhal, S.C.; Kendall, K.; *High temperature solid oxide fuel cells: fundamentals, design, and applications.* Oxford: Elsevier Science Ltd. **2003**.
36. Acuña, L.M.; Peña-Martínez, J.; Marrero-López, D.; Fuentes, R.O.; Nuñez, P.; Lamas, D.G.; *J. Power Sources* **2011**, *196*, 9276.
37. Choi, S.; Shin, J.; Kim, G.; The electrochemical and thermodynamic characterization of $PrBaCo_{2-x}Fe_xO_{5+\delta}$ (x = 0, 0.5, 1) infiltrated into yttria-stabilized zircornia scaffold as cathodes for solid oxide fuel cells, *J. Power Sources*, **2012**, *201*, 10-17.
38. Petrov, A.N.; Kononchuk, O. F.; Andreev, A. V.; k Cherepanov, V.A.; Kofstad, P.; Self-compensation characteristics of Eu ions in $BaTiO_3$, *Soid State Ionics*, **1995**, *80*, 189.
39. Kawada, T.; Suzuki, J.; Sase, M.; Kaimai, A.; Yashiro, K.; Nigara, Y.; Determination of Oxygen Vacancy Concentration in a Thin Film of $La_{0.6}Sr_{0.4}CoO_{3-\delta}$ by an Electrochemical Method, *J. Electrochem. Soc.*, **2002**, *149*, E252-E259.
40. Jacobson, A.J.; Materials for solid oxide fuel cells, *Chem. Mater*., **2010**, *22*, 660-674.
41. Kilner, J.A.; Burriel, M.; Materials for Intermediate-Temperature Solid-Oxide Fuel Cells, *Annu. Rev. Mater. Res*. **2014**, 44, 365-393.
42. Liu, B.; Chen, X.; Dong, Y.; Mao, S.S.; Cheng, M.; A High-Performance, Nanostructured $Ba_{0.5}Sr_{0.5}Co_{0.8}Fe_{0.2}O_{3-\delta}$ Cathode for Solid-Oxide Fuel Cells, *Adv. Energy. Mater*., **2011**, *1*, 343-346.
43. Xia, C.; Rauch, W.; Chen, F.; Liu, M.; $Sm_{0.5}Sr_{0.5}CoO_3$ cathodes for low-temperature SOFCs, *Solid State Ionics* **2002**, *149*, 11-19.
44. Kim, J.-H.; Manthiram, A.; $LnBaCo_2O_{5+\delta}$ Oxides as Cathodes for Intermediate-Temperature Solid Oxide Fuel Cells, *J. Electrochem. Soc*., **2008**, *155*, *4*, B385-B390.
45. Taskin, A.A.; Lavrov, A.N.; Ando, Y.; Achieving fast oxygen diffusion in perovskites by cation ordering, *Appl. Phys. Lett*., **2005**, 86, 090910-090913.
46. Zhao, L.; Shen, J.; He, B.; Chen, F.; Xia, C.; Synthesis, characterization and evaluation of $PrBaCo_{2-x}Fe_xO_{5+\delta}$ as cathodes for intermediate-temperature solid oxide fuel cells, *Int. Hydrogen Energy*, **2011**, 36, 3658-3655.
47. Berenov, A.; Wood, H.; Atkinson, A.; Evaluation of $La_{0.8}Sr_{0.2}Cu_{1-x}Mn_xO_y$ double perovskite for use in SOFCs. *J. Electrochem. Soc*., **2007**, 154, B1362–1367
48. Ahlgren, EO.; Poulsen, F.W; Thermoelectric power and electrical conductivity of strontium-doped lanthanum manganite. *Solid State Ionics* **1996**, 86–88, 1173–1178.
49. De, Souza, R.A.;, Kilner, J.A.; Oxygen transport in $La_{1-x}Sr_xMn_{1-y}Co_yO_{3+/-\delta}$ perovskites. Part I. Oxygen tracer diffusion. *Solid State Ionics*, **1998**, 106:175–87.

50. Lee, K.T.; Manthiram, A.; Comparison of $Ln_{0.6}Sr_{0.4}CoO_{3-\delta}$ (Ln = La, Pr, Nd, Sm, and Gd) as cathode materials for intermediate temperature solid oxide fuel cells. *J. Electrochem. Soc*. **2006**, 153, A794–798.
51. Petrov, A.N.; Kononchuk, O.F.; Andreev, A.V.; Cherepanov, V.A.; Kofstad, P.; Crystal structure, electrical and magnetic properties of $La_{1-x}Sr_xCoO_{3-y}$. Solid State Ionics, 1995, 80:189–99.
52. Tai L.W.; Nasrallah, M.M. Anderson, H.U.; Sparlin, D.M.; Sehlin, S.R.; Structure and electrical properties of $La_{1-x}Sr_xCo_{1-y}Fe_yO_3$. Part 2. The system $La_{1-x}Sr_xCo_{0.2}Fe_{0.8}O_3$. *Solid State Ionics*, **1995**, 76, 273–283.
53. Esquirol, A.; Kilner, J.A.; Brandon, N.; Oxygen transport in $La_{0.6}Sr_{0.4}Co_{0.2}Fe_{0.8}O_{3-\delta}$ /$Ce_{0.8}Ge_{0.2}O_{2-x}$ composite cathode for IT-SOFCs. *Solid State Ionics* 2004, 175, 63–67.
54. Vente, J.F.; McIntosh, S.; Haije, W.G.; Bouwmeester, H.J.M.; Properties and performance of $Ba_xSr_{1-x}Co_{0.8}Fe_{0.2}O_{3-\delta}$ materials for oxygen transportmembranes. *J. Solid State Electrochem.* **2006**, 10, 581–588.
55. Wei, B.; Lü, Z.; Huang, X.; Miao, J.; Sha, X.; et al. Crystal structure, thermal expansion and electrical conductivity of perovskite oxides $Ba_xSr_{1-x}Co_{0.8}Fe_{0.2}O_{3-\delta}$ ($0.3 \le x \le 0.7$). *J. Eur. Ceram. Soc*. **2006**, 26, 2827–2832.
56. Wang, L.; Merkle, R.; Maier, J.; Acartürk, T.; Starke, U.; Oxygen tracer diffusion in dense $Ba_{0.5}Sr_{0.5}Co_{0.8}Fe_{0.2}O_{3-\delta}$ films. *Appl. Phys. Lett*. **2009**, 94, 071908.
57. Tarancón, A.; Skinner, S.J.; Chater, R.J.; Hernández-Ramírez, F.; Kilner, J.A.; Layered perovskites as promising cathodes for intermediate temperature solid oxide fuel cells. *J. Mater. Chem*. **2007**, 17, 3175–3181.
58. Tarancón, A.; Marrero-López, D.; Peña-Martínez, J.; Ruiz-Morales, J.; Nùñez, P.; Effect of phase transition on high-temperature electrical properties of $GdBaCo_2O_{5+x}$ layered perovskite. *Solid State Ionics*, **2008**, 179, 611–618.
59. Burriel, M.; Peña-Martínez, J.; Chater, R.J.; Fearn, S.; Berenov, A.V.; et al.; Anisotropic oxygen ion diffusion in layered $PrBaCo_2O_{5+\delta}$. *Chem. Mater*. **2012**, 24, 613–621.
60. Zhao, L.; Shen, J.; He, B.; Chen, F.; Xia, C.; Synthesis, characterization and evaluation of $PrBaCo_{2-x}Fe_xO_{5+\delta}$ as cathodes for intermediate-temperature solid oxide fuel cells. *Int. J. Hydrogen Energy*, **2011**, 36, 3658–3665.
61. Kim, G.; Wang, S.; Jacobson, A.J.; Reimus, L.; Brodersen, P.; Mims, C.A.; Rapid oxygen ion diffusion and surface exchange kinetics in $PrBaCo_2O_{5+x}$ with a perovskite related structure and ordered A cations. *J. Mater. Chem*. **2007**, 17, 2500–2505.
62. Boehm, E.; Bassat, J.; Dordor, P.; Mauvy, F.; Grenier, J.; Stevens, P.; Oxygen diffusion and

transport properties in non-stoichiometric LnNiO oxides. *Solid State Ionics*, **2005**, 176, 2717–2725.

63. Sayers, R.; De Souza, R.A.; Kilner, J.A.; Skinner SJ. 2010.Lowtemperature diffusion and oxygen stoichiometry in lanthanum nickelate. *Solid State Ionics*, **2010**, 181, 386–391.
64. Kuklja, M.M.; Kotomin, E.A.; Merkle, R.; Mastrikov, Y.A.; Maier, J.; Combined theoretical and experimental analysis of processes determining cathode performance in solid oxide fuel cells. *Phys. Chem. Chem. Phys*. **2013**, 15, 5443–5471.
65. Ding, H.; Virkar, A.V.; Liu, M.; Liu, F.; 2013. Suppression of Sr surface segregation in $La_{1-x}Sr_xCo_{1-y}Fe_yO_{3-\delta}$: a first principles study. *Phys. Chem. Chem. Phys*. **2013**, 15, 489–496.
66. Parfitt, D.; Chroneos, A.; Tarancón, A.; Kilner, J.A.; Oxygen ion diffusion in cation ordered/disordered $GdBaCo_2O_{5+\delta}$, *J. Mater. Chem*. **2011**, *21*, 2183-2186.
67. Hjalmarsson, P.; Søgaard, M.; Mogensen, M.; Electrochemical performance and degradation of $(La_{0.6}Sr_{0.4})_{0.99}CoO_{3-\delta}$ as porous SOFC-cathode. *Solid State Ionics*, **2008**, 179, 1422–1426.
68. Yamamoto, O.; Takeda, Y.; Kanno, R.; Noda, M.; Perovskite-type oxides as oxygen electrodes for high temperature oxide fuel cells. *Solid State Ionics*, **1987**, 22, 241–246.
69. Simner, S.P.; Anderson, M.D.; Engelhard, M.H.; Stevenson, J.W.; Degradation mechanisms of La–Sr–Co–Fe–O_3 SOFC cathodes. *Electrochem. Solid State Lett*. **2006**, 9, A478–481.
70. Taniguchi, S.; Kadowaki, M.; Kawamura, H.; Yasuo, T.; Akiyama, Y.; et al.; Degradation phenomena in the cathode of a solid oxide fuel cell with an alloy separator. *J. Power Sources*, **1995**, 55, 73–79.
71. Yokokawa, H.; Horita, T.; Sakai, N.; Yamaji, K.; Brito, M.E.; et al.; Thermodynamic considerations on Cr poisoning in SOFC cathodes. *Solid State Ionics*, **2006**, 177, 3193–3198.
72. Bucher, E.; Sitte, W.; Long-term stability of the oxygen exchange properties of $(La,Sr)_{1-z}(Co,Fe)O_{3-\delta}$ in dry and wet atmospheres. *Solid State Ionics*, **2011**, 192, 480–482.
73. Bucher, E.; Sitte, W.; Klauser, F.; Bertel, E.; Oxygen exchange kinetics of $La_{0.58}Sr_{0.4}Co_{0.2}Fe_{0.8}O_3$ at 600◦C in dry and humid atmospheres. *Solid State Ionics*, **2011**, 191, 61–67.
74. Yan, L.; Salvador, P.A.; Substrate and thickness effects on the oxygen surface exchange of $La_{0.7}Sr_{0.3}MnO_3$ thin films. *ACS Appl. Mater. Interfaces*, **2012**, 4, 2541–2550.
75. Chroneos, A.; Yildiz, B.; Tarancón, A.; Parfitt, D.; Kilner, J.A.; Oxygen diffusion in solid oxide fuel cell cathode and electrolyte materials: mechanistic insights from atomistic simulations, *Energy & Environ. Sci*., **2011**, *4*, 2774-2789.
76. Claus, J.; Borchardt, G.; Weber, S.; Hiver, J.M.; Scherrer, S.; Combination of EBSP measurements and SIMS to study crystallographic orientation dependence of diffusivities in a

polycrystalline material: oxygen tracer diffusion in $La_{2-x}Sr_xCuO_{4+/-\delta}$. *Mater. Sci. Eng. B*, **1996**, 38, 251–257.

77. Jiang, L.; Wei, T.; Zeng, R.; Zhang, W-X.; Huang, Y-H.; Thermal and electrochemical properties of $PrBa_{0.5}Sr_{0.5}Co_{2-x}Fe_xO_{5+\delta}$ (x = 0.5, 1.0, 1.5) cathode materials for solid-oxide fuel cells. *J. Power Sources* **2013**, 232, 279–285.
78. Mesguich, D.; Bassat, J.M.; Aymonier, C.; Brüll, A.; Dessemond, L.; Djurado, E.; Influence of crystallinity and particle size on the electrochemical properties of spray pyrolyzed $Nd_2NiO_{4+\delta}$ powders. *Electrochim. Acta*, **2013**, 87, 330–335.
79. Ferchaud, C.; Grenier, J-C.; Zhang-Steenwinkel, Y.; van, Tuel, M.M.A.; van, Berkel, F.P.F.; Bassat, J-M.; High performance praseodymium nickelate oxide cathode for low temperature solid oxide fuel cell. *J. Power Sources*, **2011**, 196, 1872–1879.
80. Hernández, A.M.; Mogni, L.; Caneiro, A.; $La_2NiO_{4+\delta}$ as cathode for SOFC: reactivity study with YSZ and CGO electrolytes. *Int. J. Hydrogen Energy*, **2010**, 35, 6031–6036.
81. Sayers, R.; Liu, J.; Rustumji, B.; Skinner, S.J.; Novel K_2NiF_4-type materials for solid oxide fuel cells: compatibility with electrolytes in the intermediate temperature range. *Fuel Cells* **2008**, 8, 338–343.
82. Lalanne, C.; Prosperi, G.; Bassat, J.; Mauvy, F.; Fourcade, S. et al.; Neodymium-deficient nickelate oxide $Nd_{1.95}NiO_{4+\delta}$ as cathode material for anode-supported intermediate temperature solid oxide fuel cells. *J. Power Sources* **2008**, 185, 1218–1224.
83. Kim. J.H.; Cassidy, M.; Irvine, J.T.S.; Bae, J.; Electrochemical Investigation of Composite Cathodes with $SmBa_{0.5}Sr_{0.5}Co_2O_{5+\delta}$ Cathodes for Intermediate Temperature-Opertating Solid Oxide Fuel Cell, *Chem. Mater*., **2010**, *22*, 883-892.
84. Kim, J.-H.; Proda, F.; Manthiram, A.; Characterization of $GdBa_{1-x}Sr_xCo_2O_{5+\delta}$ ($0 \leq x \leq 1.0$) Double Perovskites as Cathodes for Solid Oxide Fuel Cells, *J. Electrochem. Soc.* **2008**, *155*, B1023-B1028.
85. Jun, A.; Kim, J.; Shin, J.; Kim, G.; Optimization of Sr content in layered $SmBa_{1-x}Sr_xCo_2O_{5+\delta}$ perovskite cathodes for intermediate-temperature solid oxide fuel cells, *Int. Hydrogen Energy*, **2012**, *37*, 18381-18388.
86. Park, S.; Choi, S.; Kim, J.; Shin, J.; Kim, G.; Strontium Doping Effect on High-Performance $PrBa_{1-x}Sr_xCo_2O_{5+\delta}$ as a Cathode Material for IT-SOFCs, *ECS Electrochem. Lett*., **2012**, *1*, F29-F32.
87. Yoo, S.; Choi, S.; Kim, J.; Shin, J.; Kim, G.; Investigation of layered perovskite type $NdBa_{1-x}Sr_xCo_2O_{5+\delta}$($x$ = 0, 0.25, 0.5, 0.75, and 1.0) cathodes for intermediate-temperature solid oxide fuel cells, *Electrochimica Acta*, **2013**, *100*, 44-50.

88. Kim, J.; Jun, A.; Shin, J.; Kim, G.; Effect of Fe Doping on Layered $GdBa_{1-x}Sr_xCo_2O_{5+\delta}$ Perovskite Cathodes for Intermediate Temperature Solid Oxide Fuel Cells, *J. Am. Ceram. Soc*., **2014**, *97*, 651-656.
89. Choi, S.; Park, S.; Kim, J.; Lim, T.-H.; Shin, J.; Kim, G.; Electrochemical properties of an ordered perovskite $LaBaCo_2O_{5+\delta}$-$Ce_{0.9}Gd_{0.1}O_{2-\delta}$ composite cathode with strontium doping for intermediate-temperature solid oxide fuel cells, *Electrochem. Comm*., **2013**, *34*, 5-8.
90. Choi, S.; Yoo, S.; Kim, J.; Park, S.; Jun, A.; Sengodan, S.; Kim, J.; Shin, J.; Jeong, H.Y.; Choi, Y.M.; Kim, G.; Liu, M.; Highly efficient and robust cathode materials for low-temperature solid oxide fuel cells: $PrBa_{0.5}Sr_{0.5}Co_{2-x}Fe_xO_{5+\delta}$, *Sci. Rep*. **2013**, *3*, 2426-2431.

Chapter 3. Thermodynamic and electrical characteristics of $NdBaCo_2O_{5+\delta}$ at various oxidation and reduction states

3.1 Introduction

Solid oxide fuel cell (SOFC) is a device that converts the chemical energy in a fuel to electrical energy directly with high efficiency and low emission. This high efficiency comes from its high operating temperatures (1073 to 1273 K), which lower electrode overpotential and resistance of solid electrolytes compared to other types of fuel cells. High operating temperatures, however, cause some drawbacks such as high costs and high rate of formation of electrical and chemical insulating phases due to the solid state reaction between the SOFC components during the cell fabrication and operation. Therefore, significant efforts have been reported on lowering operating temperature to 873 to 1073 K.[1,2] But, it is essential to develop the high electrochemical activity on the cathode because the polarization loss of the cathode is a limiting factor on total cell performance as the operating temperature decreases.

Recently, cation ordered perovskite-related oxides, $LnBaCo_2O_{5+\delta}$ (Ln = Pr, Nd, Sm, Gd and Y), are known as one of the best cathode materials for intermediate-temperature solid oxide fuel cells (IT-SOFCs) because of their rapid oxygen diffusion and surface exchange kinetics and high electrical conductivities.[3,4] The $LnBaCo_2O_{5+\delta}$ structure consists of the repeating stacking sequence ...$BaO/CoO_2/LnO_x/CoO_2$… to form structures closely related to the cuprate superconductors. The excess oxygen atoms, which are mobile, locate in the interstitial sites between the LnO layers and may show highly anisotropic oxygen diffusion between perovskite and fluorite structure.[5] Kim *et al*.[6] reported that $PrBaCo_2O_{5+\delta}$ (PBCO) is a promising material for IT-SOFC cathodes which showed unusual fast oxygen kinetics at lower temperature (773 to 973K), resulting in low cathodic polarization loss. Independent works of Ding *et al*.[7] and Kim *et al*.[8] examined $LnBa_{0.5}Sr_{0.5}Co_2O_{5+\delta}$ (Ln = Pr, Sm) which substituted some Ba into Sr to improve the conductivity of layered perovskite oxides. Both demonstrated excellent electrochemical performance with ceria based electrolyte and stability of single cell.

Through the comprehensive survey on cation ordered perovskite-related oxides, $NdBaCo_2O_{5+\delta}$ is chosen as a base material of this research because better fuel cell performance can be expected due to the lower cathode resistance, which can be conjectured from the fact that the electrical conductivity of Nd is known to be higher than that of Pr of PBCO.

Recent studies of $LnBaCo_2O_{5+\delta}$ have focused on its structure, oxygen kinetics and electrochemical properties or the fuel cell performance itself without considering the basic oxygen thermodynamic behavior. Moreover, the characteristics of $LnBaCo_2O_{5+\delta}$–YSZ composites, which are

actual configuration of the porous electrodes, have been completely unknown even though its redox properties of the oxide-YSZ composites could be different completely from those of the pure oxide.[9] Its redox properties regarding oxygen thermodynamics such as oxidation enthalpies and entropies of NBCO and/or NBCO-YSZ composites have never been reported, with which the development of the new electrodes can be expedited if the oxygen thermodynamics of the material can be identified prior to the fuel cell test. For example, if a new electrode material possesses poor redox properties or can be decomposed at the fuel cell operating temperature and $p(O_2)$ (atm) range, it cannot be used as an electrode.

The impregnation method for electrode fabrication has been known to be very flexible, allowing the synthesis of anode and cathode composites with a wide range of compositions. In addition to avoiding solid-state reactions, composites formed by impregnation have the additional advantage of forming a non-random structure, having a thermal expansion match close to that of the YSZ backbone, leading to good conductivity at relatively low metal loadings, and allowing much greater flexibility in preparing electrodes with more complex microstructure.[10]

In this work, we prepared the NBCO-YSZ composites by impregnation and characterize the composite as a promising candidate for a cathode of IT-SOFC. Coulometric titration and 4-probe conductivity method are used to measure the thermodynamic and electrical properties simultaneously at various conditions. Different redox properties and electrical conductivities are evaluated to check the possibility used as a cathode material.

3.2 Experimental

$NdBaCo_2O_{5+\delta}$ (NBCO)-YSZ composites were prepared by the impregnation of NBCO into porous YSZ (Tosoh corp. TZ-8Y). The porous YSZ was prepared by mixing YSZ powder, dispersant (Duramax3005, Rohm & Haas), binder (HA-12 and B-1000, Rohm & Haas), and pore former (Graphite, Alfa Aeser, 325 mesh). This solution was sintered at 1773K for 4 hours and dried afterwards to make YSZ with 65% porosity. Stoichiometric amounts of $Nd(NO_3)_3 \cdot 6H_2O$ (Aldrich, 99.9%, metal basis), $Ba(NO_3)_2$ (Aldrich, 99+%), $Co(NO_3)_2 \cdot 6H_2O$ (Aldrich, 98+%) were dissolved in distilled water, which were infiltrated into porous YSZ up to higher than 35wt% loading. The composite was calcined in air at 723 and 1023K.

The composites were characterized by X-ray diffraction (XRD), scanning electron microscopy (SEM). X-Ray powder diffraction measurements (Rigaku diffactormeter, Cu Ka radiation) was performed to confirm the structure with a scan rate of 0.5^o min^{-1} and the range $20^o < 2\theta < 60^o$.

Coulometric titration was used to accurately quantify the oxidation/reduction state of a composite as a function of $p(O_2)$.[11,12] It involves placing the oxide sample in a sealed container, separated from atmosphere by an O^{2-}-conducting membrane like yttria-stablized zirconia (YSZ).

Electrodes on either side of the membrane are used to measure the potential across the membrane, and the potential can be related to the $p(O_2)$ through the Nernst Equation.

Current is applied to the isolated YSZ tube to pump oxygen out of the tube and wait until the samples in the tube to reach equilibrium. The magnitude of the current in amperes and the duration of the current in seconds can be used to determine the moles of the species removed from the system, O_2 in this case.

The key component of our experimental setup is the yttria-stabilized zirconia (YSZ) tube (McDanel Advanced Ceramic Technologies, Z15410630) which was used both to electrochemically pump oxygen out of the system and to sense the equilibrium $p(O_2)$ inside the tube. Silver paste (SPI supplies, 05063-AB) was painted onto both sides of the YSZ tube to form the inside and outside electrodes. Pt wire was used as a lead wire to make electrical connections to the instruments. Half of the YSZ tube could be inserted into the furnace since the both ends of the tube were attached to a stainless-steel fitting with a Viton O-ring.

The electrical conductivity of composite slabs that were 1.6mm x 4.5mm x 9.6mm in size was measured with a four-probe configuration with a BioLogic Potentiostat.

Samples for thermodynamics and conductivity measurements were held up near the center of the tube. 5% O_2 in Ar flows into the tube for a long time so that the samples could be equilibrated in this atmosphere sufficiently at the start of the experiment. The criterion of thermodynamic equilibrium of oxygen concentration is within 1 mV per hour.

3.3 Results

The XRD patterns of 43 wt% NBCO-YSZ composite calcined at 1023 K for 4 h in air are shown in Fig. 3.1. The XRD patterns demonstrate that the NBCO and YSZ are present as separate phases indicating no second phases between NBCO and YSZ at 973 K. SEM images of composites formed after calcination at 1123 K are shown in Fig. 3.2. The pictures show YSZ pores roughly 5 μm in diameter, coated with NBCO nano-scale particles. The NBCO is distinguished from the YSZ by the differences in the texture of the phases. The connections of coated NBCO for electron transport are very good, and the pore size in the NBCO matrix for the supply of oxygen molecule is wide enough, expecting higher electrochemical performance. A comparison of the micrographs obtained after calcination at 1123 K and 1273 K indicate that the NBCO nano-scale particles at the higher calcination temperature of 1273K become dense and spread over YSZ backbone after heating. Some NBCO clusters are also shown. We can expect lower surface area of the NBCO heated to higher temperature, leading to poor electrochemical cell performance due to the reduction of the number of the triple phase boundary and the limitation of the oxygen diffusion.[9]

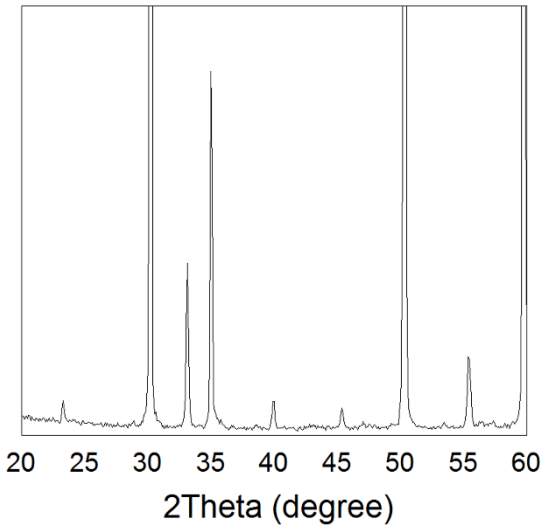

Figure 3.1 XRD patterns of NBCO-YSZ composites.

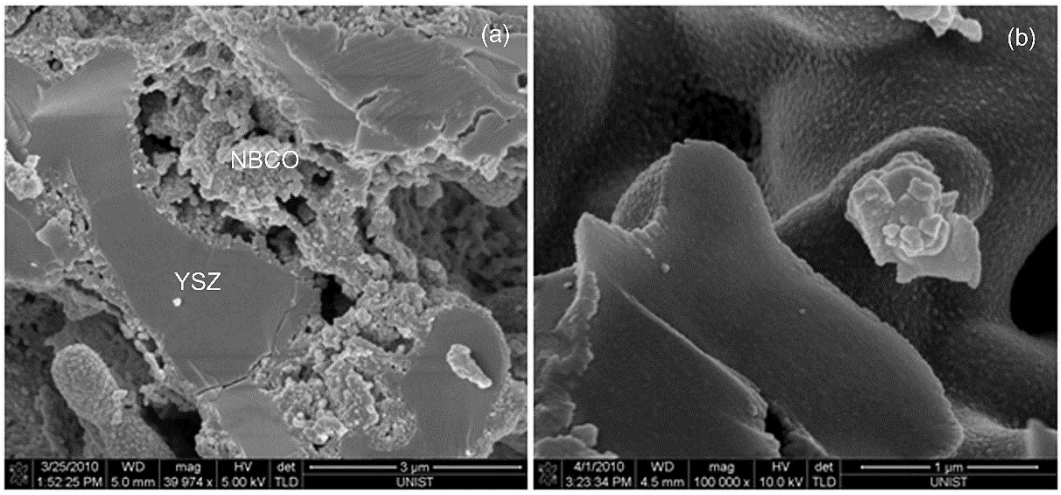

Figure 3.2 SEM images of $NdBaCo_2O_{5+\delta}$-YSZ composite annealed at (a) 1123 K and (b) 1273 K.

Equilibrium oxygen stoichiometries for the NBCO-YSZ composites are shown in Fig. 3.3 with the reference data.[13] The oxidation isotherms for three different temperatures have similar shapes suggesting that the reduction mechanisms of composites are analogous. However, as a temperature decreases, the decomposition $p(O_2)$ is getting lower. For example, the decomposition of NBCO-YSZ composites began around oxygen partial pressure($p(O_2)$) of 10^{-4} atm at 1023 K, and finally, the decomposition occurred at $p(O_2)$ of 10^{-5} atm. Meanwhile, the isotherm at 923 K has shown that the decomposition began below the $p(O_2)$ of 10^{-8} atm. It is very important information that the NBCO-YSZ cathode operating at $p(O_2)$ of 10^{-5} atm may undergo steep oxygen non-stoichiometry gradients and the corresponding instability of the structure according to the redox isotherm data in this study. Therefore, the NBCO-YSZ composites cannot be suitable as a cathode material at 1023 K due to the decomposition considering the stability.

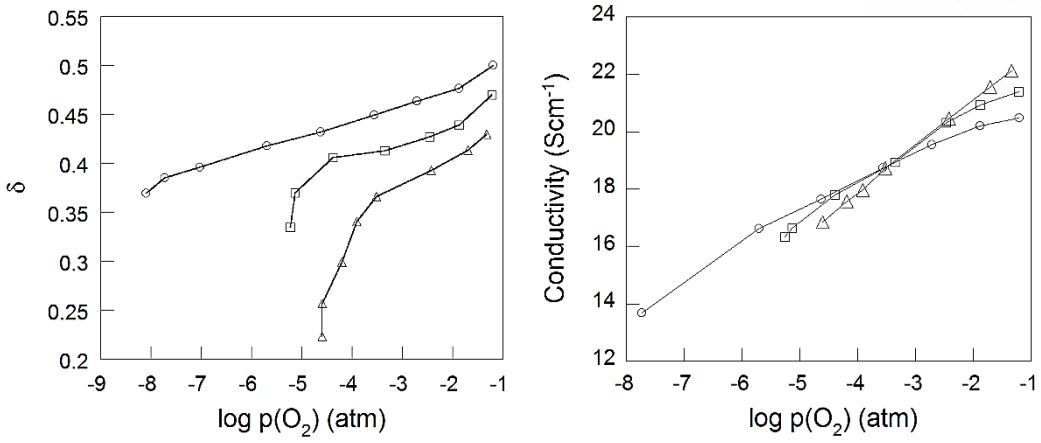

Figure 3.3 The isotherms of composites and the electrical conductivities of composites at (○) 923 K, (□) 973 K, and (△) 1023 K.

The 4-probe electrical conductivities for 43 wt% NBCO-YSZ composites calcined at 1023 K as a function of $p(O_2)$ at various temperatures (923 < T(K) < 1023) are shown in Fig. 3.3. Each datum point corresponds to the measured isotherm point in Fig. 3.2. The values of electrical conductivity of porous composites were above 20 S cm^{-1} in air and at various $p(O_2)$ in the temperature range of 923-1023 K. As $p(O_2)$ is lowered, the electrical conductivities decrease due to a decrease in the concentration of the mobile interstitial oxygen in the fluorite layers, indicating typical *p*-type electronic conductors.

The predominant defects in NBCO are the interstitial oxygens $O_i^{''}$ and the electronic holes $h^{\bullet} = O_o^{\bullet}$[14,15] and the following pseudo-chemical reaction shows the interaction between the defects and the atmosphere.

$$\frac{1}{2}O_2(g) + V_i^x + 2O_o^x \Leftrightarrow O_i^{''} + 2O_o^{\bullet} \qquad \text{Eqn. 3.4}$$

The electroneutrality produces the following equation:

$$2[O_i^{''}] = [O_o^{\bullet}] \qquad \text{Eqn. 3.5}$$

Therefore, the decrease in the oxygen interstitial concentration via lowering the $p(O_2)$ gives rise to the decrease in electronic holes which is associated with electronic conductivity of composites. Higher electrical conductivities were shown at high pressures ($p(O_2)$ > 0.1atm) and higher temperatures. However, the slope of the conductivity against $p(O_2)$ curve is dependent on temperature. The conductivities of the composites at 1023 K decrease at a much faster rate with decreases in $p(O_2)$ than the one at 923 K. This leads to an intersection of their conductivities vs. log $p(O_2)$ plots around $p(O_2) = 10^{-3}$ atm. Moreover, the slope at lower than the intersection $p(O_2)(10^{-3}$ atm) is getting steeper, which is

consistent with the steeper slope of the isotherms and the decomposition of the composites near the low $p(O_2)$. In other words, the conductivities at 1023 K are higher at higher $p(O_2)$ but are lower below 10^{-3} atm than that at 923 K. This indicates that decompositions begin to affect the electrical characteristics of the composites even before the end of the decomposition. This behavior might be ascribed to the oxygen order–disorder phase transition at the high temperature near this low $p(O_2)$.

Figure 3.4 shows $R/2\ln p(O_2)$ vs. $1/T$ plots and $RT\ln p(O_2)$ vs. T plots, respectively, for selected, δ. It is supposed that the interaction among randomly distributed defect species becomes more significant at higher δ since both curves show nonlinear behavior in this region. From the slopes of these plots, we obtain partial enthalpies from Eqn 3.6 and entropies of oxidation from thermodynamic relationships.

$$\Delta H = -\frac{R}{2}\frac{\delta \ln[p(O_2)]}{\delta(1/T)} \qquad \text{Eqn. 1.6}$$

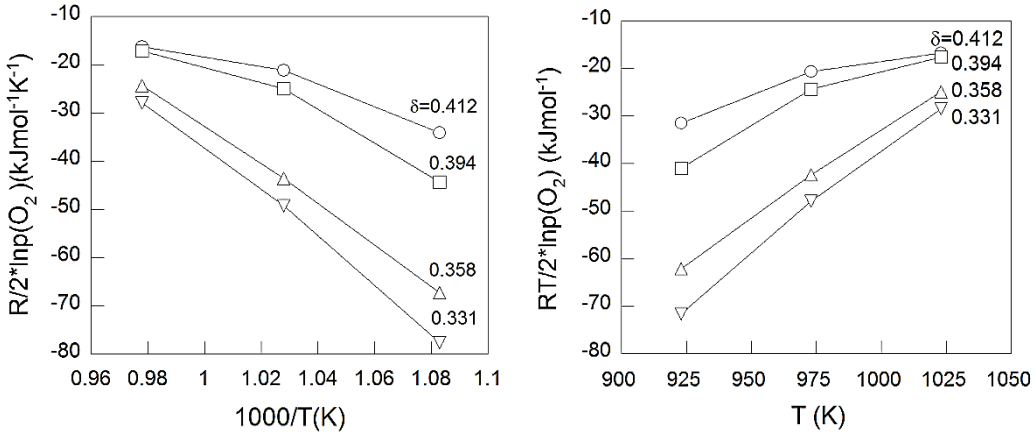

Figure 3.4 The relation between $R/2\ln p(O_2)$ and $1/T$ and $RT/2\ln p(O_2)$ and T of NBCO-YSZ composites.

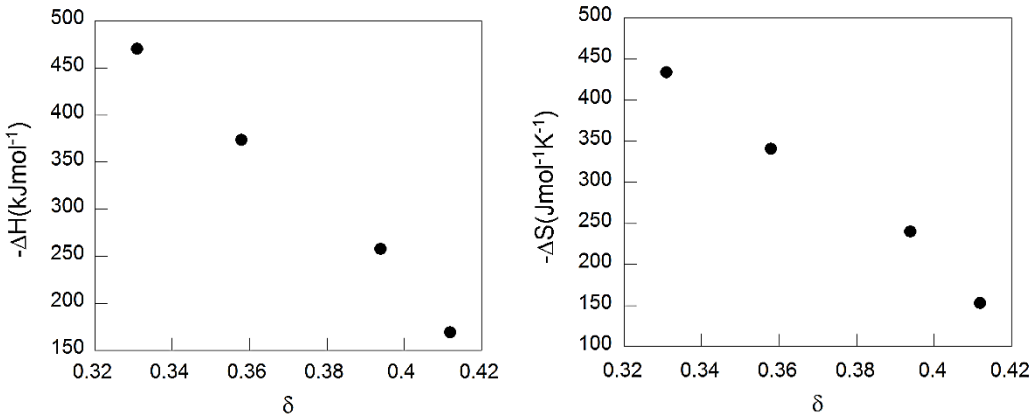

Figure 3.5 The partial molar enthalpy of oxidation (ΔH) at 973 K of NBCO-YSZ composites.

An examination of the partial enthalpies of oxidation for the NBCO samples, calculated by Eqn. 3.6, is shown in Fig. 3.5. The partial enthalpies of oxidation for the NBCO-YSZ composites range from -500 to -150 kJ/mol for excess oxygen (δ) between 0.32 and 0.42. The oxidation enthalpies ($-\Delta H$) are a strong function of oxygen non-stoichiometry in NBCO which means that the variation of the interaction among randomly distributed defect species is a crucial issue in this composites. The values of $-\Delta H$ become lower for higher δ implying lower energy needed for the formation of one interstitial oxygen, which means the oxidation of the cobalt (Co) in the lattice may destabilize the molecules near the defect species.

The partial molar entropies of oxidation, calculated from the differences of the Gibbs free energies and the enthalpies, are between -500 and -150 J/mol/K as shown in Fig. 3.5. Even though the enthalpy needed for the formation of one interstitial oxygen is lower for higher δ, the interstitial oxygen formation reaction itself is suppressed as excess oxygen increases, which is confirmed by the lower entropy at higher δ. In other words, it becomes more difficult for oxygen to exist in the composites as the amount of excess oxygen increases due to the variation of the interaction among randomly distributed defect species.[16]

3.4 Conclusions

The different redox properties of NBCO-YSZ composites at different oxidation state were explained by the coulometric titration. The oxidation enthalpies are a strong function of oxygen non-stochiometry in NBCO, δ, and are between -500 and -150 kJ/mol-O_2. The high entropy changes for NBCO with low δ seem to be explained by that the interstitial oxygen formation reaction is easier at this lower δ due to the smaller concentration of excess oxygen. The conductivities of the composites were above 20 S cm^{-1} in the temperature 923 K to 1023 K above 10^{-5} atm of $p(O_2)$, which is sufficient to provide low ohmic losses at the operating range of IT-SOFC cathode.

References

1 Shao, Z. P; Haile, S. M.; A high-performance cathode for the next generation of solid-oxide fuel cells. *Nature* **2004**, *431*, 170-173.

2 Tsai, T.; Perry, E.; Barnett, S.A.; Low-temperature solid-oxide fuel cells utilizing thin bilayer electrolytes, *J. Electrochem. Soc.*, **1997**, *144*, L130-L132.

3 Zhang, K.; Ge, L.; Ran, R.; Shao, Z.; Liu, S.; Synthesis, characterization and evaluation of cation-ordered $LnBaCo_2O_{5+\delta}$ as materials of oxygen permeation membranes and cathodes of SOFCs, *Acta Mater.*, **2008**, *56*, 4876-4889.

4 Kim, J.-H.; and Manthiram, A.; $LnBaCo_2O_{5+\delta}$ Oxides as Cathodes for Intermediate-Temperature Solid Oxide Fuel Cells, *J. Electrochem. Soc*., **2008**, *155*, B385-B390.

5 Kim, G.; Wang, S.; Jacobson, A. J.; Reimus, L.; Brodersen, P.; Mims, C. A.; *J. Mater. Chem*., 2007, 17, 2500.

6 Kim, G.; Wang, S.; Jacobson, A. J.; Yuan, Z.; Donner, W.; Chen, C. L.; Reimus, L.; Brodersen, P.; Mims, C. A.; Oxygen exchange kinetics of epitaxial $PrBaCo_2O_{5+\delta}$ thin films, *Appl. Phys. Lett*., **2006**, *88*, 024103-024106.

7 Ding, H.; Xue, X.; $PrBa_{0.5}Sr_{0.5}Co_2O_{5+\delta}$ layered perovskite cathode for intermediate temperature solid oxide fuel cells, *Electrochim. Acta*, **2010**, *55*, 3812-3816.

8 Kim, J. H.; Kim, Y.; Connor, P. A.; Irvine, J. T. S.; Bae, J.; Zhou, W.; Structural, thermal and electrochemical properties of layered perovskite $SmBaCo_2O_{5+\delta}$, a potential cathode material for intermediate-temperature solid oxide fuel cells, *J. Power Sources*, **2009**, *194*, 704-711.

9 Kim, G.; Vohs, J. M.; Gorte, R. J.; Enhanced reducibility of ceria-YSZ composites in solid oxide electrodes, *J. Mater. Chem*., **2008**, *18*, 2386-2390.

10 Gross, M. D.; Vohs, J. M.; Gorte, R. J.; Recent progress in SOFC anodes for direct utilization of hydrocarbons, *J. Mater. Chem*., **2007**, *17*, 3071-3077.

11 Vasala, S.; Lehtimaki, M.; Huang, Y. H.; Yamauchi, H.; Goodenough, J. B.; Karppinen, M.; Degree of order and redox balance in *B*-site ordered double perovskite oxides, $Sr_2MMoO_{6-\delta}$ (*M* = Mg, Mn, Fe, Co, Ni, Zn) *J. Solid State Chem.*, **2010**, *183*, 1007-1012.

12 Tsvetkov, D. S.; Sereda, V. V.; Zuev, A. Y.; Oxygen nonstoichiometry and defect structure of the double perovskite $GdBaCo_2O_{6-\delta}$, *Solid State Ionics*, **2010**, *180*, 1620-1625.

13 Kim, G.; *Doctoral thesis*, University of Houston, **2005**.

14 Mauvy, F.; Bassat, J.-M.; Boehm, E.; Manaud, J.-P.; Dordor, P.; Grenier, J.-C.; Oxygen electrode reaction on Nd2NiO4+d cathode materials: impedance spectroscopy study, *Solid State Ionics*, **2003**, *158*, 17-28.

15 Vashook, V. V.; Tolochko, S. P.; Yushkevich, I. I.; Makhnach, L. V.; Kononyuk, I. F.; Altenburg,

H.; Hauck. J.; Ullmann, H.; Oxygen nonstoichiometry and electrical conductivity of the solid solutions $La_{2-x}Sr_xNiO_y$ ($0 \leq x \leq 0.4$), *Solid State Ionics*, **1998**, *110*, 245-253.

16 Nakamura, T.; Yashiro, K.; Sato, K.; Mizusaki, J.; Oxygen nonstoichiometry and defect equilibrium in $La_{2-x}Sr_xNiO_{4+\delta}$, *Solid State Ionics*, **2009**, *180*, 368-376.

Chapter 4. Thermodynamic and Electrical Properties of Layered Perovskite $NdBaCo_{2-x}Fe_xO_{5+\delta}$-YSZ ($x$=0, 1) Composites for Intermediate Temperature SOFC Cathodes

4.1 Introduction

The solid oxide fuel cell (SOFC) is a promising energy conversion device that exploits the natural tendency of oxygen and fuel to react, which gives high efficiency, low emissions, and excellent fuel flexibility. The requirement for high operating temperatures (1073-1273 K), however, cause some problems such as high costs and high rate of formation of electrical and chemical insulating phases due to the solid state reaction between the SOFC components during the cell fabrication and operation. To make SOFC technologies commercially viable, therefore, the operating temperature must be reduced from high temperature (up to 1273 K) to intermediate temperature (873 to 1073 K).[1-4] For IT-SOFCs, cathode materials with high electrocatalytic activity for oxygen reduction should be developed because the cell performances at intermediate temperatures are often limited by polarization loss on the cathode.

Oxygen-deficient layered perovskite-related oxides, $LnBaCo_2O_{5+\delta}$(Ln = Pr, Nd, Sm, Gd), are getting attention as IT-SOFC cathode materials because of their high oxygen diffusivity and fast surface exchange kinetics along with high electrical conductivities. The ideal structure of these compounds can be generated by the stacking sequence ...$BaO/CoO_2/LnO_x/CoO_2$… (Ln = Pr, Nd, Sm, Gd), which is closely related to the cuprate superconductors depicted in Fig. 4.1. The oxygen non stoichiometry ($5+\delta$), crystal structure, and electrical property are determined by the difference in the ionic radii between the Ln^{3+} and Ba^{2+}. For instance, in the case of Sr^{2+} (ionic-radius, 1.44 Å) substitution for Ba^{2+} (ionic radius, 1.60 Å) in $GdBaCo_2O_{5+\delta}$, the oxygen content increase from 5.6 to 6.0 and an orthorhombic structure (*Pmmm*) becomes a tetragonal symmetry (*P4/mmm*) as the amount of Sr^{2+} increases.[5]

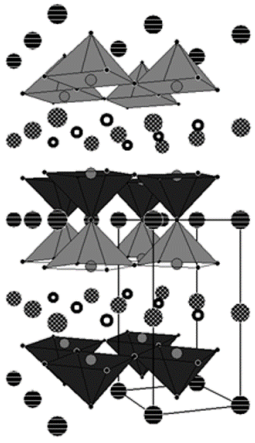

Figure 4.1 The structure of $NdBaCo_{2-x}Fe_xO_{5+\delta}$: each symbol indicates Neodymium (●), Barium (●), Cobalt (●), Oxygen (●), and Interstitial oxygen (○).

The excess oxygen atoms in the interstitial sites between the LnO layers may show highly anisotropic oxygen diffusion between the perovskite and fluorite structure, implying that the kinetics of mobile oxygen are faster between the a-b plane than the direction of the c axis.[6] Kim *et al*.[7] reported that $PrBaCo_2O_{5+\delta}$(PBCO) is a promising cathode for IT-SOFC which showed unusual fast oxygen diffusion and oxygen surface exchange kinetics at lower temperatures (773 to 973 K), resulting in a low cathodic polarization loss. Ding *et al*.[8] and Kim *et al*.[9] showed high electrical conductivity and better cell performance of the layered perovskite oxides, $LnBa_{0.5}Sr_{0.5}Co_2O_{5+\delta}$(Ln = Pr, Sm), substituting Sr for Ba. Recently, the effect of Fe partially substituted for Co in the NBCO on the structure, oxygen content and electrical properties has been reported by the Manthiram group.[10] They showed that the increase of Fe leads to a decrease in the thermal expansion coefficient (TEC) and electrical conductivity.

Our group recently characterized the isotherms and the corresponding electrical conductivities of the NBCO-YSZ composites, and the result indicated that NBCO showed a high electrical conductivity suitable to IT-SOFC application but less stability.[11] It is probable that Fe partially substituted for Co could potentially improve the stability of layered perovskite oxides due to the stronger Fe-O bond, which has been confirmed by recent studies.[12]

Recently Kim *et al.*[13] reported that the redox and electrical properties of the oxide-YSZ composites with YSZ prepared by impregnation, which are the actual configuration of the porous electrodes, could be completely different from those of the pure oxides. The impregnation method for electrode fabrication has been known to be very flexible, allowing the synthesis of anode and cathode composites with a wide range of compositions. For example, the porous YSZ scaffold is first sintered together with the electrolyte, and NBCF oxides are then added in subsequent steps by infiltrating the porous YSZ with solutions that contain the nanoparticles of the NBCF.[14] This method allows the formation of a long triple-phase boundary (TPB) where the oxygen reduction reaction occurs, which could provide higher performance of the composite electrode. The composites formed by impregnation have the advantage of forming a non-random structure leading to a good conductivity at relatively low metal loadings, and allowing much greater flexibility in preparing electrodes with a more complex microstructure.[15] The characteristics of NBCF-YSZ and/or NBCO-YSZ composites prepared by the impregnation method, however, have been completely unknown, to say nothing of the pure oxide, $NdBaCoFeO_{5+\delta}$.

The new electrodes can be developed faster if the thermodynamic and electrical characteristics of the materials are identified before the cell performance test. For example, a candidate cannot be used as an electrode if it possesses poor redox properties or can be decomposed at the operating temperature and/or the $p(O_2)$(atm) range of the IT-SOFC. Nevertheless, recent studies of the electrode materials have focused only on their structure, oxygen kinetics, electrochemical properties, or the fuel cell performance itself without considering the basic thermodynamic and electrical behavior.

The present work is devoted to evaluating the thermodynamic and electrical characteristics of a NBCF-YSZ composite as a promising candidate for an IT-SOFC cathode and to compare the properties with those of NBCO-YSZ composites. Different redox properties and electrical conductivities are revealed as important means to check the possibility for use as an IT-SOFC cathode material by the coulometric titration and 4-probe conductivity method.

4.2 Experimental

$NdBaCoFeO_{5+\delta}$-YSZ composites were synthesized by the impregnation of $NdBaCoFeO_{5+\delta}$ into a porous YSZ backbone, which was prepared by mixing YSZ powder (Tosoh corp. TZ-8Y), dispersant (Duramax3005, Rohm & Haas), binder (HA-12 and B-1000, Rohm & Haas), and pore former (Graphite, Alfa Aeser, 325 mesh). This solution of YSZ slurry was dried in air and sintered afterwards at 1773 K for 4 hours to yield porous YSZ with 65% porosity.[13] Stoichiometric amounts of $Nd(NO_3)_3 \cdot 6H_2O$ (Aldrich, 99.9%, metal basis), $Ba(NO_3)_2$ (Aldrich, 99+%), $Co(NO_3)_2 \cdot 6H_2O$ (Aldrich, 98+%), and $Fe(NO_3)_3 \cdot 6H_2O$ (Aldrich, 98+%) were dissolved in distilled water, which were infiltrated into the porous YSZ up to higher than 42 wt% loading. After firing in air at 723 and 1023 K, a $NdBaCoFeO_{5+\delta}$ phase was formed in porous YSZ.

The structure and the morphology of the composites were characterized by X-ray diffraction (XRD) and scanning electron microscopy (SEM). X-Ray powder diffraction measurements (Rigaku diffactormeter, Cu Ka radiation) were performed to confirm the structure with a scan rate of 0.5 ^{o} min^{-1} and the range $20^{o} < 2\theta < 60^{o}$.

The coulometric-titration was used to evaluate the exact redox state of a composite as a function of $p(O_2)$.[16,17] In coulometric titration, the $p(O_2)$ of the gases over an equilibrated sample are measured electrochemically with an oxygen sensor. The oxide-YSZ composite was placed in a sealed container at the temperature of interest and equilibrated sufficiently by passing a mixture of gases (for the present study, 5% O_2 in Ar) over it. Then the sample was isolated in the tube and the equilibrium $p(O_2)$ was measured with an oxygen sensor. The oxygen sensor was part of the container wall and could also be used to add or remove oxygen from the system through the application of a potential across the ion-conducting YSZ tube. Electrodes on either side of the YSZ tube were used to measure the potential across the membrane, and the potential could be related to the $p(O_2)$ through the Nernst Equation. A precise amount of charge could be passed across the tube using a BioLogic Potentiostat, with 1 Coulomb of charge equivalent to 2.6 μmol of O_2.

The yttria-stabilized zirconia (YSZ) tube (McDanel Advanced Ceramic Technologies, Z15410630) was used both to electrochemically pump oxygen out of the system and to sense the equilibrium $p(O_2)$ inside the tube. The electrical conductivity of the composite slabs, 2.2 mm x 5.3 mm x 9.9 mm in size,

was measured with a four-probe method with a BioLogic Potentiostat. The criterion we used for establishing equilibrium in coulometric titration was that the potential of the oxygen sensor changed by less than 1 mV h^{-1}.

Electrochemical performances of the $NdBaCo_{2-x}Fe_xO_{5+\delta}$ cathodes were evaluated with Ni-YSZ anode-supported single cells. The Ni-YSZ powder was prepared using nickel oxide (J. T. Baker), YSZ (Tosoh corp., TZ-8Y), and graphite (Aldrich, 20 micron) as a pore-former, and were then primarily mixed at 5.5 : 4.5 : 2.5 by weight and ball-milled together for 72 h in ethanol. Afterwards, NiO-YSZ pellet was prepared by grounding, pressing and sintering this mixture at 1473 K for 3 h. To improve the performance of the cell, the anode functional layer was coated by dipping the anode support into mixed slurries of NiO–YSZ (60 : 40 wt%) powder, isopropanol, and toluene followed by sintering at 1473 K for 3 h. The pellets were again coated by dense YSZ electrolyte layers through a dipping process and then sintered.

The pellets were again coated by dense YSZ electrolyte layers through a dipping process and then sintered. A second layer of the YSZ electrolyte was added via dipping in order to prevent the formation of pin-holes. The cathode layer was fabricated by tape casting with a slurry of YSZ powder (Tosoh corp. TZ-8Y), dispersant (Duramax 3005, Rohm & Haas), binder (HA-12 and B-1000, Rohm & Haas), and pore former (Graphite, Alfa Aeser, 325 mesh) and this slurry was laminated on the electrolyte layer. The thickness of the entire dense YSZ electrolyte layer was approximately 20 μm. The pellets, with an active electrode area of 0.36 cm^2, were finally sintered at 1773 K for 2 h under an air atmosphere. $NdBaCo_{2-x}Fe_xO_{5+\delta}$ solution was added onto the pellets using an infiltration technique, which was repeated until the loading reached 45 wt%. Finally, the cell was sintered at the same temperature, 1023 K, used during the preparation of slab samples.

Ag wires were attached to both electrodes using Ag paste as a current collector. The cells were fixed on a 10 mm diameter alumina tube using a ceramic adhesive (Aremco, Ceramabond 552). During the single cell test, humidified H_2 (3 % H_2O) was supplied to the anode side with a flow rate of 20 mL min^{-1} by first passing H_2 through a water bubbler, and the cathode was left open in air. AC impedance spectra under 800 mV and *I-V* polarization curves were determined at various currents in a frequency range of 1 mHz to 500 kHz and 14 mA AC perturbation using a BioLogic Potentiostat.

4.3 Results

The XRD patterns of the 42 wt% NBCF-YSZ composite calcined at 1023 K for 4 h in air are shown in Fig. 4.2. The XRD patterns demonstrate that the NBCF and YSZ are present as separate phases indicating no second phases between NBCF and YSZ at 1023 K.

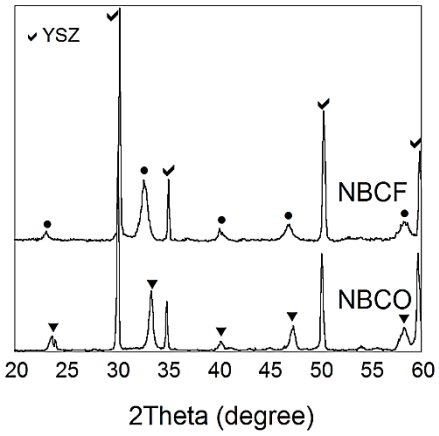

Figure 4.2 XRD pattern of the $NdBaCo_{2-x}Fe_xO_{5+\delta}$-YSZ composites.

SEM images of the YSZ backbone after sintering at 1773 K, the NBCF-YSZ, and the NBCO-YSZ composites formed after calcination at 1023 K are shown in Fig. 4.3a, b, and c, respectively. Due to the high wetness of NBCF oxides than that of NBCO oxides infiltrated into the YSZ backbone, the NBCF covers properly the surface of the YSZ pores, leading to a relatively thin dense layer with a thickness of 0.1 μm (Fig. 4.3b). In contrast, the NBCO-YSZ (Fig. 4.3c) consists of connected particles of NBCO, about 0.2 μm in size, coating the walls of the YSZ pores.

Figure 4.4 shows the Arrhenius plot of the electrical conductivity of the NBCO and NBCF composites. Both samples show an increase in electrical conductivity with an increasing temperature of up to 1123 K for NBCO and 1023 K for NBCF composites, respectively, implying typical semiconductor behaviour. A semiconductor-to-metal transition appears upon further increase of temperature as the behaviour of the electrical conductivity of both bulk NBCO and NBCF due to the decreasing concentration of interstitial oxygens.[10,16] However, Kim *et al*.[10] reported a lower transition temperature (573 K) for the bulk NBCF. This discrepancy can be explained by the fact that the interfacial interaction between YSZ and oxides might affect the electrical properties of the composites.

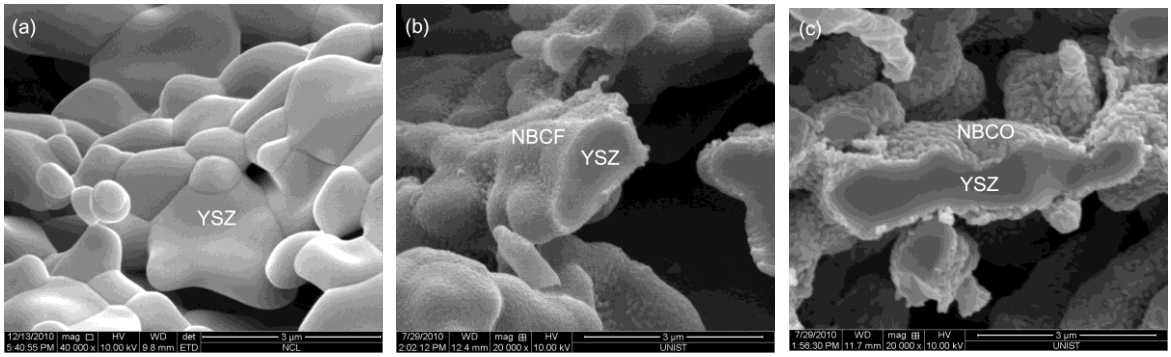

Figure 4.3 SEM images of the (a) YSZ backbone, the (b) NBCF-YSZ composite, and the (c) NBCO-YSZ composite annealed at 1023 K.

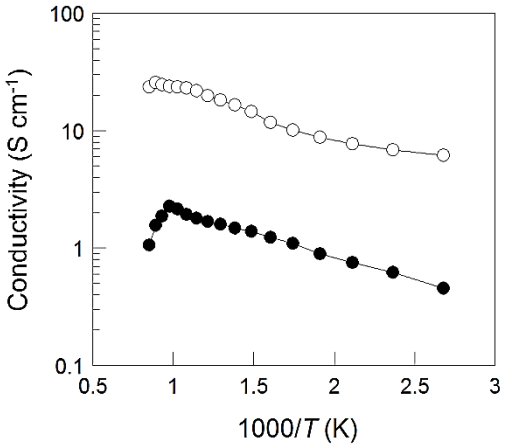

Figure 4.4 The electrical conductivity of the NBCF-YSZ composite (●) and the NBCO-YSZ composite (○) at various temperature from 1023 K to 373 K.

The 4-probe electrical conductivities for 42 wt% NBCF-YSZ composites calcined at 1023 K as a function of $p(O_2)$ at various temperatures (923<T(K)<1023) are shown in Fig. 4.5. Each datum point corresponds to the measured point in isotherms, Fig. 4.6. The electrical conductivities of the NBCF-YSZ composites range from 1 to 3 Scm^{-1} in air at various $p(O_2)$ and the temperature from 923 to 1023 K but are one order of magnitude smaller than those of NBCO-YSZ.

As $p(O_2)$ is lowered, the electrical conductivities decrease due to a dropping off of the concentration of the mobile interstitial oxygen in the fluorite layers, indicating typical *p*-type electronic conductor behavior. The predominant defects in NBCF and NBCO are the interstitial oxygens O_i'' and the electronic holes $h^{\bullet} = O_o^{\bullet}$,[18,19] according to the Kröger-Vink notation and the following pseudo-chemical reaction shows the interaction between the defects and the atmosphere.

$$\frac{1}{2}O_2(g) + V_i^{x} + 2O_o^{x} \Leftrightarrow O_i'' + 2O_o^{\bullet} \qquad \text{Eqn. 3.7}$$

The electroneutrality produces the following equation:

$$2[O_i''] = [O_o^{\bullet}] \qquad \text{Eqn. 3.8}$$

Therefore, the decrease in the interstitial oxygen concentration via lowering $p(O_2)$ gives rise to the decrease in electronic holes which is associated with the electronic conductivity of the composites. Higher electrical conductivities were expected at higher temperatures for pressure over around 10^{-5} atm.

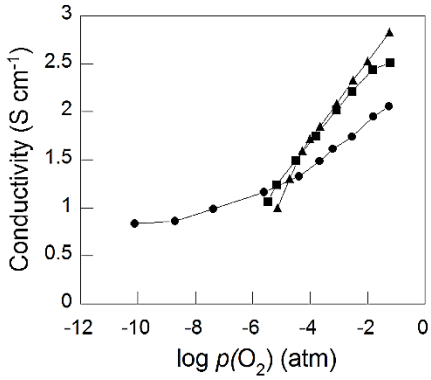

Figure 4.5 The electrical conductivities of the NBCF-YSZ composite in various $p(O_2)$ at (●) 923 K, (■) 973 K, and (▲) 1023 K.

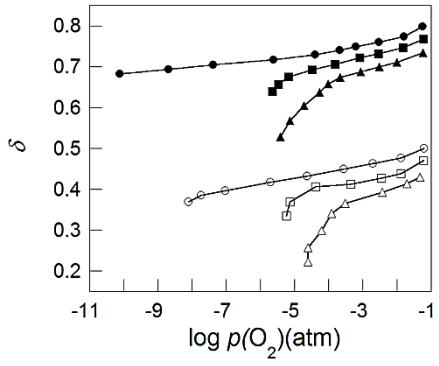

Figure 4.6 The isotherms of the NBCF-YSZ composites at (●) 923 K, (■) 973 K, and (▲) 1023 K and the isotherms of the NBCO-YSZ composites at (○) 923 K, (□) 973 K, and (△) 1023 K. Data for the NBCO were collected also by coulometric titration.[11]

However, the slope of the conductivity against the $p(O_2)$ curve is dependent on the temperature. The conductivities of the composites at 1023 K decrease at a much faster rate with decreases in $p(O_2)$ than those one at 923 K. This leads to an intersection of their conductivities vs. log $p(O_2)$ plots. Moreover, the slope at lower than the intersection $p(O_2)$ is getting steeper, which is consistent with the steeper slope of the isotherms and the decomposition of the composites near the low $p(O_2)$. This indicates that the decompositions begin to affect the electrical characteristics of the composites even before the end of the decomposition. This behavior might be ascribed to the oxygen order–disorder phase transition at the high temperature near this low $p(O_2)$.

Equilibrium oxygen non-stoichiometries for the NBCF composites are shown in Fig. 4.6 with the NBCO composites data of our previous work.[11] The oxidation isotherms for three different temperatures have similar shapes suggesting that the reduction mechanisms of the composites are analogous. As

temperature decreases, the decomposition $p(O_2)$ decreases. It is also shown that NBCF-YSZ has a higher redox stability than NBCO-YSZ down to a lower $p(O_2)$ at the same temperature due to the partial substitution of Fe for Co, as expected. For example, the NBCO composites start to decompose under oxygen partial pressure at 5.8×10^{-6} atm at 973 K, however, the NBCF composites do not decompose and can be reduced to a lower $p(O_2)$, 2.2×10^{-6} atm, at 973 K. The higher redox stability of the NBCF composites is a key factor for stable electrochemical properties of a cathode material for viable operation of the IT-SOFC at those operating conditions. Therefore, NBCF-YSZ composites can be more suitable as a cathode material than NBCO-YSZ in terms of stability.

$$\Delta H = -\frac{R}{2}\frac{\delta \ln[p(O_2)]}{\delta(1/T)} \qquad \text{Eqn. 3.9}$$

An examination of the partial molar enthalpies of oxidation for both composites, calculated by Eqn. 3.9, is shown in Fig. 4.7 as a function of δ (Fig. 4.7a) and $p(O_2)$ (Fig. 4.7b), respectively. The partial enthalpies of oxidation range from -640 to -240 kJ mol^{-1} for excess oxygen (δ) between 0.68 and 0.73 for the NBCF composites, but it is -500 to -150 kJ mol^{-1} between 0.32 and 0.42 for the NBCO composites for δ between 0.32 and 0.42.[11] The oxidation enthalpies ($-\Delta H$) are a strong function of oxygen non-stoichiometry in both composites, which means that the variation of the interaction among randomly distributed defect species is a crucial issue, and the behaviour of the composites cannot be taken as an ideal solution.[19] The values of $-\Delta H$ become lower for a higher δ, implying lower energy needed for the formation of an interstitial oxygen atom, from which it can be hypothesized that the lattice structures near the defect sites become destabilized more easily as the oxidation of cobalt (Co) and/or iron (Fe) in the lattice proceeds.

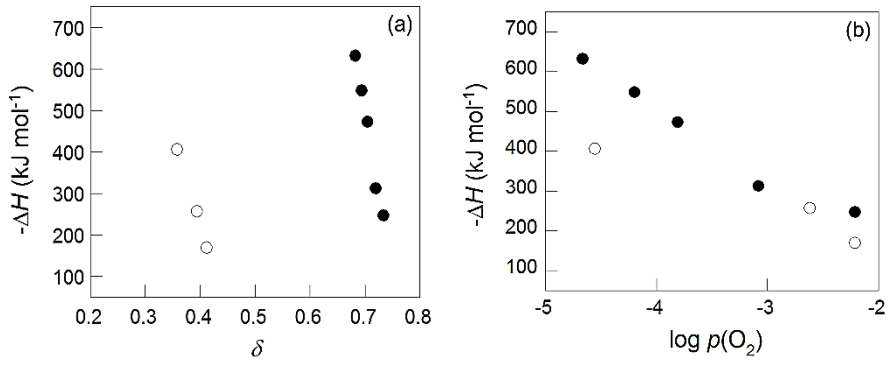

Figure 4.7 Partial molar enthalpy of oxidation (ΔH) at 973 K of the NBCF-YSZ composites (●) and the NBCO-YSZ composites (○). Data for the NBCO were collected also by coulometric titration.[11]

It is also confirmed that the NBCF composite is more stable than the NBCO composite considering the higher oxidation enthalpy near the cathode operating condition, which can also be found from the oxygen nonstoichiometry data in Fig. 4.6, partially explaining the comparative difficulty in oxidizing NBCF-YSZ composites.

The partial molar entropies of oxidation, calculated from the differences of the Gibbs free energies and the enthalpies, are shown in Fig. 4.8. The result means that the probabilities of the interstitial oxygen formation reaction itself decrease as excess oxygen increases. In other words, there are less sites for the interstitial oxygen formation reaction in the composites as the excess oxygen increases. The higher partial molar entropies for NBCF-YSZ than that of NBCO-YSZ means that more interstitial oxygen formation reaction can occur around the same $p(O_2)$.

To demonstrate the performance of the $NdBaCo_{2-x}Fe_xO_{5+\delta}$-YSZ composites cathodes are illustrated in Fig. 4.9. The *I-V* curves and the corresponding power density of $NdBaCo_{2-x}Fe_xO_{5+\delta}$-YSZ composites evaluated using YSZ as an electrolyte at 923, 973, 1023, and 1073 K, respectively, in humidified H_2. The open circuit voltages (OCVs) are near the theoretical value derived from the Nernst equation, which shows that the cell is well sealed with a gas-tight electrolyte. The maximum power densities of the cell with the NBCF cathode material were 0.362, 0.667, 1.034, and 1.438 W cm^{-2} at 923, 973, 1023, and 1073 K, respectively, as seen in Fig. 4.9(a). The performance is improved with partial substitution of Co with Fe, as seen in Fig. 4.9(a) and (b). For example, the maximum power density of the NBCO composite is 0.540 W cm^{-2} at 973 K and that of NBCF is much higher cell performance, 0.667 W cm^{-2} at the same temperature. It could be due to the extended electrochemical triple-phase boundary (TPB), where the electrochemical reaction occurs, as demonstrated in the microstructure of $NdBaCo_{2-x}Fe_xO_{5+\delta}$-YSZ composites in Fig. 4.3.

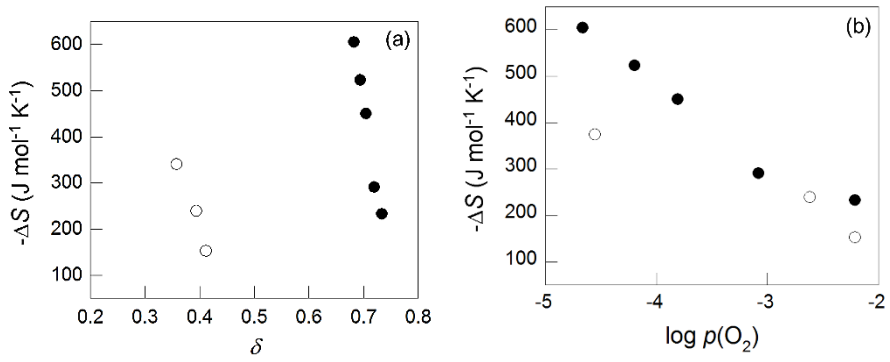

Figure 4.8 Partial molar entropy of oxidation (ΔS) at 973 K of the NBCF-YSZ composites (●) and the NBCO-YSZ composites (○). Data for the NBCO were collected also by coulometric titration.[11]

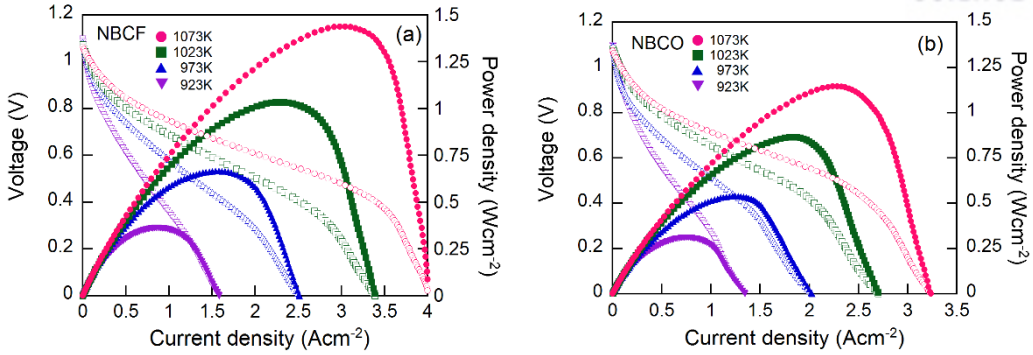

Figure 4.9 *I-V* curves and corresponding power density curves of single cell (Ni-YSZ/YSZ/$NdBaCo_{2-x}Fe_xO_{5+\delta}$-YSZ) in various temperatures.

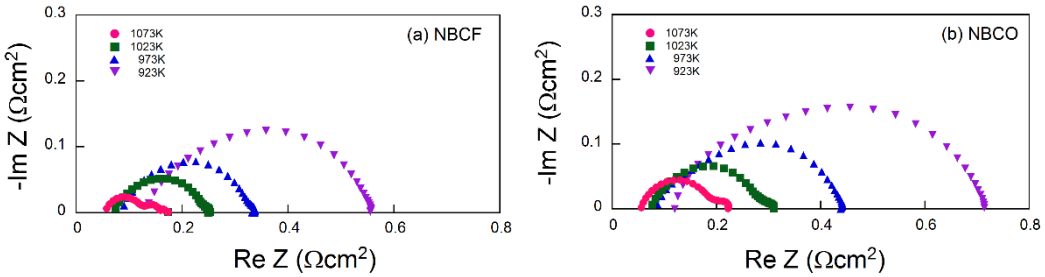

Figure 4.10 Impedance spectra of the single cell (Ni-YSZ/YSZ/ $NdBaCo_{2-x}Fe_xO_{5+\delta}$–YSZ) measured under 800mV using H_2 as fuel and ambient air as oxidant at various temperatures.

The electrochemical impedance spectra of $NdBaCo_{2-x}Fe_xO_{5+\delta}$-YSZ composites corresponding to the *I-V* polarization curve under 800 mV through 923-1073 K are presented in Fig. 4.10. In these spectra, the intercepts with the real axis at low frequency designate the total resistance of the cell and the value of high frequency is the ohmic resistance of the cell. The non-ohmic resistance of the cell designating the value between the two intercepts on the real axis determines cell performance associated with oxygen kinetics, such as oxygen diffusion and surface exchange rate. The non-ohmic resistance of the NBCF 0.418, 0.241, 0.174, and 0.116 Ωcm^2 at 923, 973, 1023, and 1073 K, respectively, as shown in Fig. 4.10(a). It is clear that the increase in operating temperature leads to a considerable reduction of the non-ohmic resistance due to the faster oxygen reduction kinetics. The non-ohmic resistance also decreases with the substitution of Fe from 0.353 down to 0.241 Ωcm^2 at 973 K. Therefore, NBCF is a superior candidate cathode material over NBCO in IT-SOFC applications.

4.4 Conclusion

The redox properties for NBCF-YSZ composites and NBCO-YSZ composites prepared by infiltration are evaluated by coulometric titration. The NBCF-YSZ composites can be more suitable as a cathode material than NBCO-YSZ in terms of stability. The higher oxidation enthalpies of the NBCF-YSZ

composites can explain the superior stability of the composites down to a lower oxygen partial pressure. The high entropy change for the NBCF composites can explain the high probability of forming interstitial oxygen near the same $p(O_2)$. The maximum power density of the NBCF-YSZ composite is higher than that of NBCO-YSZ composite, possibly due to the extended electrochemical TPB. The conductivity of NBCF was smaller than that of NBCO but it still seems to be satisfactory as an IT-SOFC cathode material.

References

1. Dusastre, V.; Kilner, J. A.; Optimisation of composite cathodes for intermediate temperature SOFC applications, *Solid State Ionics*, **1999**, *126*, 163-174.
2. Shao, Z. P; Haile, S. M.; A high-performance cathode for the next generation of solid-oxide fuel cells. *Nature* **2004**, *431*, 170-173.
3. Taracón, A.; Skinner, S. J.; Chater, R. J.; Hernández-Ramírez, F.; Kilner, J. A.; Layered perovskites as promising cathodes for intermediate temperature solid oxide fuel cells, *J. Mater .Chem.*, **2007**, *17*, 3175-3181.
4. Steele, B. C. H.; Heinzel, A.; Materials for fuel-cell technologies, *Nature*, **2001**, *414*, 345-352.
5. Kim, J.-H.; Proda, F.; Manthiram, A.; Characterization of $GdBa_{1-x}Sr_xCo_2O_{5+\delta}$ ($0 \leq x \leq 1.0$) Double Perovskites as Cathodes for Solid Oxide Fuel Cells, *J. Electrochem. Soc.* **2008**, *155*, B1023-B1028.
6. Kim, G.; Wang, S.; Jacobson, A. J.; Reimus, L.; Brodersen, P.; Mims, C. A.; *J. Mater. Chem.*, 2007, 17, 2500.
7. Kim, G.; Wang, S.; Jacobson, A. J.; Yuan, Z.; Donner, W.; Chen, C. L.; Reimus, L.; Brodersen, P.; Mims, C. A.; Oxygen exchange kinetics of epitaxial $PrBaCo_2O_{5+\delta}$ thin films, *Appl. Phys. Lett*., **2006**, *88*, 024103-024106.
8. Ding, H.; Xue, X.; $PrBa_{0.5}Sr_{0.5}Co_2O_{5+\delta}$ layered perovskite cathode for intermediate temperature solid oxide fuel cells, *Electrochim. Acta*, **2010**, *55*, 3812-3816.
9. Kim, J. H.; Kim, Y.; Connor, P. A.; Irvine, J. T. S.; Bae, J.; Zhou, W.; Structural, thermal and electrochemical properties of layered perovskite $SmBaCo_2O_{5+\delta}$, a potential cathode material for intermediate-temperature solid oxide fuel cells, *J. Power Sources*, **2009**, *194*, 704-711.
10. Kim, Y. N.; Kim, J. H.; Manthiram, A.; Effect of Fe subtitution on the structure and properties of $LnBaCo_{2-x}Fe_xO_{5+\delta}$ (Ln = Nd and Gd) cathodes, *J. Power Soures*, **2010**, *195*, 6411-6419.
11. Yoo, S.; Shin, J.; Kim, G.; Thermodynamic and electrical characteristics of $NdBaCo_2O_{5+\delta}$ at varous oxidation and reduction states, *J. Mater. Chem*. **2011**, *21*, 439-443.
12. Stevenson, J.W.; Armstrong, T.R.; Carneim, R.D.; Pederson, L.R.; Weber, W.J.; Electrochemical Properties of Mixed Conducting Perovskites $La_{1-x}M_xCo_{1-y}Fe_yO_{3-\delta}$ (M = Sr, Ba, Ca), *J. Electrochem. Soc*., **1996**, *143*, 2722-2729.
13. Kim, G.; Vohs, J. M.; Gorte, R. J.; Enhanced reducibility of ceria-YSZ composites in solid oxide electrodes, *J. Mater. Chem*., **2008**, *18*, 2386-2390.
14. Küngas, R.; Bidrawn, F.; Vohs, J. M.; Gorte, R. J.; Doped-Ceria Diffusion Barriers Prepared by Infiltration for Solid Oxide Fuel Cells, *Electrochem. Solid-State Lett*. 2010, 13, B87-B90.
15. Gross, M. D.; Vohs, J. M.; Gorte, R. J.; Recent progress in SOFC anodes for direct utilization

of hydrocarbons, *J. Mater. Chem.*, **2007**, *17*, 3071-3077.

16. Vasala, S.; Lehtimaki, M.; Huang, Y. H.; Yamauchi, H.; Goodenough, J. B.; Karppinen, M.; Degree of order and redox balance in *B*-site ordered double perovskite oxides, $Sr_2MMoO_{6-\delta}$ (*M* = Mg, Mn, Fe, Co, Ni, Zn) *J. Solid State Chem.*, **2010**, *183*, 1007-1012.
17. Tsvetkov, D. S.; Sereda, V. V.; Zuev, A. Y.; Oxygen nonstoichiometry and defect structure of the double perovskite $GdBaCo_2O_{6-\delta}$, *Solid State Ionics*, **2010**, *180*, 1620-1625.
18. Mauvy, F.; Bassat, J.-M.; Boehm, E.; Manaud, J.-P.; Dordor, P.; Grenier, J.-C.; Oxygen electrode reaction on Nd2NiO4+d cathode materials: impedance spectroscopy study, *Solid State Ionics*, **2003**, *158*, 17-28.
19. Vashook, V. V.; Tolochko, S. P.; Yushkevich, I. I.; Makhnach, L. V.; Kononyuk, I. F.; Altenburg, H.; Hauck. J.; Ullmann, H.; Oxygen nonstoichiometry and electrical conductivity of the solid solutions $La_{2-x}Sr_xNiO_y$ ($0 \leq x \leq 0.4$), *Solid State Ionics*, **1998**, *110*, 245-253.

‘

Chapter 5. Electrical Properties, Thermodynamic Behavior, and Defect Analysis of $La_{n+1}Ni_nO_{3n+1+\delta}$ Infiltrated into YSZ Scaffolds as Cathodes for Intermediate Temperature SOFCs

5.1 Introduction

A solid oxide fuel cell (SOFC) is an electrochemical device for chemical-to-electrical energy conversion with high efficiency, low emissions, and excellent fuel flexibility. The requirement for high operating temperature (1073-1273 K) of conventional SOFCs, however, leads to notable problems such as high costs and high rate of degradation due to interactions between cell components during cell fabrication and operation. To overcome these problems, much effort has been devoted to lowering the SOFC operating temperature toward an intermediate range (873 to 1073 K). One of the challenges for IT-SOFC is to develop cathode materials with high electrocatalytic activity for oxygen reduction at these temperatures.[1-5]

While $La_{1-x}Sr_xMnO_3$ (LSM) has been widely used as a cathode material for SOFCs based on YSZ electrolytes at high temperatures,[3,4] it is inadequate for use in an intermediate temperature range due to reduced ionic and electronic conductivity and diminished catalytic activity at lower temperatures.[5-7]

Recently, mixed ionic and electronic conductors (MIECs) have received tremendous attention as potential cathodes for IT-SOFCs. MIECs based on transition metal (e.g., Mn, Fe, Co, and Ni) oxides have been extensively investigated. Among various MIECs, cobalt containing oxides showed superior electrocatalytic activity than oxides with predominant electronic conductivity (and little ionic conductivity) such as lanthanum manganese. In particular, $La_{1-x}Sr_xCo_{1-y}Fe_yO_{3-\delta}$ (LSCF)-based cathodes have attracted much attention for IT-SOFCs. However, the long-term stability of LSCF-based cathodes is still a concern.[6-8]

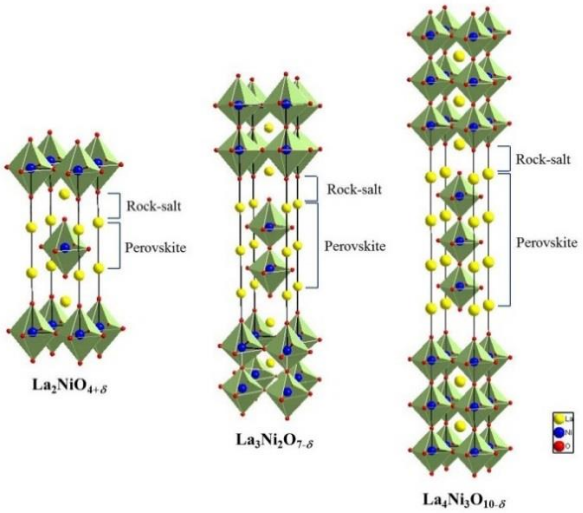

Figure 5.1 The structure of the $La_{n+1}Ni_nO_{3n+1}$ (n = 1, 2, and 3)

As a mixed conductor derived from the K_2NiF_4-type materials, La_2NiO_4 has attracted significant attention for possible application as IT-SOFC cathodes. Its advantages include high oxygen ionic and electronic conductivity, moderate thermal expansion coefficient (TEC), and high electrocatalytic activity toward oxygen reduction under oxidizing conditions.[9-11] Other materials such as lanthanum cobaltite perovskite also exhibit good conductivities; however, the large thermal expansion mismatch with other cell components may lead to thermo-mechanical problems.

The Ruddlesden-Popper compounds are comprised of alternating perovskite and rock-salt layers, as shown in Figure 1. The number of perovskite layers increases with *n* in this structure, leading to the formation of higher order Ruddlesden-Popper phases, $La_3Ni_2O_7$ and $La_4Ni_3O_{10}$, allowing faster ionic and electronic transport.[6,9] These effects are primarily attributed to increased concentration of Ni-O-Ni bonds, which are responsible for electronic conduction due to progressive delocalization of the *p*-type electronic charge carriers, and enhanced vacancy-migration or oxygen ion diffusivity. [12-15]

Currently, much of the study on $La_{n+1}Ni_nO_{3n+1+\delta}$ (n = 1, 2, or 3) focused on the structure and electrochemical properties of the bulk phases, with little attention to the basic thermodynamic properties. To date, the characteristics of $La_{n+1}Ni_nO_{3n+1+\delta}$ infiltrated into a scaffold of YSZ and the actual configuration of a porous cathode fabricated by infiltration, are still unknown. Because of the unique microstructures and possible interactions between the two phases, the behaviour of this $La_{n+1}Ni_nO_{3n+1+\delta}$ -YSZ composite could be very different from that of a pure $La_{n+1}Ni_nO_{3n+1+\delta}$ phase. Further, redox properties related to oxygen thermodynamics such as oxidation enthalpies and entropies of $La_{n+1}Ni_nO_{3n+1}$ (n = 1, 2, and 3), and redox stability have not been reported for the intermediate temperature range.

In this study, we characterized non-stoichiometric variations of oxygen and electrical conductivities of $La_{n+1}Ni_nO_{3n+1+\delta}$ (n = 1, 2, and 3) infiltrated into porous YSZ as a function of oxygen partial pressure in a temperature range of 923-1023 K. Redox behavior was evaluated using coulometric titration and the electrical conductivity was determined using 4-probe conductivity measurement.

5.2. Experimental

$La_{n+1}Ni_nO_{3n+1}$ (n = 1, 2, and 3) composites were prepared by the infiltration of $La_{n+1}Ni_nO_{3n+1}$ (n = 1, 2, and 3) into porous YSZ (Tosoh corp. TZ-8Y). The porous YSZ slab was prepared by mixing YSZ powder, dispersant (Duramax3005, Rohm & Haas), binder (HA-12 and B-1000, Rohm & Haas), and pore former (Graphite, Alfa Aeser, 325 mesh). This solution of YSZ slurry was dried and sintered afterwards at 1773 K to yield porous YSZ with 65% porosity. Stoichiometric amounts of $La(NO_3)_3 \cdot 6H_2O$ (Aldrich, 99.9%), $Ni(NO_3)_2 \cdot 6H_2O$ (Aldrich), and citric acid were dissolved in distilled water, which were infiltrated into the porous YSZ up to higher than 45wt% loading. After firing in air at 723 K and 1123 K, $La_{n+1}Ni_nO_{3n+1}$ (n = 1, 2, and 3) phase was formed in the porous YSZ.

The $La_{n+1}Ni_nO_{3n+1}$ (n = 1, 2, and 3) composites were characterized using X-ray diffraction (XRD) and scanning electron microscopy (SEM). X-ray powder diffraction measurements (Rigaku diffractometer, Cu Ka radiation) was performed to confirm the structure with a scan rate of 0.5^o min^{-1} and a range of $20^o < 2\theta < 60^o$.

The oxidation/reduction state of a composite can be characterized precisely by coulometric titration as a function of $p(O_2)$.[16,17] This involves placing the oxide sample in a sealed container, separated from the atmosphere by an O^{2-}-conducting membrane such as yttria-stablized zirconia (YSZ). The YSZ tube (McDanel Advanced Ceramic Technologies, Z15410630) was used both to pump oxygen out of the system and to sense the equilibrium $p(O_2)$ inside the tube. The $La_{n+1}Ni_nO_{3n+1}$ (n = 1, 2, and 3) composite was located in a sealed container at various temperatures of interest and equilibrated by subjecting it to a flow of 5% O_2 in Ar. The composite was then isolated in the tube and the equilibrium $p(O_2)$ was measured with an oxygen sensor. Electrodes on both sides of the YSZ tube were used to measure the potential across the membrane, and the potential could be related to the $p(O_2)$ through the Nernst Equation. A specific amount of charge could be passed across the tube using a BioLogic Potentiostat, with 1 Coulomb of charge being equivalent to 2.6 μmol of O_2.

The electrical conductivity of the composite slabs, 2mm x 5mm x 10mm in size, were measured in air by the four-probe method with a BioLogic Potentiostat. The measurements were performed starting from 1023 to 373 K with 323 K measurement intervals.

5.3 Results

5.3.1 XRD and SEM

Shown in Figure 2 are typical XRD patterns of $La_{n+1}Ni_nO_{3n+1}$(42 wt%) -YSZ composites fired at 1123 K, suggesting that the $La_{n+1}Ni_nO_{3n+1}$ compounds have a Ruddlesden-Popper structure and the two main phases are $La_{n+1}Ni_nO_{3n+1}$ and YSZ without observable peaks of other phases. The XRD data suggest that there were no observable chemical reactions between $La_{n+1}Ni_nO_{3n+1}$ and YSZ under the processing conditions.

As is well known, the microstructure of an electrode may sensitively influence the reaction kinetics, charge and mass transport processes, and hence fuel cell performance. For example, three phase boundaries (TPBs) at the electrode/electrolyte interfaces are the most active sites for electrochemical reactions in SOFCs. Smaller grain size often results in longer TPB length and potentially higher electrochemical performance.[16] SEM images of the $La_{n+1}Ni_nO_{3n+1}$-YSZ composites fired at 1123 K are presented in Figures 3a, b, and c, respectively, for n = 1, 2, and 3. It is clearly seen that the grain size of the $La_{n+1}Ni_nO_{3n+1}$ becomes smaller with the increasing value of n, leading to increased length of TPBs.

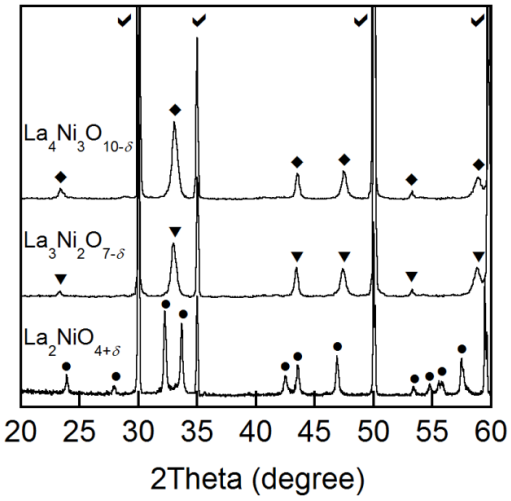

Figure 5.2 XRD pattern of $La_{n+1}Ni_nO_{3n+1}$ (n = 1, 2, and 3)-YSZ composites sintered at 1123 K : each symbol indicates $La_{n+1}Ni_nO_{3n+1}$ (n=1, 2, and 3), $La_2NiO_{4+\delta}$(●), $La_3Ni_2O_{7-\delta}$(▼), $La_4Ni_3O_{10-\delta}$(◆), and YSZ(✔).

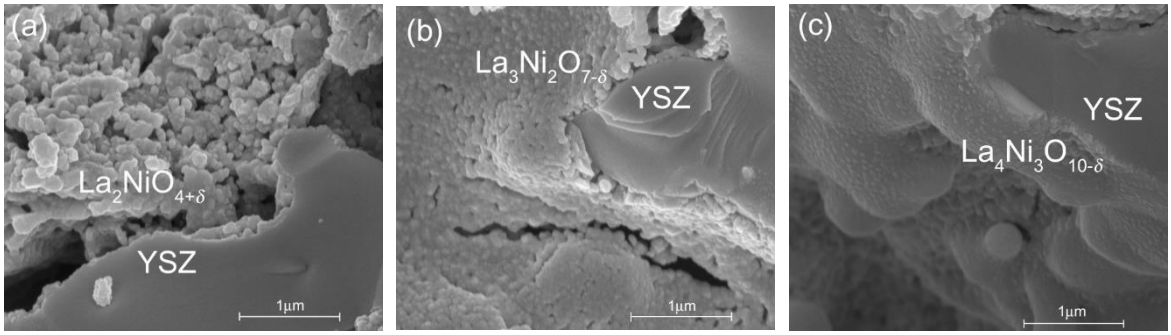

Figure 5.3 SEM images of the (a) $La_2NiO_{4+\delta}$-YSZ composite, the (b) $La_3Ni_2O_{7-\delta}$-YSZ composite, and the (c) $La_4Ni_3O_{10-\delta}$-YSZ composite annealed at 1123 K.

5.3.2 Thermodynamic characterization

Shown in Fig. 5.4 are the equilibrium oxygen nonstoichiometries for $La_{n+1}Ni_nO_{3n+1}$ infiltrated in YSZ determined by coulometric titration[17,18] as a function of $p(O_2)$ in a temperature range of 923-1023 K. In general, oxygen interstitials (O_i'') are considered the dominating defects for n = 1 whereas oxygen vacancies ($V_o^{\bullet\bullet}$) are the main defects for n = 2 and 3 due to the increase of perovskite layers in the structure.

There is a considerable change in oxygen nonstoichiometry throughout the $p(O_2)$ range for all compounds. The data show that the isotherms of $La_{n+1}Ni_nO_{3n+1}$-YSZ composites (n = 1, 2, and 3) have similar shapes, suggesting that the reduction mechanisms of the composites are quite similar. As

temperature decreases, the decomposition $p(O_2)$ becomes lower. With an increase of n, the isotherms are extended to the left, indicating that $La_4Ni_3O_{10-\delta}$ has higher redox stability than $La_2NiO_{4+\delta}$ down to a lower $p(O_2)$ at the same temperature. This is due possibly to the higher number of perovskite layers in $La_4Ni_3O_{10-\delta}$ and, accordingly, stronger interaction between the molecules in the lattice.

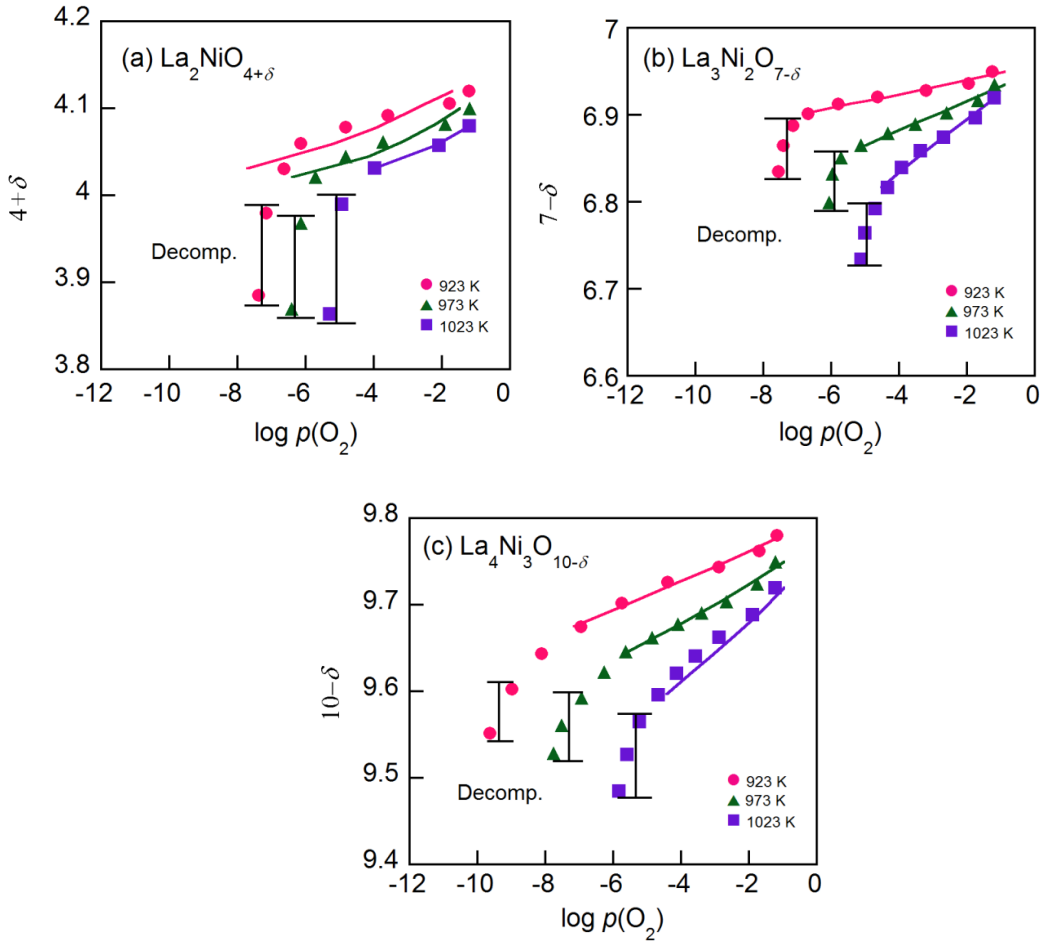

Figure 5.4 The isotherms of the $La_{n+1}Ni_nO_{3n+1}$ (n = 1, 2, and 3)-YSZ composites at 923-1023 K, (a) $La_2NiO_{4+\delta}$, (b) $La_3Ni_2O_{7-\delta}$ and (c) $La_4Ni_3O_{10-\delta}$. The solid curves are fitting curves calculated by the proposed defect model using data only before decomposition.

The partial molar enthalpy and entropy of oxygen can be calculated from the slopes of the isotherms. The Gibbs free energy, ΔG, is related to the equilibrium constant, K, and $p(O_2)$ as follows,

$$\Delta G = -RT\ln K = \frac{1}{2}RT\ln p(O_2) \qquad \text{Eqn. (1)}$$

At a constant δ, the partial molar enthalpy of oxygen at various temperatures is shown by the Gibbs-Helmholtz equation.

$$-\Delta H = \frac{\partial\left(\frac{\Delta G}{T}\right)}{\partial\left(\frac{1}{T}\right)} = \frac{R}{2}\frac{\partial \ln[p(O_2)]}{\partial\left(1/T\right)}\Big|_{\delta} \quad \text{Eqn. (2)}$$

And the partial molar entropy can be obtained by using the Maxwell relation as follows.

$$\Delta S = -\frac{\partial \Delta G}{\partial T} = \left(\frac{R}{2}\right)\left(\frac{\partial T \ln p(O_2)}{\partial T}\right)\Big|_{\delta} \quad \text{Eqn. (3)}$$

The partial enthalpies of oxidation for the $La_{n+1}Ni_nO_{3n+1}$-YSZ composites (n = 1, 2, and 3), calculated from Equation (2), are presented in Fig. 5.5. The oxidation enthalpies (-ΔH) are a strong function of oxygen non-stoichiometry in $La_{n+1}Ni_nO_{3n+1}$ (n = 1, 2, and 3).

The partial molar enthalpies of oxidation at 10^{-5} atm are plotted in Fig. 5.6. The higher partial molar enthalpy for $La_4Ni_3O_{10-\delta}$-YSZ relative to that of $La_{n+1}Ni_nO_{3n+1}$ (n = 1 and 2) means that it would be more stable at roughly the same $p(O_2)$.

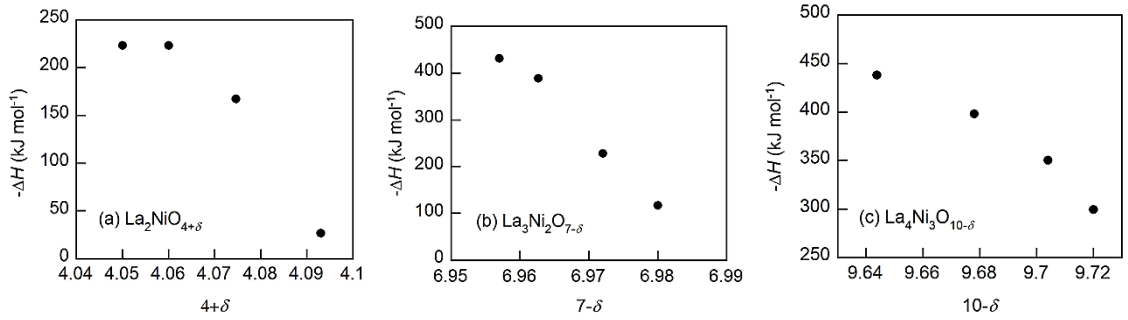

Figure 5.5 Partial molar enthalpy of oxidation (ΔH) at 973 K of the $La_{n+1}Ni_nO_{3n+1}$ (n = 1, 2, and 3)-YSZ composites, (a) $La_2NiO_{4+\delta}$, (b) $La_3Ni_2O_{7-\delta}$ and (c) $La_4Ni_3O_{10-\delta}$.

5.3.2.1 Hyperstoichiometric $La_2NiO_{4+\delta}$

The partial molar enthalpies of oxidation for the $La_2Ni_1O_{4+\delta}$-YSZ composites range from -20 to -250 kJ mol^{-1}. The values of -ΔH become smaller for larger δ, implying lower energy is needed for the formation of one interstitial oxygen. Oxidation of the nickel ions in the lattice would then destabilize the local structure near the defected sites. In other words, the interatomic forces between ions inside the lattice may become weaker in the vicinity of the defected sites.

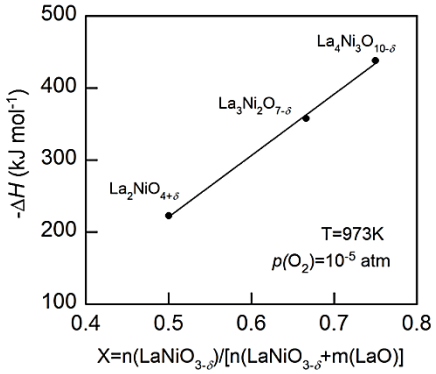

Figure 5.6 Partial molar enthalpy of oxidation (ΔH) at 973 K of the $La_{n+1}Ni_nO_{3n+1}$ (n = 1, 2, and 3)-YSZ composites at $p(O_2) = 10^{-5}$ atm.

The partial molar entropies of oxidation, calculated from the differences in the Gibbs free energies and the enthalpies, are presented in Fig. 5.7. The values of $-\Delta S$ become smaller for higher δ, implying that the probability for interstitial oxygen formation decreases with excess oxygen. In other words, there are fewer sites for the interstitial oxygen formation reaction in the composites as the amount of excess oxygen increases (Fig. 5.7a). [9, 18-20]

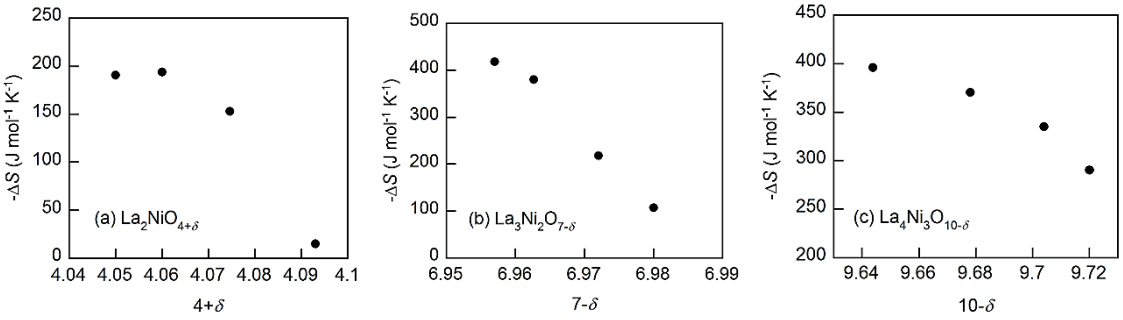

Figure 5.7 Partial molar entropy of oxidation (ΔS) at 973 K of the $La_{n+1}Ni_nO_{3n+1}$ (n = 1, 2, and 3)-YSZ composites, (a) $La_2NiO_{4+\delta}$, (b) $La_3Ni_2O_{7-\delta}$ and (c) $La_4Ni_3O_{10-\delta}$.

5.3.2.2 Oxygen deficient $La_3Ni_2O_{7-\delta}$ and $La_4Ni_3O_{10-\delta}$

The partial molar enthalpies of oxidation for the $La_{n+1}Ni_nO_{3n+1}$-YSZ composites (n = 2, and 3) range from -100 to -430 kJ mol^{-1} and -300 to -450 kJ mol^{-1}, respectively. However, the values of $-\Delta H$ become larger for higher δ, implying higher energy is needed for release of the oxygen inside the lattice (*i.e.*, oxygen vacancy formation) as the reduction proceeds.

It can also be argued that fewer sites will be available for oxygen vacancy formation in the composites as the concentration of oxygen vacancy increases. This is consistent with the finding that the values of $-\Delta S$ become smaller for higher δ (Fig. 5.7b and c). [9, 21]

5.3.3 Defect Analysis

5.3.3.1 Hyperstoichiometric $La_2NiO_{4+\delta}$

The predominant point defects in $La_2NiO_{4+\delta}$ are, expectedly, oxygen interstitials O_i'' and electron holes.[22] The concentration of oxygen vacancies is considered negligible here. The following pseudo-chemical reaction shows the equilibrium between oxygen interstitials, electron holes, and the surrounding oxygen gas molecules.

$$\frac{1}{2}O_2(g) \leftrightarrow O_i'' + 2h^{\bullet} \qquad \text{Reaction (4)}$$

Thus, electroneutrality approximation requires that the number of electron holes should be about twice the number of oxygen interstitials.

$$[h^{\bullet}] = 2[O_i''] = 2\delta \qquad \text{Reaction (5)}$$

In terms of δ and $p(O_2)$, the equilibrium constant for reaction (4) can be expressed as

$$K = \frac{[O_i''][h^{\bullet}]^2}{p(O_2)^{1/2}}\gamma_1{\gamma_2}^2 = \frac{(\delta)(2\delta)^2}{p(O_2)^{1/2}}\gamma_1{\gamma_2}^2 \qquad \text{Reaction (6)}$$

where γ_1 and γ_2, denote the activity coefficients of O_i'' and $h^{\bullet}$, respectively.

Thus, the Gibbs free energy change for reaction (4) can be expressed as follows.

$$\Delta G = -RT\ln K = -RT\ln\frac{(\delta)(2\delta)^2}{p(O_2)^{1/2}} - RT\ln(\gamma_1{\gamma_2}^2) \qquad \text{Eqn. (7)}$$

The second term in Equation (7) represents the deviation from the Gibbs free energy change for an ideal system (activity coefficient = 1). As a first order approximation, the deviation is assumed to be a linear function of the oxygen nonstoichiometry, δ.[19, 22]

$$\Delta G_{ex} = -RT\ln\gamma_1{\gamma_2}^2 \equiv a\delta \qquad \text{Eqn. (8)}$$

Thus, the constant a reflects the degree of interaction between the defects and the lattice ions. A positive a suggests that the formation of interstitial oxygen is easier than in an ideal system while a

negative *a* implies that it becomes more difficult than in an ideal system.[19] As *a* approaches zero, the system reduces to the ideal system (*i.e.*, there is no interactions between the defects and the lattice ions).

In light of Equation (8), Equation (7) can be rewritten as

$$p(O_2) = \frac{16\delta^6}{K^2}\left\{exp\left(\frac{-a\delta}{RT}\right)\right\}^2 \qquad \text{Eqn. (9)}$$

The relationship between δ and $p(O_2)$ as described by Equation (9) can then be used to estimate the parameters *K* and *a* from experimental data.

The formation of oxygen interstitials in the $La_2NiO_{4+\delta}$-YSZ composites is electrically compensated by the formation of electron holes to satisfy electroneutrality. The oxygen non-stoichiometry data for all $La_2NiO_{4+\delta}$-YSZ composites were fitted to the models described above. The theoretical curves calculated for $La_2NiO_{4+\delta}$-YSZ using Equation (9) are presented as solid lines in Fig. 5.4a, with the fitted *K* and *a* values listed in Table 1. Although there was some small deviation, the observed nonstoichiometric behaviour of $La_2NiO_{4+\delta}$-YSZ can be well explained using the proposed defect model over a wide range of $p(O_2)$ except the area where decomposition is expected.

Table 5.1 The fitting parameters providing the best fit to the measurements ($La_2NiO_{4+\delta}$)

$La_2NiO_{4+\delta}$	**log *K***	***a* [J mol^{-2}]**
923 K	0.336	-2.42E+05
973 K	-1.130	-9.88E+04
1023 K	-1.792	-7.68E+04

Table 5.2 The fitting parameters providing the best fit to the measurements ($La_3Ni_2O_{7-\delta}$, and $La_4Ni_3O_{10-\delta}$)

$La_3Ni_2O_{7-\delta}$	**log *K****	***a* [J mol^{-2}]**
923 K	1.308	-8.53E+05
973 K	1.662	-4.27E+05
1023 K	1.959	-2.17E+05

$La_4Ni_3O_{10-\delta}$	**log *K****	***a* [J mol^{-2}]**
923 K	0.049	-4.13E+05
973 K	0.412	-3.15E+05
1023 K	1.112	-1.89E+05

The equilibrium constant *K* increases exponentially with temperature, implying that the formation of oxygen interstitials is highly affected by temperature, as also shown in the isotherms. This is further confirmed by the observation that the slope of δ versus $p(O_2)$ at higher temperatures is steeper than that at lower temperatures, reflecting the relative ease of interstitial oxygen formation at high temperatures. Since the value of *-a* for $La_2NiO_{4+\delta}$-YSZ decreases with increasing temperature, the degree of interactions between the defects and the lattice ions diminishes at higher temperatures.

5.3.3.2 Oxygen deficient $La_3Ni_2O_{7-\delta}$ and $La_4Ni_3O_{10-\delta}$

Since oxygen vacancies ($V_o^{\bullet\bullet}$) and electron holes are the dominant defects in these crystals, the interactions between the crystal and the surrounding oxygen molecules can be described as follows.

$$\frac{1}{2}O_2 + V_o^{\bullet\bullet} \overset{K}{\leftrightarrow} O_o^{x} + 2h^{\bullet} \qquad (10a)$$

where the electron holes can be emitted from the lattice ions (most likely Ni ions) as follows,

$$Ni_{Ni}{}^{X} \leftrightarrow Ni_{Ni}{}' + h^{\bullet} \qquad (10b)$$

The combination of reactions (10a) and (10b) are the dominant defect reaction in these materials. Thus, charge neutrality requires that the effective negative charge on the lattice ions be balanced by the positive charges of electron holes and oxygen vacancies, as described below.

$$[Ni_{Ni}{}'] = [h^{\bullet}] + 2[V_o{}^{\bullet\bullet}] \quad \text{or} \quad [h^{\bullet}] = [Ni_{Ni}{}'] - 2\delta \qquad \text{Reaction (11)}$$

Here, the concentration of the charged lattice ions changes with non-stoichiometry as well. Since the electronic conductivity (σ_h) is much greater than the ionic conductivity (σ_v) for these materials, however, the total conductivity (σ) is dominated primarily by the transport of electron holes, i.e.,

$$\sigma \approx \sigma_h + \sigma_v \approx \sigma_h \approx [h^{\bullet}]\mu_h q \ \text{ or } \ [h^{\bullet}] \approx \frac{\sigma}{\mu_h q} \qquad \text{Reaction (12)}$$

where q is the charge of electron and μ_h is the drift mobility of electron holes.
In light of this approximation, the equilibrium constant for reaction (10a) can be approximated by

$$K = \frac{[O_o{}^{x}][h^{\bullet}]^2}{p(O_2)^{1/2}[V_o{}^{\bullet\bullet}]}\frac{\gamma_3{\gamma_2}^2}{\gamma_4} = \frac{[O_o{}^{x}](\frac{\sigma}{q\mu_h})^2}{p(O_2)^{1/2}[V_o{}^{\bullet\bullet}]}\frac{\gamma_3{\gamma_2}^2}{\gamma_4} \qquad \text{Reaction (13)}$$

where γ_3 and γ_4 denote the activity coefficients of O_o^x and $V_o^{\bullet\bullet}$, respectively.

The Gibbs free energy change, ΔG, of reaction (10a) can be expressed in terms of the equilibrium constant, K, as in Equation (14a) and (14b) for $La_3Ni_2O_{7-\delta}$ and $La_4Ni_3O_{10-\delta}$, respectively.

$$\Delta G = -RT\ln K = -RT\ln\frac{(7-\delta)(\frac{\sigma}{q\mu_h})^2}{p(O_2)^{1/2}\delta} - RT\ln(\frac{\gamma_3{\gamma_2}^2}{\gamma_4}) \quad \text{for } La_3Ni_2O_{7-\delta} \quad \text{Eqn. (14a)}$$

$$\Delta G = -RT\ln K = -RT\ln\frac{(10-\delta)(\frac{\sigma}{q\mu_h})^2}{p(O_2)^{1/2}\delta} - RT\ln(\frac{\gamma_3{\gamma_2}^2}{\gamma_4}) \quad \text{for } La_4Ni_3O_{10-\delta} \quad \text{Eqn. (14b)}$$

We define the second term in Equations (14a) and (14b) as the deviation from the standard free energy change of the ideal system, similar to the approximation made for the $La_2NiO_{4+\delta}$ case.[23]

$$\Delta G_{\text{ex}} = RT\ln\frac{\gamma_3{\gamma_2}^2}{\gamma_4} \equiv a\delta \quad \text{Eqn. (15)}$$

Solving Equations (13) – (15) simultaneously with $K^* \equiv K(q\mu_h)^2$, we have following equations.

$$K^* = \frac{(7-\delta)\sigma^2}{p(O_2)^{1/2}\delta}\frac{\gamma_3{\gamma_2}^2}{\gamma_4} \quad \text{for } La_3Ni_2O_{7-\delta} \quad \text{Eqn. (16a)}$$

$$K^* = \frac{(10-\delta)\sigma^2}{p(O_2)^{1/2}\delta}\frac{\gamma_3{\gamma_2}^2}{\gamma_4} \quad \text{for } La_4Ni_3O_{10-\delta} \quad \text{Eqn. (16b)}$$

which can be rewritten as,

$$p(O_2) = \frac{(7-\delta)^2\sigma^4}{{K^*}^2\delta^2}\left\{\exp(\frac{a\delta}{RT})\right\}^2 \quad \text{for } La_3Ni_2O_{7-\delta} \quad \text{Eqn. (17a)}$$

$$p(O_2) = \frac{(10-\delta)^2\sigma^4}{{K^*}^2\delta^2}\left\{\exp(\frac{a\delta}{RT})\right\}^2 \quad \text{for } La_4Ni_3O_{10-\delta} \quad \text{Eqn. (17b)}$$

The oxygen non-stoichiometry data (δ values) and the electrical conductivity data (σ values) at different partial pressure of oxygen collected for the two composite cathodes ($La_3Ni_2O_{7-\delta}$-YSZ and $La_4Ni_3O_{10-\delta}$-YSZ) were curve fitted to the models again. The theoretical curves calculated for using Equations (17a) and (17b) are presented as solid lines in Figure 4(b) and 4(c), respectively, with the fitted K^* and a values listed in Table 2. The theoretical curves again show quite good agreement with the experimental data before decomposition. Oxygen vacancy formation becomes more difficult compared to the ideal system when a is negative.[23,24]

5.3.4 Electrical conductivity

Shown in Fig. 5.8 are electrical conductivities for the $La_{n+1}Ni_nO_{3n+1}$-YSZ composites (n = 1, 2, and 3). At a given temperature, electrical conductivity increased with the value of n, due possibly to the increased number of Ni-O-Ni interactions, which are responsible for the electronic conduction pathways in the perovskite layers. However, the electrical conductivity showed a different trend on temperature.

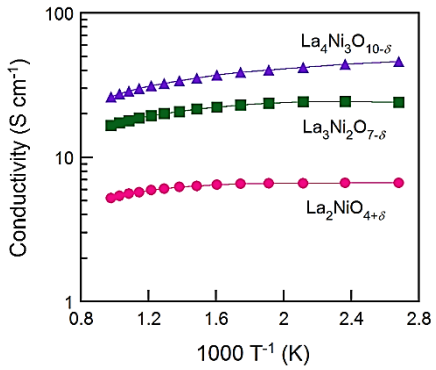

Figure 5.8 The electrical conductivity of the $La_{n+1}Ni_nO_{3n+1}$ (n = 1, 2, and 3)-YSZ composites at various temperature from 1023 K to 373 K in air, (●) $La_2NiO_{4+\delta}$, (■) $La_3Ni_2O_{7-\delta}$, and (▲) $La_4Ni_3O_{10-\delta}$.

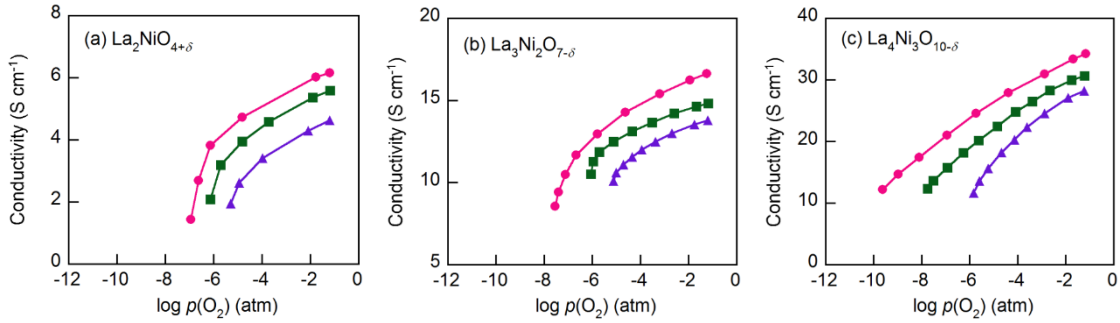

Figure 5.9 The electrical conductivities of the $La_{n+1}Ni_nO_{3n+1}$ (n = 1, 2, and 3)-YSZ composites, (a) $La_2NiO_{4+\delta}$, (b) $La_3Ni_2O_{7-\delta}$, and (c) $La_4Ni_3O_{10-\delta}$ at (●) 923 K, (■) 973 K, and (▲) 1023 K in various $p(O_2)$(atm).

The electrical conductivities of the $La_2NiO_{4+\delta}$-YSZ (n = 1) and $La_3Ni_2O_{7-\delta}$-YSZ (n = 2) composites show little dependence on temperature below ~573 K and then decreased slightly with increasing temperature (573<T(K)<1023). On the contrary, the electrical conductivity of the $La_4Ni_3O_{10-\delta}$-YSZ (n = 3) composite decreased monotonically with temperature, showing metallic behavior over the entire temperature range. The electrical conductivities for $La_{n+1}Ni_nO_{3n+1}$(42 wt%)-YSZ composites (n = 1, 2, and 3) calcined at 1023 K as a function of $p(O_2)$ at various temperatures (923<T(K)<1023) are presented

in Fig. 5.9. The electrical conductivities increased with $p(O_2)$ in all cases over the entire temperature range studied, indicating that this material is a *p*-type electronic conductor under the testing conditions. Further, the electrical conductivities measured at a higher temperature changed more rapidly with $p(O_2)$, suggesting that the electrical properties are more sensitive to oxygen non-stoichiometry at higher temperatures.

For $La_2NiO_{4+\delta}$, the electrical conductivities increased with $p(O_2)$ due mainly to increased concentration of mobile interstitial oxygen in the perovskite layers. Since the predominant defects in $La_2NiO_{4+\delta}$ are interstitial oxygen and electronic holes, an increase in the concentration of oxygen interstitial results in an increase in the concentration of electronic holes, which leads to increased electronic conductivity of the material.[17,18]

For $La_3Ni_2O_{7-\delta}$ and $La_4Ni_3O_{10-\delta}$, in contrast, an increase in oxygen partial pressure would lead to a decrease in concentration of oxygen vacancies and an increase in the concentration of electronic holes, which in turn increase the *p*-type electrical conductivity.

5.4. Conclusion

$La_{n+1}Ni_nO_{3n+1}$ (n = 1, 2, and 3) were infiltrated into scaffolds of YSZ to form composite cathodes for IT-SOFCs. The redox properties of $La_{n+1}Ni_nO_{3n+1}$ (n = 1, 2, and 3) infiltrated in YSZ were investigated using coulometric titration. $La_4Ni_3O_{10-\delta}$ appears to be more suited as cathode materials than $La_2NiO_{4+\delta}$ and $La_3Ni_2O_{7-\delta}$ because it has higher oxidation enthalpies and hence better stability in a lower $p(O_2)$ under the same testing conditions, Partial molar entropies can provide insight into the variation of the number of sites available for oxygen interstitial or vacancy formation reactions during the oxidation/reduction process. A defect model is proposed and it fits well the experimental data on non-stoichiometric variation of oxygen over a wide range of $p(O_2)$. All samples show increased electrical conductivity with increasing n at a given temperature. Therefore, the $La_4Ni_3O_{10-\delta}$-YSZ composites are considered the most favorable candidate cathode material for IT-SOFC applications.

References

1 Jacobson, A.J.; Materials for solid oxide fuel cells, *Chem. Mater.*, **2010**, *22*, 660-674.

2 Amow, G.; Skinner, S. J.; Recent developments in Ruddlesden-Popper nickelate systems for solid oxide fuel cell cathode, *J. Solid State Electrochem.*, 2006, **10**, 538-546.

3 Zhang, Z.; Greenblatt, M.; Goodenough, J. B.; Synthesis, structure, and properties of the layered perovskite $La_3Ni_2O_{7-\delta}$, *J. Solid State Chem.*, 1994, **108**, 402-409.

4 Zhang, Z.; Greenblatt, M.; Synthesis, structure, and properties of $Ln_4Ni_3O_{10-\delta}$ (Ln = La, Pr, and Nd), *J. Solid State Chem.*, 1995, **117**, 236-246.

5 Lee, K. T.; Manthiram, A.; $LaSr_3Fe_{3-y}Co_yO_{10-\delta}$ ($0 \leq y \leq 1.5$) Intergrowth Oxide Cathodes for Intermediate Temperature Solid Oxide Fuel Cells, *Chem. Mater.*, 2006, **18**, 1621-1626.

6 Amow, G.; Davidson, I. J.; Skinner, S. J.; A comparative study of the Ruddlesden-Popper series, $La_{n+1}Ni_nO_{3n+1}$ (n = 1, 2, and 3), for solid-oxide fuel-cell cathode applications, *Solid State Ionics*, **2006**, *177*, 1205-1210.

7 Skinner, S.J.; Kilner, J.A.; Oxygen diffusion and surface exchange in $La_{2-x}Sr_xNiO_{4+\delta}$, *Solid State Ionics*, **2000**, *135*, 709-712.

8 Yamada, A.; Suzuki, Y.; Saka, K.; Uehara, M.; Mori, D.; Kanno, R.; Kiguchi, T.; Mauvy, F.; Grenier, J.-C.; Ruddlesden-Popper-type epitaxial film as oxygen electrode for solid oxide fuel cells, *Adv. Mater.*, **2008**, *20*, 4124-4128.

9 Bannikov, D.O.; Safronov, A.P.; Cherepanov, V.A.; Thermochemical characteristics of $La_{n+1}Ni_nO_{3n+1}$ oxides, *Thermochim. Acta*, **2006**, *451*, 22-26.

10 Gao, Z.; Mao, Z. Q.; Wang, C.; Liu, Z. X.; Preparation and characterization of $La_{1-x}Sr_xNi_yFe_{1-y}O_{3-\delta}$ cathodes for low-temperature solid oxide fuel cells, *Int. J. Hydrogen Energy*, 2010, **35**, 12905-12910.

11 Kharton, V. V.; Viskup, A. P.; Naumovich, E. N.; Marques, F. M. B.; Oxygen ion transport in La_2NiO_4-based ceramics, *J. Mater. Chem.*, 1999, **9**, 2623-2629.

12 Tsipis, E. V.; Patrakeev, M. V.; Waerenborgh, J. C.; Pivak, Y. V.; Markov, A. A.; Gaczynski, P.; Naumovich. E. N.; Kharton, V. V.; Oxygen non-stoichiometry of $Ln_4Ni_{2.7}Fe_{0.3}O_{10-\delta}$ (Ln = La, Pr) *J. Solid State Chem.*, **2007**, *180*, 1902-1910.

13 Andersson, M.; Yuan, J. L.; Sunden, B.; Review on modeling development for multiscale chemical reactions coupled transport phenomena in solid oxide fuel cells, *Applied Energy*, **2010**, *87*, 1461-1476.

14 Yoo, S.; Shin, J.; Kim, G.; Thermodynamic and electrical characteristics of $NdBaCo_2O_{5+\delta}$ at varous oxidation and reduction states, *J. Mater. Chem.* **2011**, *21*, 439-443.

15 Yoo, S.; Shin, J.; Kim, G.; Thermodynamic and Electrical Properties of Layered Perovskite

$NdBaCo_{2-x}Fe_xO_{5+\delta}$-YSZ ($x$ = 0, 1) Composites for Intermediate Temperature SOFC Cathodes; *J. Electrochem. Soc*., **2011**, *158*, B632-B638.

16 Nakamura, T.; Yashiro, K.; Sato, K.; Mizusaki, J.; Oxygen nonstoichiometry and defect equilibrium in $La_{2-x}Sr_xNiO_{4+\delta}$, *Solid State Ionics*, **2009**, *180*, 368-376.

17 Tsipis, E. V.; Naumovich, E. N.; Patrakeev, M. V.; Waerenborgh, J. C.; Pivak, Y. V.; Gaczynski, P.; Kharton, V. V.; Oxygen non-stoichiometry and defect thermodynamics in $La_2Ni_{0.9}Fe_{0.1}O_{4+\delta}$, *J. Phys. Chem. Solids*, 2007, **68**, 1443-1455.

18 Sengodan, S.; Yeo, H. J.; Shin, J. Y., Kim, G.; Assessment of perovskite-type $La_{0.8}Sr_{0.2}Sc_xMn_{1-x}O_{3-\delta}$ oxides as anodes for intermediate-temperature solid oxide fuel cells using hydrocarbon fuels, *J. Power Sources*, **2011**, *196*, 3083-3088.

19 Li, Z.; Haugsrud, R.; Smith, J. B.; Norby, T.; Transport properties and defect analysis of $La_{1.9}Sr_{0.1}NiO_{4+\delta}$, *Solid State Ionics*, **2009**, *180*, 1433-1441.

20 Onuma, S.; Yashiro, K.; Miyoshi, S.; Kaimai, A.; Matsumoto, H.; Nigara, Y.; Kawada, T.; Mizusaki, J.; Kawamura, K.; Sakai, N.; Yokokawa, H.; Oxygen nonstoichiometry of the perovskite-type oxide $La_{1-x}Ca_xCrO_{3-\delta}$ (x = 0.1, 0.2, 0.3), *Solid State Ionics*, **2004**, *174*, 287-293.

21 Oishi, M.; Yashiro, K.; Hong, J. O.; Nigara, Y.; Kawada, T.; Mizusaki, J.; Oxygen nonstoichiometry of B-site doped $LaCrO_3$, *Solid State Ionics*, **2007**, *178*, 307-312.

22 Carvalho, M. D.; Wattiaux, A.; Ferreira, L. P.; Bassat, J. M.; Moessbauer investigation of 57Fe doped $La_4Ni_3O_{10\pm y}$ phases, *J. Solid State Chem.*, **2009**, *182*, 60-64.

23 Schroeder, M.; Dragan, M.-A.; J. Mater. Sci., Oxygen transport in $La_{2-x}Sr_xNiO_{4+\delta}$: membrane permeation and defect chemical modeling, *J. Mater. Sci.*, **2007**, *42*, 1972-1983.

Chapter 6. Comparative characterization of thermodynamic, electrical, and electrochemical properties of $Sm_{0.5}Sr_{0.5}Co_{1-x}Nb_xO_{3-\delta}$ (x = 0, 0.05, and 0.1) as cathode materials in intermediate temperature solid oxide fuel cells

6.1 Introduction

Solid oxide fuel cells (SOFCs) have been studied as a new power generation device on the strengths of their high conversion efficiency, low emissions, and excellent fuel flexibility. The requirement for high operating temperature ranging from 800 to 1000 °C, however, raises crucial issues such as high material costs and high rates of formation of electrical and chemical insulating phases during the cell fabrication and operation. The focus of recent research on SOFC technology has thus shifted towards intermediate temperature operation ranging from 500 to 700 °C.[1-3] The reduction of operating temperature, however, leads to a significant decrease in cathode activity. Therefore, an appropriate cathode material for IT-SOFCs should have high electrical conductivities and high catalytic activity for the oxygen reduction reaction as well as a thermal expansion coefficient that is compatible with the electrolyte.[4-6]

In this regard, mixed ionic and electronic conductors (MIECs) containing Mn, Fe, Co, and/or Ni with the capability to conduct oxygen ions and electrons simultaneously are strong candidates as IT-SOFC cathodes.[7-12] Among the various MIEC oxides, cobalt containing perovskite oxides such as (La,Sr)CoO_3 and (Ba,Sr)CoO_3 have attracted strong interest due to their high electrocatalytic activity for the oxygen reduction reaction.[13-15] The high catalytic activity of LSC can be explained by its high ionic conductivity with lower overpotential and high oxygen vacancy concentration, which facilitates rapid migration of oxygen species through the bulk as well as the surface of the electrode material. In addition, recent reports investigating Co-based perovskites, such as $Sm_{0.5}Sr_{0.5}CoO_{3-\delta}$ (SSC), have also garnered notable attention. Fukunaga *et al.* measured the reaction of a dense SSC cathode and found that the surface exchange constants are one order of magnitude larger than the corresponding values for $La_{0.6}Sr_{0.4}CoO_{3-\delta}$.[4,14-17]

Co-based perovskites, on the other hand, show very large thermal expansion coefficients (TECs), which causes mismatch between the cathode and electrolyte. This mismatch degrades the long-term stability and durability for thermal cycling in SOFC systems.[18-22] Nagai *et al.* demonstrated that the stability of the perovskite structure is enhanced by substituting B-sites with cations having a higher valence, and Nb is the most effective dopant for improving the chemical stability of Co-based perovskite oxides.[23,24] It has been reported that the introduction of Nb in the B-sites of cobalt-based perovskites can improve the electrochemical performance and chemical stability for SOFC application, with 10% Nb doping on $BaCo_{1-x}Fe_xO_{3-\delta}$.[25]

Based on these results, Nb doped SSC is regarded as a suitable cathode material that can provide high

cell performance and stability. The aim of this study is to assess the behavior of Nb doped SSC through characterization of the redox properties and electrochemical performances in terms of its application as a cathode for IT-SOFCs.

6.2. Experimental

$Sm_{0.5}Sr_{0.5}Co_{1-x}Nb_xO_{3-\delta}$ (SSCNb*x*) oxides were synthesized using the Pechini process to form submicron powder particles. Metal nitrates were employed both as metal precursors and oxidizing agents. Citric acid and niobium oxalate hydrate (Alfa aesar, $C_{10}H_5NbO_2 \cdot xH_2O$) were added to a hydrogen peroxide (H_2O_2) solution under heating (~50 ^oC) to increase the solubility of the Nb-complex. Stoichiometric amounts of $Sm(NO_3)_3 \cdot 6H_2O$ (Aldrich, 99.9%, metal basis), $Sr(NO_3)_2$ (Aldrich, 99+%), and $Co(NO_3)_2 \cdot 6H_2O$ (Aldrich, 98+%) were added into a beaker containing a suitable amount of concentrated nitric acid solution under continuous heating and stirring with the Nb precursor. An adequate amount of ethylene glycol was added into the beaker after the mixture was dissolved. After a viscous resin was formed, the mixture was heated to roughly 300 ^oC. The resultant powder was pre-calcined at 700 ^oC for 4 h, and ball-milled in acetone for 24 h. The powder was pressed into pellets and sintered at 1150-1200 ^oC for 4 h in air. For the measurement of cell performances of SSCNb*x* cathodes, slurries consisting of powders, GDC, and an organic binder at a weight ratio of 6 : 4 : 12 were used.

The structure and the morphology of the SSCNb*x* were characterized by X-ray diffraction (XRD) and scanning electron microscopy (SEM). X-Ray powder diffraction measurements (Rigaku diffractometer, Cu Ka radiation) were performed to confirm the structure with a scan rate of 0.6 ^{o} min^{-1}.

Symmetrical electrochemical cells with a configuration of electrode/GDC/electrode were applied for the impedance studies. $Ce_{0.9}Gd_{0.1}O_{1.95}$ (GDC) was used for the electrolyte to avoid interfacial reactions between the electrolyte and the cathode, because the LSGM electrolyte and YSZ electrolyte may react with the Sr-doped lanthanide cobaltites.[26] The GDC powder was pressed into pellets, and sintered at 1350 ^oC for 4 h in air to obtain a dense electrolyte substrate. The cathode slurry was painted onto both surfaces of the dense GDC electrolyte symmetrically and subsequently sintered at 950 ^oC for 4 h under an air atmosphere.

Electrochemical performances of the SSCNb*x* cathode were evaluated with Ni-GDC anode-supported single cells. To measure cell performance, the SSCNb*x* powders and GDC were mixed at a weight ratio of 6 : 4 and ball-milled for 12 h. The Ni-GDC cermet anode, thereafter, was fabricated from a mixture of nickel oxide, GDC prepared by GNP, and starch at a weight ratio of 6 : 4 : 1.5. This mixture was ball-milled in ethanol for 24 h. The GDC powder electrolyte was pressed over the pelletized Ni-GDC cermet anode. The Ni-GDC/GDC anode-electrolyte layer was sintered at 1350 ^oC for 5 h. For the top layer cathode, the SSCNb slurries were painted on the GDC electrolyte. The cells, with an active

electrode area of 0.36 cm^2, were finally sintered at 950 °C for 4 h under an air atmosphere. Ag wires were attached to both the anode and cathode of a single cell using Ag paste (SPI Supplies, 05063-AB) as a current collector. An alumina tube was employed to fix the single cell using a ceramic adhesive (Aremco, Ceramabond 553). H_2 containing 3 % H_2O was applied through a water bubbler with a flow rate of 20 mL min^{-1}, while air was applied as an oxidant and supplied to the cathode by ambient air flow during the single cell test. A BioLogic Potentiostat was used to measure impedance spectra and *I-V* curves. Impedance spectra were recorded under OCV in a frequency range of 1 mHz to 500 kHz with AC perturbation of 14 mA at 700 °C. I-V polarization curves were measured between 500 to 650 °C.

Coulometric-titration was used to evaluate the exact redox state of a composite as a function of $p(O_2)$. The detailed procedure has been described elsewhere.[27] The oxide-sample was placed in a sealed container at the temperature of interest and equilibrated sufficiently by passing a mixture of gases (5% O_2 in Ar) over it. The yttria-stabilized zirconia (YSZ) tube (McDanel Advanced Ceramic Technologies, Z15410630) was used both to electrochemically pump oxygen out of the system and to sense the equilibrium $p(O_2)$ inside the tube. The criterion we used for establishing equilibrium in coulometric titration was that the potential of the oxygen sensor changed by less than 1 mV h^{-1}. The electrical conductivity of the composite slabs was measured via the 4-probe method with a BioLogic Potentiostat.

6.3 Results

Figure 6.1(a) presents typical XRD patterns of SSC fired at 1150 °C and SSCNb*x* (*x* = 0.05, 0.1, 0.15, and 0.2) fired at 1200 °C. The patterns suggest that the SSCNb*x* samples have a single-phase perovskite structure without any detectable impurity phases up to *x* = 0.1 and the $Sr(Co_{0.5}Nb_{0.5})O_3$ secondary phase (JCPDS 00-052-0666) started to form with Nb content above *x* = 0.1. This indicates that SSC can form a solid-solution with Nb content of $x \leq 0.1$.

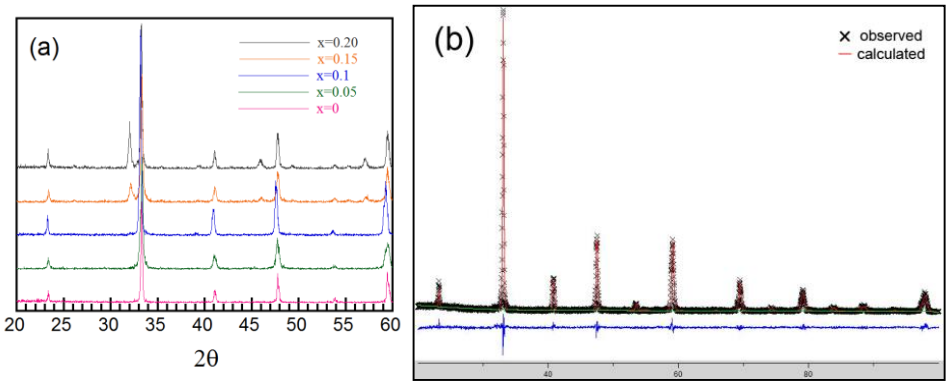

Figure 6.1 (a) XRD pattern of $Sm_{0.5}Sr_{0.5}Co_{1-x}Nb_xO_{3-\delta}$ after sintered at 1150-1200 °C, and (b) Rietveld refinement of $Sm_{0.5}Sr_{0.5}Co_{1-x}Nb_xO_{3-\delta}$ (*x* = 0.1) data from room temperature.

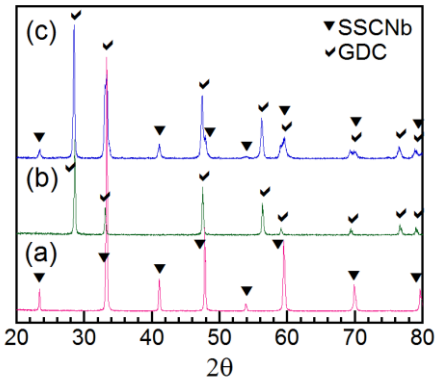

Figure 6.2 XRD patterns for (a) $Sm_{0.5}Sr_{0.5}Co_{0.9}Nb_{0.1}O_{3-\delta}$ powder, (b) GDC electrolyte, (c) $Sm_{0.5}Sr_{0.5}Co_{0.9}Nb_{0.1}O_{3-\delta}$-GDC composite after sintered at 950 °C for 4 h.

The XRD powder pattern of the SSCNb*x* cathode is analyzed by Rietveld refinement to demonstrate its crystal structure. The SSCNb*x* (*x* = 0.1) cathode could be indexed to an orthorhombic structure (space group: *Pbnm*), as illustrated in Fig. 6.1(b). As summarized in Table 6.1, the unit cell parameters increase with increasing Nb content, leading to an increase of unit cell volume. While the valence states of Co ions mostly are +3 or +4, Nb ions exist as a fixed valence state of +5 in SSCNb*x* oxides. If Nb^{5+} ions are substituted for Co^{3+} or Co^{4+} in B sites, a reduction of Co ions (from Co^{4+} to Co^{3+}) and/or a decrease of oxygen vacancy concentration would occur to maintain electroneutrality.[28,29] XRD patterns of SSCNb*x*-GDC powder composites calcined at 1000 °C are obtained in order to check their chemical stability. There appear to be no detectable reactions between SSCNb*x* and GDC and the patterns verify that the SSCNb*x* (*x* = 0.1) sample, for example, maintains a stable perovskite structure, as seen in Fig. 6.2.

Cross-sectional SEM images of a single cell and cathode are displayed in Fig. 3. The bottom side indicates the microstructure of the dense GDC electrolyte and the upper side shows the microstructure of the porous cathode made of SSCNb*x*-GDC (*x* = 0.1) after calcination at 950 °C, as presented in Fig. 6.3(a). The thickness of the cathode layer and the GDC electrolyte is approximately 15-20 μm, respectively. The microstructure of all SSCNb*x* (*x* = 0, 0.05, and 0.1) samples is similar, thus showing that the microstructures of the samples are apparently insensitive to Nb substitution.

The thermogravimetric analysis of SSCNb*x* cathodes with temperature in air is shown in Fig. 6.4. The room temperature oxygen content of SSCNb*x* (*x* = 0, 0.05, and 0.1) is set to be 3.0 through iodometric titration. The TGA curves show that significant weight loss occurs above 300 °C due to the loss of oxygen from the lattice. The weight loss of the sample over the entire temperature range decreases with increasing Nb content, possibly due to the stronger Nb-O bond compared to the Co-O bond, which would suppress the oxygen loss of the samples with high Nb content.

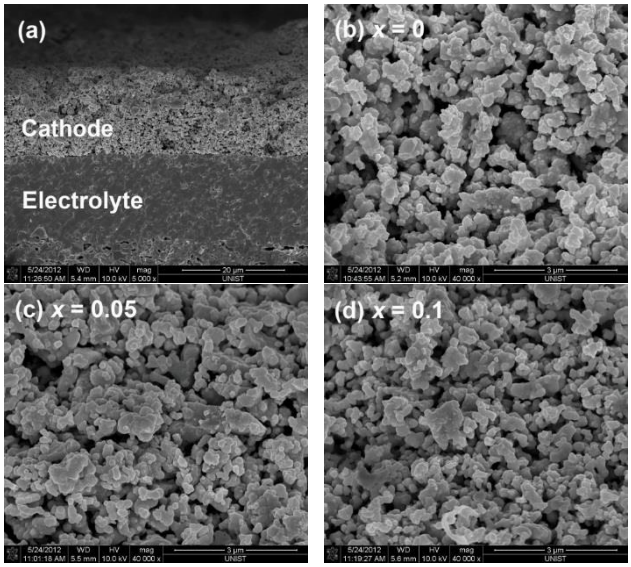

Figure 6.3 SEM images of (a) cross-sectional view of the single cell and $Sm_{0.5}Sr_{0.5}Co_{1-x}Nb_xO_{3-\delta}$ cathode with GDC electrolyte in a single cell configuration; (b) x = 0, (c) x = 0.05, and (d) x = 0.1.

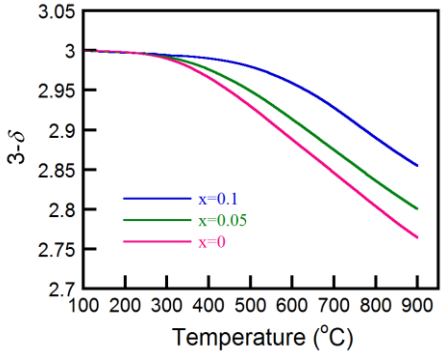

Figure 6.4 Thermogravimetric data of $Sm_{0.5}Sr_{0.5}Co_{1-x}Nb_xO_{3-\delta}$ (x = 0, 0.05, and 0.1) as a function of temperature.

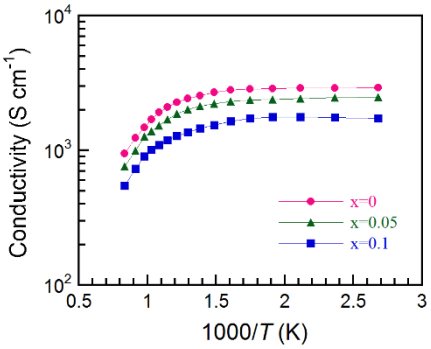

Figure 6.5 The electrical conductivity data for $Sm_{0.5}Sr_{0.5}Co_{1-x}Nb_xO_{3-\delta}$ (x = 0, 0.05, and 0.1) as a function of temperature in air.

The temperature dependence of the electrical conductivity of SSC in air is presented in Fig. 6.5. The electrical conductivity decreased monotonically with temperature, showing metallic behaviour over the entire temperature range. The faster decrease in conductivity at higher temperatures could be due to the formation of a significant amount of oxide ion vacancies.[1] The formation of oxide ion vacancies is accompanied by a reduction of Co^{4+} to Co^{3+}, which results in a decrease of the charge carrier concentration and Co-O covalency, respectively.[1,13] The electrical conductivity decreases with further increases of the Nb doping content. For the perovskite MIECs, simultaneous transport of oxygen ions and electronic conduction is achieved in these oxides. The transport of oxygen ions proceeds through hopping of oxygen vacancies, while transport of electrons is along the B^{n+}-O^{2-}-$B^{(n-1)+}$ network due to overlapping between B:3d and O:2p orbitals.[30] The increase of Nb doping leads to an increase of non-conducting Nb-O bonds, which obstructs electronic transport through O-Co-O bonds and, as a result, the electrical conductivity decreases.[29,30]

The impedance spectra for the symmetric cells (SSCNb*x*-GDC/GDC/SSCNb*x*-GDC) by AC impedance spectroscopy with various temperatures in air are shown in Fig. 6.6. In these spectra, the intercepts with the real axis at low frequency designate the total resistance of the cell and the value of high frequency is the ohmic resistance of the cell. The difference between the two values on the real axis indicates the sum of the cathode-electrolyte interface impedance and non-charge processes, including oxygen surface exchange, solid-state diffusion, and gas-phase diffusion, and is identified as the non-ohmic resistance of the cell.[11] The non-ohmic resistance values of SSCNb*x* (x = 0, 0.05, and 0.1) symmetrical cells are 0.061 Ω cm^2, 0.081 Ω cm^2, and 0.107 Ω cm^2, respectively at 650 °C. From these data, the apparent activation energies (E_a) of SSCNb*x* (x = 0, 0.05, and 0.1) are calculated to be 100.21 kJ mol^{-1}, 99.20 kJ mol^{-1}, and 96.35 kJ mol^{-1}, respectively. The increase of the ASR with an increase of Nb is possibly due to the decreased electrical conductivity and oxygen vacancy concentration.[11,31,32]

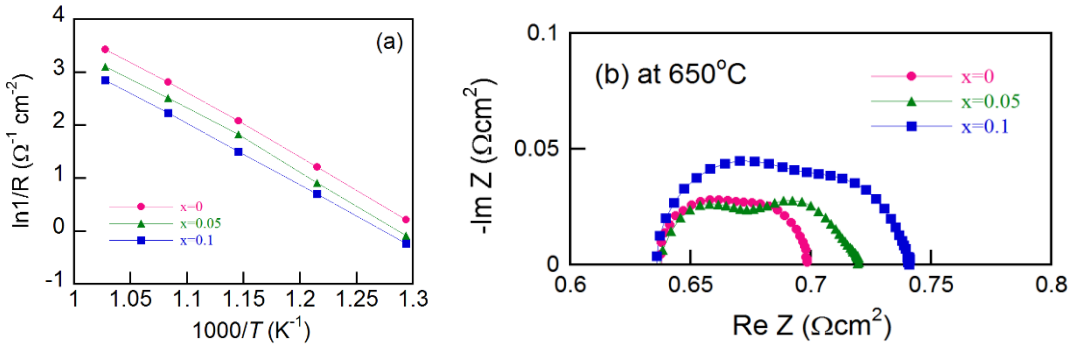

Figure 6.6 (a) Arrhenius plot of the area specific resistance for $Sm_{0.5}Sr_{0.5}Co_{1-x}Nb_xO_{3-\delta}$ (x = 0, 0.05, and 0.1) at various temperature.

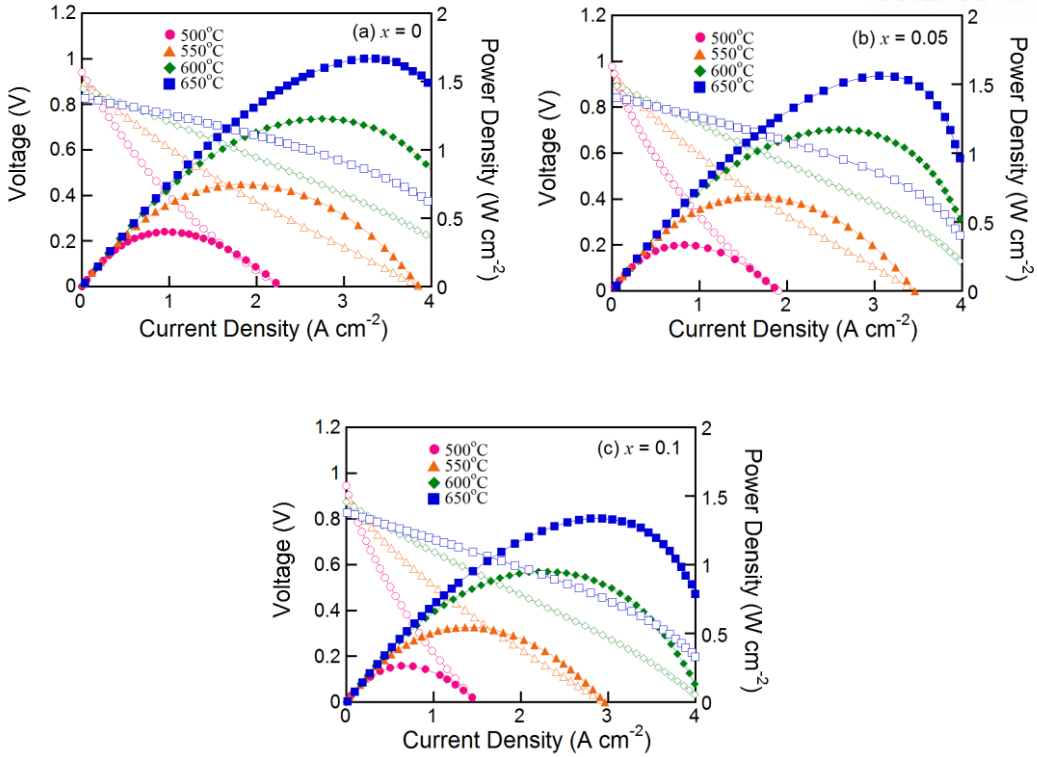

Figure 6.7 *I-V* curves and corresponding power density curves of single cell (Ni-GDC/GDC/$Sm_{0.5}Sr_{0.5}Co_{1-x}Nb_xO_{3-\delta}$ (x = 0, 0.05, and 0.1) in various temperature.

The performance of the SSCNb*x* cathodes in SOFCs is measured using the GDC electrolyte with humidified H_2 (3% H_2O) as a fuel and static ambient air as an oxidant in a temperature range of 500-650 °C. Figure 7 shows the *I-V* curves and the corresponding power density of the SSCNb*x* cathodes. The open-circuit voltages of the SSCNb*x* cells are typically 0.8 V at 700 °C and increase with decreasing operating temperature. The maximum power densities of the SSCNb*x* (x = 0, 0.05, and 0.1) cathode material are 1.229, 1.172, and 0.951 W cm^{-2}, at 600 °C, respectively.

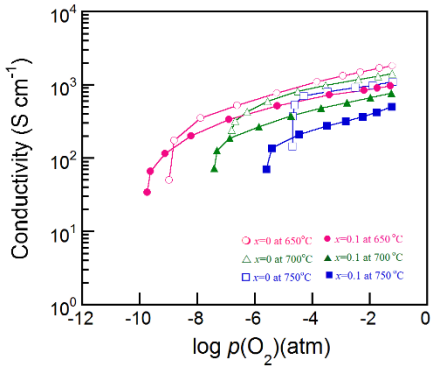

Figure 6.8 The electrical conductivities of the $Sm_{0.5}Sr_{0.5}Co_{1-x}Nb_xO_{3-\delta}$ (x = 0, 0.1) in various $p(O_2)$.

The electrical conductivities for SSCNb*x* measured at various $p(O_2)$ are shown in Fig. 6.8. The electrical conductivities increased with $p(O_2)$ in all cases over the entire temperature range, indicating that this material is a *p*-type electronic conductor under the experimental conditions. The predominant defects in SSCNb*x* are oxygen vacancies, $V_O^{\bullet\bullet}$ and $Co_{Co}^{\bullet}$. The pseudo-chemical reaction between the oxygen vacancies and the surrounding gas can be expressed as Eqn. (1).[17,29]

$$\frac{1}{2}O_2 + V_O^{\bullet\bullet} + 2Co_{Co}{}^{x} \rightleftarrows O_o{}^{x} + 2Co_{Co}^{\bullet} \qquad \text{Eqn. (1)}$$

Therefore, an increase in oxygen partial pressure would lead to a decrease in the concentration of oxygen vacancies and an increase in the concentration of electronic holes, which would in turn increase the *p*-type electrical conductivity.[11] The electrical conductivity is high enough at the IT-SOFC operating temperature (650-750 °C) down to a low oxygen partial pressure. The electrical conductivities of SSC dramatically decreased at a $p(O_2)$ of approximately 10^{-6} atm and the SSC appears to decompose thoroughly at a $p(O_2)$ of 10^{-7} atm. In contrast, the electrical conductivities of SSCNb*x* (x = 0.1) retain acceptable values down to a lower $p(O_2)$ of 10^{-7} atm. The higher redox stability of SSCNb*x* (x = 0.1) than SSC down to a lower $p(O_2)$ at the same temperature is attributed to the positive effect of Nb on the stability.[23,24,32]

Figure 6.9 shows the equilibrium oxygen nonstoichiometries for SSCNb*x* determined by coulometric titration as a function of $p(O_2)$ at temperatures of 650, 700, and 750 °C.[27,33] Under operation conditions, the interface of SOFCs between the electrolyte and the cathode experiences a lower $p(O_2)$, which may cause redox degradation of the cathode and affect the long term stability of the cathode performance.[34] The data show that the isotherms of SSCNb*x* at three different temperatures (650, 700, and 750 °C) have similar shapes, suggesting that the reduction mechanisms are quite similar. As the temperature decreases, the decomposition $p(O_2)$ becomes lower and the isotherms are extended to the left and the concentration of oxygen vacancies increases. It is shown that SSCNb*x* (x = 0.1) has a higher redox stability than SSC down to a lower $p(O_2)$ at the same temperature. For example, at 700 °C, the SSC sample starts to decay at a $p(O_2)$ of approximately 10^{-6} atm and appears to decompose thoroughly at a $p(O_2)$ of 10^{-7} atm; the SSCNb*x* samples meanwhile are stable to a lower $p(O_2)$, 10^{-7} atm. The higher redox stability of the SSCNb*x* oxides can be a key factor for attaining stable electrochemical properties of a cathode material for viable operation of IT-SOFCs. Therefore, Nb doped SSC oxides can be regarded as suitable cathode materials in terms of redox stability.[33]

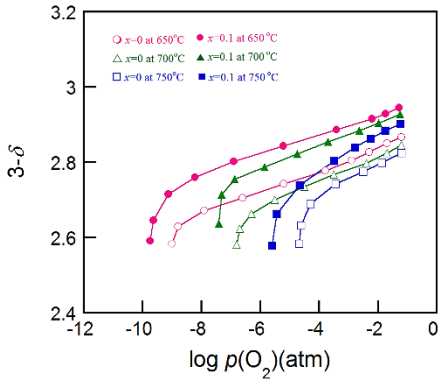

Figure 6.9 The isotherms of the $Sm_{0.5}Sr_{0.5}Co_{1-x}Nb_xO_{3-\delta}$ (x = 0, 0.1)

The partial molar enthalpy and entropy of oxidation can be calculated from the slopes of the isotherms. The Gibbs free energy, ΔG, is related to the equilibrium constant, K, and $p(O_2)$ as follows,

$$\Delta G = -RT\ln K = \frac{1}{2}RT\ln p(O_2) \qquad \text{Eqn. (2)}$$

At a constant δ, the partial molar enthalpy of oxidation at various temperatures is shown by the Gibbs-Helmholtz equation.[35]

$$\Delta H = \frac{\partial\left(\frac{\Delta G}{T}\right)}{\partial\left(\frac{1}{T}\right)} = \frac{R}{2}\left.\frac{\partial \ln[p(O_2)]}{\partial\left(1/T\right)}\right|_{\delta} \qquad \text{Eqn. (3)}$$

And the partial molar entropy can be obtained by using the Maxwell relation as follows.

$$-\Delta S = \frac{\partial \Delta G}{\partial T} = \left(\frac{R}{2}\right)\left.\left(\frac{\partial\, T\ln[p(O_2)]}{\partial T}\right)\right|_{\delta} \qquad \text{Eqn. (4)}$$

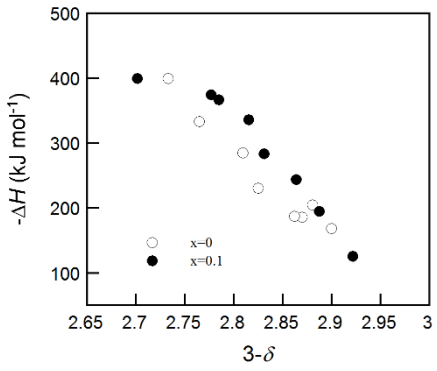

Figure 6.10 Partial molar enthalpy of oxidation (ΔH) at 700 ºC of $Sm_{0.5}Sr_{0.5}Co_{1-x}Nb_xO_{3-\delta}$ (x = 0, 0.1)

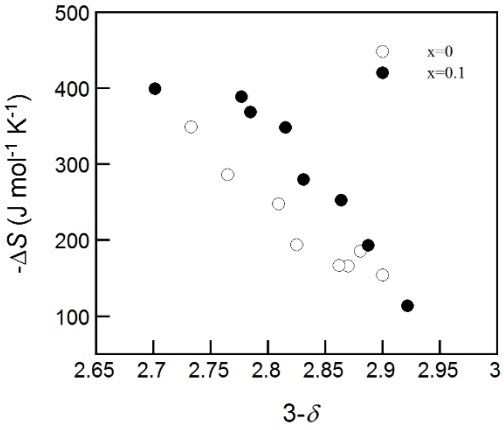

Figure 6.11 Partial molar entropy of oxidation (ΔS) at 700 ºC of $Sm_{0.5}Sr_{0.5}Co_{1-x}Nb_xO_{3-\delta}$ (x = 0, 0.1)

The partial enthalpies of oxidation for SSCNb*x* are calculated from Eqn. (3) and presented in Fig. 6.10. There are dramatic changes in the oxidation enthalpies according to the extent of reduction. In the case of Nb doped on a Co-based oxide, the energy states of Nb ions are located far above the Fermi level, and thus the electrons released by the formation of oxygen vacancies under a reducing atmosphere would results in little deterioration of the bonds between Nb and O ions. The resilient Nb-O bonding can thus stabilize the oxide. Furthermore, Nb doping raises the formation energy of oxygen vacancies in perovskites.[23]

The partial molar entropies of oxidation, calculated from the differences in the Gibbs free energies and the enthalpies, are shown in Fig. 6.11. It appears that the probability of oxygen vacancy formation rises as the concentration of oxygen vacancies increases.

6.4 Conclusion

$Sm_{0.5}Sr_{0.5}Co_{1-x}Nb_xO_{3-\delta}$ (SSCNb*x*) perovskite oxides have been investigated as a cathode material for IT-SOFCs. It is shown that Nb doping has a significant effect on the electrical conductivity, electrochemical performance, and redox stability of the SSCNb*x* oxides. SSCNb*x* (x = 0, 0.05, and 0.1) oxides show gradually decreasing electrical conductivity with increasing Nb doping at the same temperature. The impedance spectra for symmetric cells are measured by AC impedance spectroscopy at various temperatures in air. The non-ohmic resistance of SSCNb*x* (x = 0, 0.05, and 0.1) smmetrical cells is 0.061 Ωcm^2, 0.081 Ωcm^2, and 0.107 Ωcm^2, respectively, at 650 ºC. The increase of the ASR with an increase of Nb is possibly due to the decreased electrical conductivity and oxygen vacancy concentration. The electrochemical performances of SSCNb*x* are measured using an anode-supported cell based on a GDC electrolyte with humidified H_2 (3% H_2O). The maximum power densities of the single cell are 1.229, 1.172, and 0.951 W cm^{-2}, at 600 ºC, respectively, with a SSCNb*x* (x = 0, 0.05, and

0.1)-GDC composite cathode. The maximum power density of SSCNb*x* (x = 0.05, 0.1) is lower than that of SSC; however, SSCNb*x* (x = 0.1) is more stable than SSC considering the thermodynamic behaviour observed from the coulometric titration experiment. From these results, the Nb doped SSC oxide appears to be an acceptable IT-SOFC cathode material, considering its high power density and reasonable redox stability.

References

1 Lee, K.T.; Manthiram, A.; Comparison of $Ln_{0.6}Sr_{0.4}CoO_{3-\delta}$ (Ln = La, Pr, Nd, Sm, and Gd) as Cathode Materials for Intermediate Temperature Solid Oxide Fuel Cells, *J. Electrochem. Soc*., **2006**, *153*, A794-A798.

2 Zhou, W.; Jin, W.; Zhu, Z.; Shao, Z.; Structural, electrical and electrochemical characterizations of $SrNb_{0.1}Co_{0.9}O_{3-\delta}$ as a cathode of solid oxide fuel cells operating below 600 ºC, *Int. J. Hydrogen Energy*, **2010**, *35*, 1356-1366.

3 Jacobson, A.J.; Materials for solid oxide fuel cells, *Chem. Mater*., **2010**, *22*, 660-674.

4 Fukunaga, H.; Koyama, M.; Takahashi, N.; Wen, C.; Yamada, K.; Reaction model of dense $Sm_{0.5}Sr_{0.5}CoO_3$ as SOFC cathode, *Solid State Ionics*, **2000**, *132*, 279-285.

5 Zhou, W.; Ran, R.; Shao, Z.; Progress in understanding and development of $Ba_{0.5}Sr_{0.5}Co_{0.8}Fe_{0.2}O_{3-\delta}$-based cathodes for intermediate-temperature solid-oxide fuel cells: A review, J. Power Sources, **2009**, *192*, 231-246.

6 Yang, S.; He, T.; He, Q.; $Sm_{0.5}Sr_{0.5}CoO_3$ cathode material from glycne-nitrate process: Formation, characterization, and application in $LaGaO_3$-based solid oxide fuel cells, *J. Alloys Compd.*, **2008**, *450*, 400-404.

7 Tsipis, E.V.; Kharton, V.V.; Electrode materials and reaction mechanisms in solid oxide fuel cells: a brief review, *J. Solid State Electrochem.*, **2008**, *12*, 1367-1391.

8 Murray, E.P.; Sever, M.J.; Barnett, S.A.; Electrochemical performance of (La,Sr)(Co,Fe)O_3-(Ce,Gd)O_3 composite cathodes, *Solid State Ionics*, **2002**, *148*, 27-34.

9 Choi, S.; Shin, J.; Kim, G.; The electrochemical and thermodynamic characterization of $PrBaCo_{2-x}Fe_xO_{5+\delta}$ (x = 0, 0.5, 1) infiltrated into yttria-stabilized zircornia scaffold as cathodes for solid oxide fuel cells, *J. Power Sources*, **2012**, *201*, 10-17.

10 Acuña, L.M.; Peña-Martínez, J.; Marrero-López, D.; Fuentes, R.O.; Nuñez, P.; Lamas, D.G.; Electrochemical performance of nanostructured $La_{0.6}Sr_{0.4}CoO_{3-\delta}$ and $Sm_{0.5}Sr_{0.5}CoO_{3-\delta}$ cathodes for IT-SOFCs, *J. Power Sources*, **2011**, *196*, 9276-9283.

11 Adler, S.B.; Lane, J.A.; Steele, B.C.H.; Electrode Kinetics of Porous Mixed-Conducting Oxygen Electrodes, *J. Electrochem. Soc*., **1996**, *143*, 3554-3564.

12 Jiang, S.P.; A comparison of O_2 reduction reactions on porous (La,Sr)MnO_3 and (La,Sr)(Co,Fe)O_3 electrodes, *Solid State Ionics*, **2002**, *146*, 1-22.

13 Park, S.; Choi, S.; Shin, J.; Kim, G.; Electrochemical investigation of strontium doping effect on high performance $Pr_{1-x}Sr_xCoO_{3-\delta}$ (x = 0.1, 0.3, 0.5, and 0.7) cathode for intermediate-temperature solid oxide fuel cells, *J. Power Sources*, **2012**, *210*, 172-177.

14 Xia, C.; Rauch, W.; Chen, F.; Liu, M.; $Sm_{0.5}Sr_{0.5}CoO_3$ cathodes for low-temperature SOFCs, *Solid*

State Ionics **2002**, *149*, 11-19.

15 Hung, I.-M.; Fung, K.-Z.; Lin, C.-T.; Hon, M.-H.; The synthesis and characterization of the $Sm_{0.5}Sr_{0.5}Co_{1-x}Cu_xO_{3-\delta}$ cathode by the glycine-nitrate process, *J. Power Sources*, **2009**, *193*, 116-121.

16 Guo, Y.; Chen, D.; Shi, H.; Ran, R.; Shao, Z.; Effect of Sm3+ content on the properties and electrochemical performance of $Sm_xSr_{1-x}CoO_{3-\delta}$ ($0.2 \leq x \leq 0.8$) as an oxygen reduction electrodes on doped ceria electrolytes, *Electrochim. Acta*, **2011**, *56*, 2870-2876.

17 Dong, F.; Chen, D.; Ran, R.; Park, H.; Kwak, C.; Shao, Z.; A comparative study of $Sm_{0.5}Sr_{0.5}MO_{3-\delta}$ (M = Co and Mn) as oxygen reduction electrodes for solid oxide fuel cells, *Int. J. Hydrogen Energy*, **2012**, *37*, 4377-4387.

18 Equchi, K.; Ceramic materials containing rare earth oxides for solid oxide fuel cell, *J. Alloys and Compd*. **1997**, *250*, 486-491.

19 Lv, H.; Wu, Y.; Huang, B.; Zhao, B.; Hu, K.; Structure and electrochemical properties of $Sm_{0.5}Sr_{0.5}Co_{1-x}Fe_xO_{3-\delta}$ cathodes for solid oxide fuel cells, *Solid State Ionics*, **2006**, *177*, 901-906.

20 Lee, S.J.; Muralidharan, P.; Jo, S.H.; Kim, D.K.; Composite cathode for IT-SOFC: Sr-doped lanthanum cuprate and Gd-doped ceria, *Electrochem. Comm*., **2010**, *12*, 808-811.

21 Zhang, Y.; Xia, C.; A durability model for solid oxide fuel cell electrodes in thermal cycle processes, *J. Power Sources*, **2010**, *195*, 6611-6618.

22 Zhao, F.; Peng, R.; Xia, C.; A $La_{0.6}Sr_{0.4}CoO_{3-\delta}$-based electrode with high durability for intermediate temperature solid oxide fuel cells, *Mater. Res. Bull*., **2008**, *43*, 370-376.

23 Shen, P.J.; Liu, X.; Wang, H.H.; Ding, W.Z.; Niobium Doping Effects on Performance of $BaCo_{0.7}Fe_{0.3-x}Nb_xO_{3-\delta}$ Perovskite, *J. Phys. Chem. C*, **2010**, 114, 22338-22345.

24 Nagai, T.; Ito, W.; Sakon, T.; Relationship between cation substitution and stability of perovskite structure in $SrCoO_{3-\delta}$ based mixed conductors, *Solid State Ionics*, **2007**, *177*, 3433-3444.

25 Yang, Z.; Yang, C.; Jin, C.; Han, M.; Chen, F.; $Ba_{0.9}Co_{0.7}Fe_{0.2}Nb_{0.1}O_{3-\delta}$ as cathode material for intermediate temperature solid oxide fuel cells, *Electrochem. Comm*., **2011**, *13*, 882-885.

26 Dieterle, L.; Bach, D.; Schneider, R.; Störmer, H.; Gerthsen, D.; Guntow, U.; Ivers-Tiffée, E.; Weber, A.; Peters, C.; Yokokawa, H.; *J. Mater. Sci*., **2008**, *43*, 3135–3143.

27 Yoo, S.; Shin, J.; Kim, G.; Thermodynamic and electrical characteristics of $NdBaCo_2O_{5+\delta}$ at varous oxidation and reduction states, *J. Mater. Chem*. **2011**, *21*, 439-443.

28 Cheng, Y.; Zhao, H.; Teng, D.; Li, F.; Lu, X.; Ding, W.; Investigation of Ba fully occupied A-site $BaCo_{0.7}Fe_{0.3-x}Nb_xO_{3-\delta}$ perovskite stabilized by low concentration of Nb for oxygen permeation membrane, *J. Membrane. Sci*., **2008**, *322*, 484-490.

29 Wang, F.; Zhou, Q.; He, T.; Li, G.; Ding, H.; Novel $SrCo_{1-y}Nb_yO_{3-\delta}$ cathodes for intermediate-

temperature solid oxide fuel cells, *J. Power Sources*, **2010**, *195*, 3772-3778.

30 Deng, Z.Q.; Yang, W.S.; Liu, W.; Chen, C.S.; Relationship between transport properties and phase transformations in mixed-conducting oxides, *J. Solid State Chem.*, **2006**, *179*, 362-369.

31 Li, Q.; Zhao, H.; Huo, L.; Sun, L.; Cheng, X.; Grenier, J.-C.; Electrode properties of Sr doped La_2CuO_4 as new cathode material for intermediate-temperature SOFCs, *Electrochem. Comm.*, **2007**, *9*, 1508-1512.

32 Deng, Z.Q.; Smit, J.P.; Niu, H.J.; Evans, G.; Li, M.R.; Xu, Z.L.; Claridge, J.B.; Rosseinsky, M.J.; B Cation Ordered Double Perovskite $Ba_2CoMo_{0.5}Nb_{0.5}O_{6-\delta}$ As a Potential SOFC Cathode, *Chem. Mater.*, **2009**, *21*, 5154-5162.

33 Yoo, S.; Shin, J.Y.; Kim, G.; Thermodynamic and Electrical Properties of Layered Perovskite $NdBaCo_{2-x}Fe_xO_{5+\delta}$-YSZ ($x$ = 0, 1) Composites for Intermediate Temperature SOFC Cathodes, J. Electrochem. Soc., **2011**, *158*, B632-B638.

34 Bastidas, D.M.; Tao, S.; Irvine, J.T.S.; A symmetrical solid oxide fuel cell demonstrating redox stable perovskite electrodes, *J. Mater. Chem.*, **2006**, *16*, 1603-1605.

35 Nakamura, T.; Yashiro, K.; Sato, K.; Mizusaki, J.; Oxygen nonstoichiometry and defect equilibrium in $La_{2-x}Sr_xNiO_{4+\delta}$, *Solid State Ionics*, **2009**, *180*, 368-376.

Chapter 7. Structural, electrical and electrochemical characteristics of $La_{0.1}Sr_{0.9}Co_{1-x}Nb_xO_{3-\delta}$ as a cathode material for intermediate temperature solid oxide fuel cells

7.1 Introduction

One of the most promising energy conversion devices, solid oxide fuel cells has recently received a great deal of attention because of their high efficiency, low pollutant, and fuel flexibility, etc. The requirement for high operating temperature (800-1000 °C) of conventional SOFCs, however, leads to notable problems such as high costs and high rate of degradation due to the interactions between cell components during cell fabrication and/or operation. To overcome these problems, researchers have strived to lower the SOFC operating temperature toward an intermediate-temperature (IT) range (500-700 °C). One of the challenges for IT-SOFCs, however, is to develop cathode materials with sufficiently high electrocatalytic activity for oxygen reduction.[1-6]

A preferable cathode material for IT-SOFCs should have high electronic and oxide ion conductivities, and high catalytic activity for the oxygen reduction reaction. In this regard, mixed ionic and electronic conductors (MIECs) containing Mn, Fe, Co, and/or Ni with the capability to conduct oxygen ions and electrons simultaneously are strong candidates as IT-SOFC cathodes.[7-12] Among those various MIEC oxides, perovskite systems continue to dominate the research on SOFC cathodes, and there has been increasing interest in Co-containing systems in particular due to their high electronic and oxide ion conductivity.[8-11]

Among Co-containing perovskite materials, lanthanum-doped strontium cobaltites ($(La,Sr)CoO_{3-\delta}$) have been studied extensively due to the favorable electrical properties.[1,12] The high catalytic activity of LSC was meanwhile explained by its high ionic conductivity with lower overpotential and high oxygen vacancy concentration, which facilitates rapid migration of oxygen species through the bulk as well as the surface of the electrode material. The oxygen vacancies located in the lattice of a cathode material are an important factor to determine the oxygen reduction process as well as the electronic conduction. Oxygen vacancies are not only carriers for oxide ion transport through the cathode but also active sites for oxygen adsorption, dissociation, and diffusion. Both high oxygen vacancy concentration and high electronic conductivity would be beneficial for reducing the resistance of the oxygen reduction reaction (ORR).[1,13,14]

However, one of the problems with $(La,Sr)CoO_{3-\delta}$ perovskite cobaltites is the stability of competing hexagonal phases at high cobalt oxidation states (> +3). These hexagonal phases can influence degradation over time and impair their performance as SOFC cathodes.[12] Another problem is the ordering of oxygen vacancies that has been demonstrated to occur in $(La,Sr)CoO_{3-\delta}$ below 750 °C at $p(O_2)$ below 0.1 atm. These problems give rise to a significant decrease in electronic and ionic

conductivity, in addition to mechanical instability associated with lattice expansion.[12,15-17]

This incompatibility can cause structural instability of cathode materials in operating SOFCs and thus result in poor long-term thermal stability. Therefore, to enhance the structural stability of LSC-based perovskites, one strategy is to dope their B-sites via suitable cations. Nagai *et al.* demonstrated that the stability of the perovskite structure is enhanced by substituting B-sites with cations having a higher valence and Nb is the most effective dopant for improving the chemical stability of Co-based perovskite oxides.[18,19] It has been reported that the introduction of Nb in the B-sites of cobalt-based perovskites can improve the electrochemical performance and chemical stability for SOFC application, with 10% Nb doping on $BaCo_{1-x}Fe_xO_{3-\delta}$.[20,21]

The aim of this study is to present the structural-stabilization effect of Nb doping in the B-site of the perovskite $La_{0.1}Sr_{0.9}Co_{1-x}Nb_xO_{3-\delta}$ (LSCNb*x*), which shows considerably good structural stability and high electrochemical performance. The behavior of Nb doped LSC is illustrated through the structural, electrical, and electrochemical characterization in terms of its application as a cathode for IT-SOFCs.

7.2 Experimental

LSCNb*x* (x = 0, 0.1, 0.15, and 0.2) phases were synthesized through standard solid-state reaction techniques. La_2O_3 was dried overnight at 1000 °C before being used. Stoichiometric amounts of La_2O_3 (Waco, 99.99%), $SrCO_3$ (Aldrich, 99.9%), Co_2O_3 (Junsei, 99%), and Nb_2O_5 (Fluka, 99.9%) were thoroughly mixed with an agate mortar and pestle and pressed into pellets. The pellets in alumina boats were gradually heated to 1200 °C for 24 h with an intermediate regrinding. All the samples were cooled, reground, and repelletized during the intermediate heating. The samples were cooled at a rate of 5 °C h^{-1} to room temperature.

The X-ray powder diffraction data were collected on a Bruker D8-Advance diffractometer using Cu Kα radiation at room temperature with 40 kV and 40 mA. The 2θ range was 10–110° with a step size of 0.02°, and a step time of 1 s. High-temperature XRD studies were carried out in air ranging from 100 to 800 °C (Bruker D8 Advance, Cu Kα radiation) with measurements made every 100 °C. The diffraction patterns were analyzed using the Rietveld method with the GSAS program.[22] The structural refinement of the materials was carried out in the space group *Pm*-3*m* (No. 221) with a starting model based on the reported data of $La_{0.1}Sr_{0.9}CoO_3$.[23] A total of 25 parameters were used during the refinements. An asymmetry correction was applied to the low-angle reflections. The scale was initially refined, followed in subsequent iterations by the zero point error, unit-cell, peak shape, and overall isotropic displacement parameters. No crystallographic ordering between Co^{3+} and Nb^{5+} cations was observed. In the solid solutions of LSCNb*x* (x = 0.1, 0.15, and 0.2), the Co^{3+} and Nb^{5+} were statistically disordered over the transition metal sites.

Table 7.1 Summary of Crystallographic Data and Refinement Results for $La_{0.1}Sr_{0.9}Co_{1-x}Nb_xO_3$

x	0.0	0.1	0.15	0.2
formula	$La_{0.1}Sr_{0.9}CoO_3$	$La_{0.1}Sr_{0.9}Co_{0.9}Nb_{0.1}O_3$	$La_{0.1}Sr_{0.9}Co_{0.85}Nb_{0.15}O_3$	$La_{0.1}Sr_{0.9}Co_{0.8}Nb_{0.2}O_3$
space group	*Pm*-3*m* (No. 221)	*Pm*-3*m* (No. 221)	*Pm*-3*m* (No. 221)	*Pm*-3*m* (No. 221)
$a = b = c$ (Å)	3.842134(19)	3.85814(3)	3.86748(2)	3.87504(3)
V (Å^3)	56.7180(10)	57.4290(10)	57.8470(10)	58.188(2)
λ (Å)	1.5406	1.5406	1.5406	1.5406
R_p[a]	0.0292	0.0312	0.0290	0.0307
R_{wp}[b]	0.0368	0.0396	0.0368	0.0377

Table 7.2 Selected Bond Distances (Å) for $La_{0.1}Sr_{0.9}Co_{1-x}Nb_xO_3$

$La_{0.1}Sr_{0.9}CoO_3$		$La_{0.1}Sr_{0.9}Co_{0.9}Nb_{0.1}O_3$	
Co(1)–O(1) × 6	1.921070(10)	Co(1)/Nb(1)–O(1) × 6	1.92907(2)
Sr(1)/La(1)–O(1) × 12	2.716800(10)	Sr(1)/La(1)–O(1) × 12	2.72811(2)

$La_{0.1}Sr_{0.9}Co_{0.85}Nb_{0.15}O_3$		$La_{0.1}Sr_{0.9}Co_{0.8}Nb_{0.2}O_3$	
Co(1)/Nb(1)–O(1) × 6	1.933740(10)	Co(1)/Nb(1)–O(1) × 6	1.93752(2)
Sr(1)/La(1)–O(1) × 12	2.73472(2)	Sr(1)/La(1)–O(1) × 12	2.74007(2)

The resulting formulas are in good agreement with the reported stoichiometry. The results of the crystallographic data and selected bond distances (Å) for LSCNb*x* (x = 0.1, 0.15, and 0.2) solid solutions are summarized in Table 1 and 2, respectively.

The microstructures and morphologies of LSCNb*x* cathode samples were observed using a field emission scanning electron microscope (SEM) (Nova SEM). A thermogravimetric analysis (TGA) was carried out using a SDT-Q600 (TA instrument, USA). TGA experiments were performed from 100 °C to 900 °C with a heating/cooling rate of 2 °C min^{-1} in air. The room-temperature oxygen content values were determined by iodometric titration.

Symmetrical electrochemical cells with a configuration of electrode/GDC/electrode were applied for the impedance studies. $Ce_{0.9}Gd_{0.1}O_{1.95}$ (GDC) was used for the electrolyte to avoid interfacial

reactions between the electrolyte and the cathode, because the $LaGaO_3$ based electrolyte (LSGM) and yttria-stabilized zircornia electrolyte (YSZ) may react with the La-doped strontium cobaltites.[24] The GDC powder was pressed into pellets, and sintered at 1350 °C for 4 h in air to obtain a dense electrolyte substrate. The cathode slurry was painted onto both surfaces of the dense GDC electrolyte symmetrically and subsequently sintered at 950 °C for 4 h under an air atmosphere.

Electrochemical performance of the LSCNb*x* (*x* = 0.1, 0.15, and 0.2) cathode was evaluated with Ni-GDC anode-supported single cells. To measure cell performance, LSCNb*x* (*x* = 0.1, 0.15, and 0.2) powders and GDC were mixed at a weight ratio of 6 : 4 and ball-milled for 12 h. The Ni-GDC cermet anode, thereafter, was fabricated from a mixture of nickel oxide, GDC prepared by GNP, and starch at a weight ratio of 6 : 4 : 1.5. This mixture was ball-milled in ethanol for 24 h. The GDC powder electrolyte was pressed over the pelletized Ni-GDC cermet anode. The Ni-GDC/GDC anode-electrolyte layer was sintered at 1350 °C for 5 h. For the top layer cathode, LSCNb*x* (*x* = 0.1, 0.15, and 0.2) slurries were painted on the GDC electrolyte. The cells, with an active electrode area of 0.36 cm^2, were finally sintered at 950 °C for 4 h under an air atmosphere. Ag wires were attached to both the anode and cathode of a single cell using Ag paste (SPI Supplies, 05063-AB) as a current collector. An alumina tube was employed to fix the single cell using a ceramic adhesive (Aremco, Ceramabond 552). H_2 containing 3 % H_2O was applied through a water bubbler with a flow rate of 20 mL min^{-1}, while air was applied as an oxidant and supplied to the cathode by ambient air flow during the single cell test. A BioLogic Potentiostat was used to measure impedance spectra and *I-V* curves. Impedance spectra were recorded under OCV in a frequency range of 1 mHz to 500 kHz with AC perturbation of 14 mA at 700 °C. I-V polarization curves were measured between 500 to 650 °C.

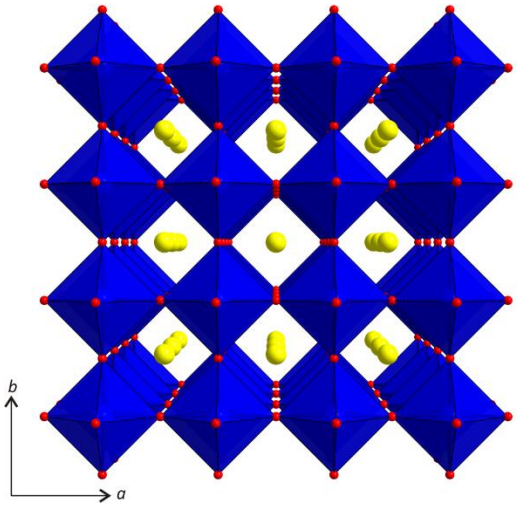

Figure 7.1 Polyhedral representation of $La_{0.1}Sr_{0.9}Co_{1-x}Nb_xO_3$ in the *ab*-plane (blue, Co(1) or Nb(1); yellow, Sr(1) or La(1); red, O).

7.3 Results

LSCNb*x* (*x* = 0, 0.1, 0.15, and 0.2) exhibits a perovskite structure crystallizing in a centrosymmetric cubic space group *Pm*-3*m* (No. 221) as shown in Fig. 7.1. The B-site is occupied by Co^{3+} or Nb^{5+} and the cations are bonded to six oxygen atoms in a regular octahedral environment with bond length ranging from 1.92107(10) to 1.93752(2) Å depending on *x*. In the A-site, Sr^{2+} or La^{3+} cations are present with A–O contact distances ranging from 2.71680(10) to 2.74007(2) Å. For comparison, lists of the selected bond distances for LSCNb*x* (*x* = 0, 0.1, 0.15, and 0.2) are given in Table 2. The bond distances are consistent with those previously reported.[2,25]

We were able to substitute up to 20 % of Nb^{5+} cations for Co^{3+} to form solid solutions, *i.e.*, LSCNb*x* (*x* = 0.1, 0.15, and 0.2). The powder X-ray diffraction data for solid solutions of $La_{0.1}Sr_{0.9}Co_{1-x}Nb_xO_3$ are shown in Fig. 7.2 with the refined parameters given in Table 7.1. As can be seen clearly from the powder X-ray diffraction patterns in Fig. 7.2, the peak positions shift to the left-hand side and the peak widths broaden as the amount of doped Nb^{5+} increases. As expected, the cell volume increases with increasing Nb^{5+} on the Co^{3+} site, which is attributed to the larger size of Nb^{5+} compared with the relatively smaller size of Co^{3+}. While the ionic radius of six-coordinate Nb^{5+} is known to be 0.64 Å, that for six-coordinate Co^{3+} is known to be smaller, 0.61 Å.[26] Thus, the unit-cell parameters and the cell volumes increase with increasing Nb^{5+} on the Co^{3+} site (see Fig. 7.3a). The peak broadening may be attributable to the increased statistical disordering between Co^{3+} and Nb^{5+} cations. We did not observe any ordering between Nb^{5+} and Co^{3+} in the LSCNb*x* phase. The experimental, calculated, and difference diffraction plots for LSCNb*x* (*x* = 0.1) are also shown in Fig. 7.3b.

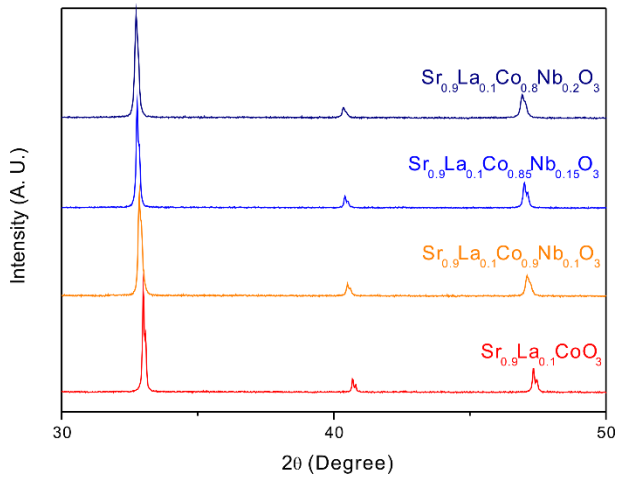

Figure 7.2 Powder X-ray diffraction data for $La_{0.1}Sr_{0.9}Co_{1-x}Nb_xO_3$ (*x* = 0, 0.1, 0.15, and 0.2). Note that the peak positions shift toward the left-hand side as *x* increases.

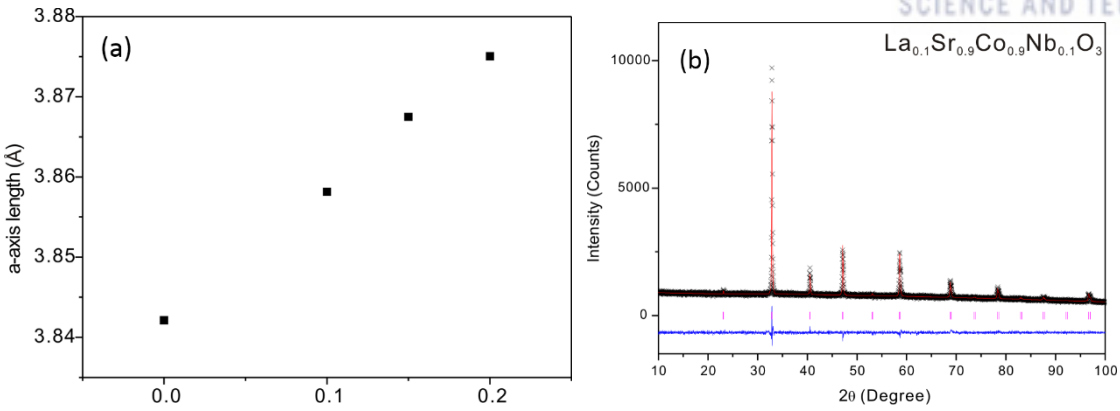

Figure 7.3 (a) Variation of the lattice constant (the *a*-axis length) as a function of the Nb content for $La_{0.1}Sr_{0.9}Co_{1-x}Nb_xO_3$ solid solutions and final Rietveld plot of an example $La_{0.1}Sr_{0.9}Co_{0.9}Nb_{0.1}O_3$. The calculated pattern (red solid line) is compared with observed data (×). The locations of reflections are indicated by magenta vertical bars. The difference between the observed and calculated profiles is shown at the bottom (blue solid line).

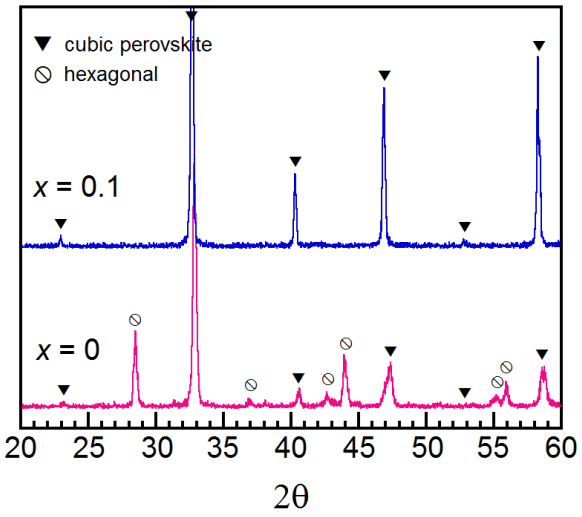

Figure 7.4 XRD patterns of $La_{0.1}Sr_{0.9}Co_{1-x}Nb_xO_{3-\delta}$ (x = 0, 0.1) after annealing at 800 °C for 350 h.

To check the structural stability of LSCNb*x* (x = 0, 0.1), XRD measurements were carried out after annealing at 800 °C for 350 h. As seen in Fig. 7.4, the XRD results show that LSCNb*x* (x = 0) structurally changes from cubic to hexagonal, while LSCNb*x* (x = 0.1) maintains a cubic perovskite structure. This indicates that the cubic perovskite phase is efficiently stabilized after annealing at high temperature, when the LSCNb*x* oxides are doped with Nb for Co at x = 0.1.

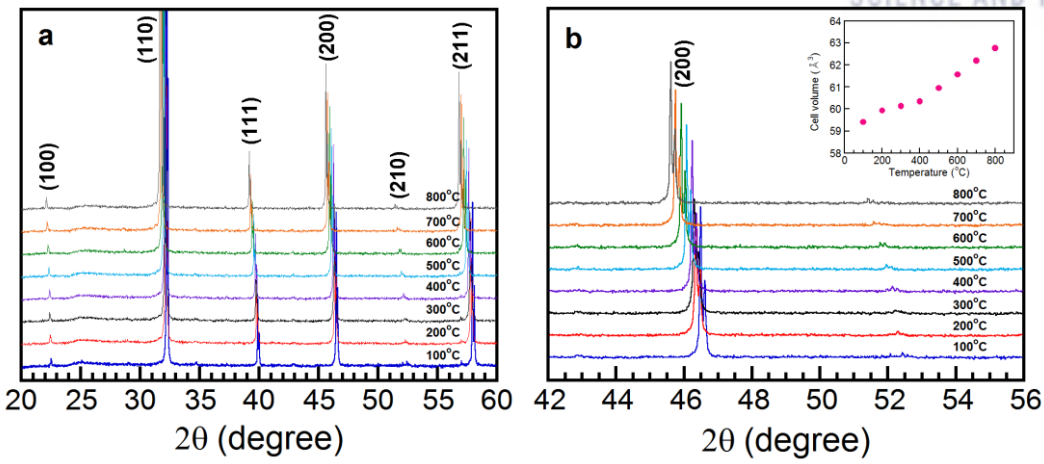

Figure 7.5 (a) In-situ XRD patterns of $La_{0.1}Sr_{0.9}Co_{1-x}Nb_xO_{3-\delta}$ (x = 0.1) at various temperatures, and (b) enlarged in-situ XRD data. The inset shows the effect of temperature on cell volumes (Å ^{3}).

In order to confirm the phase stability at various temperatures (100 to 800 °C) in air, high-temperature XRD measurement was carried out and the results are presented in Fig. 7.5(a). The in-situ XRD patterns of the LSCNbx (x = 0.1) at various temperatures showed that the material retained its perovskite structure over the temperature range (100 to 800 °C). As shown in Fig. 7.5(b), with increasing temperature, the main diffraction peaks obviously shift to lower 2θ, indicating that the volume of the unit cell increases.

The thermogravimetric analyses diagrams of LSCNbx (x = 0.1, 0.15, and 0.2) with temperature in air are shown in Fig. 7.6. The room temperature oxygen contents of $LSCNb_{0.1}$, $LSCNb_{0.15}$, and $LSCNb_{0.2}$ are set to be 2.745, 2.715, and 2.720, respectively, through iodometric titrations. The TGA curves show that significant weight losses occur above 350 °C due to the loss of oxygen from the lattice. The total weight loss of the sample over the entire temperature range decreases with increasing Nb content, possibly due to the stronger Nb-O bond compared to the Co-O bond, which would suppress the oxygen loss of the samples with high Nb content upon heating the samples.[27]

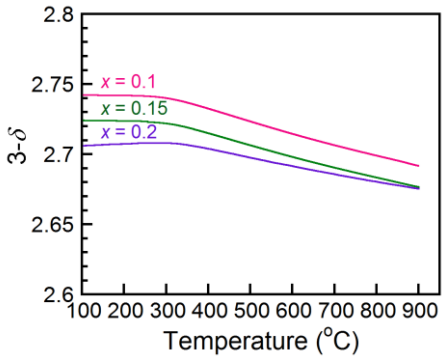

Figure 7.6 TGA data of $La_{0.1}Sr_{0.9}Co_{1-x}Nb_xO_{3-\delta}$ (x = 0.1, 0.15, and 0.2) as a function of temperature.

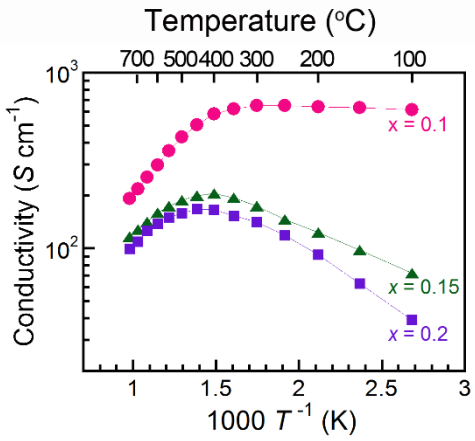

Figure 7.7 Electrical conductivities of $La_{0.1}Sr_{0.9}Co_{1-x}Nb_xO_{3-\delta}$ (x = 0.1, 0.15, and 0.2) in air as a function of temperature.

The temperature dependence of the electrical conductivity of LSCNbx (x = 0.1, 0.15, and 0.2) in air is presented in Fig. 7.7. The electrical conductivity decreases with higher Nb content mainly due to decreasing $Co^{3+/4+}$ which is consistent with previous results.[28] For x = 0.1, the faster decrease in conductivity at higher temperatures could be due to the formation of a significant amount of oxide ion vacancies.[1,2] As shown in Fig. 7.7, the electrical conductivity decreases with the Nb doping content. A different trend has been observed in LSCNbx (x = 0.1, 0.15, 0.2) electrical conductivity results. LSCNbx (x = 0.1) samples presents different slope of electrical conductivity compared to LSCNbx (x = 0.15, 0.2). This change in slope of the electrical conductivity with Nb substitution for Co at high temperatures is explicable by the lattice oxygen loss. This is attributed mainly to the reduction from high valence state Co^{4+} to Co^{3+}, which results in a decrease of the charge carrier concentration.[2,28] In other words, the suppressed oxygen loss from the lattice with increasing Nb content induce less formation of oxygen vacancies and a consequent decrease in charge carriers, which lowers electrical conductivity. For the perovskite MIECs, transport of oxygen ions and electronic conduction are simultaneously achieved in these oxides. The transport of oxygen ions proceeds through the hopping of oxygen vacancies, while transport of electrons is along the B^{n+}-O^{2-}-$B^{(n-1)+}$ network due to overlapping between B:3d and O:2p orbitals.[12] The increase of Nb doping leads to an increase of non-conducting Nb-O bonds, which obstructs electronic transport through O-Co-O bonds and, as a result, decreases the electrical conductivity. [12,16]

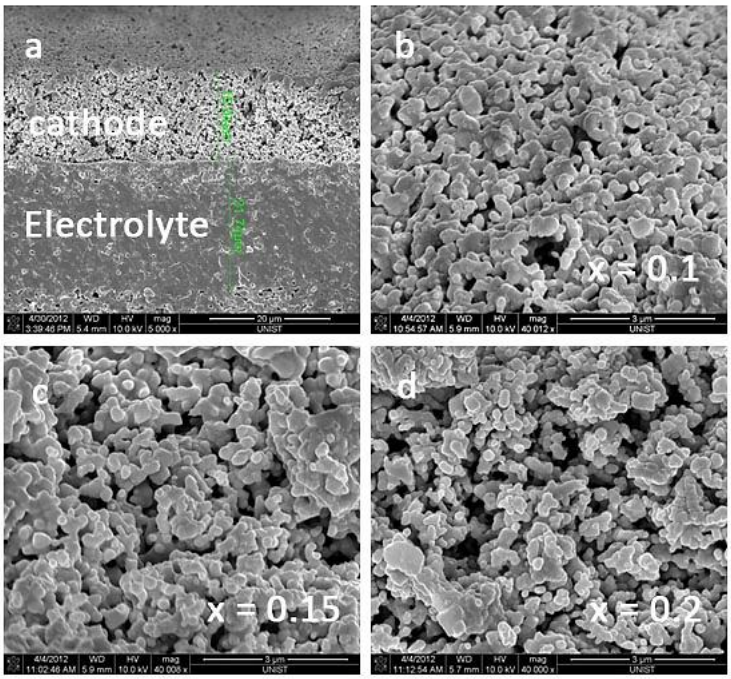

Figure 7.8 SEM images of (a) cross-sectional view of the single cell and $La_{0.1}Sr_{0.9}Co_{1-x}Nb_xO_{3-\delta}$ cathode with GDC electrolyte in a single cell configuration; (b) x = 0.1, (c) x = 0.15, and (d) x = 0.2.

Cross-sectional SEM images of a single cell and cathode are displayed in Fig. 7.8. The bottom side indicates the microstructure of the dense GDC electrolyte and the upper side shows the microstructure of the porous cathode made of LSCNb*x*/GDC (x = 0.1) after calcination at 950 °C, as presented in Fig. 8(a). The thickness of the cathode layer and the GDC electrolyte is approximately 15-20 μm, respectively. The microstructures of all LSCNb*x* (x = 0.1, 0.15, and 0.2) samples are similar, thus showing that the microstructures of the samples are apparently insensitive to Nb substitution.

The impedance spectra for the symmetric cells (LSCNb*x*-GDC/GDC/LSCNb*x*-GDC) by AC impedance spectroscopy with various temperatures in air are shown in Fig. 7.9. The impedance spectra are fitted to the equivalent circuit. The fitting parameters (R_2 and R_3) are presented as a function of Nb content in the inset of Fig. 7.9(a). Based on the literature,[14,29,30] the high and intermediate frequencies behavior of impedance (R_2) is related to ion and electron transfer at the electrode, electrolyte, and collector/electrode interfaces, while the low frequency behavior of impedance, R_3, is associated with non-charge transfer, such as oxygen surface exchange and gas-phase diffusion inside and outside the electrode layer. From these results, the increase of the R_3 with an increase of Nb content are likely to influence oxygen reduction reaction more than other factors.

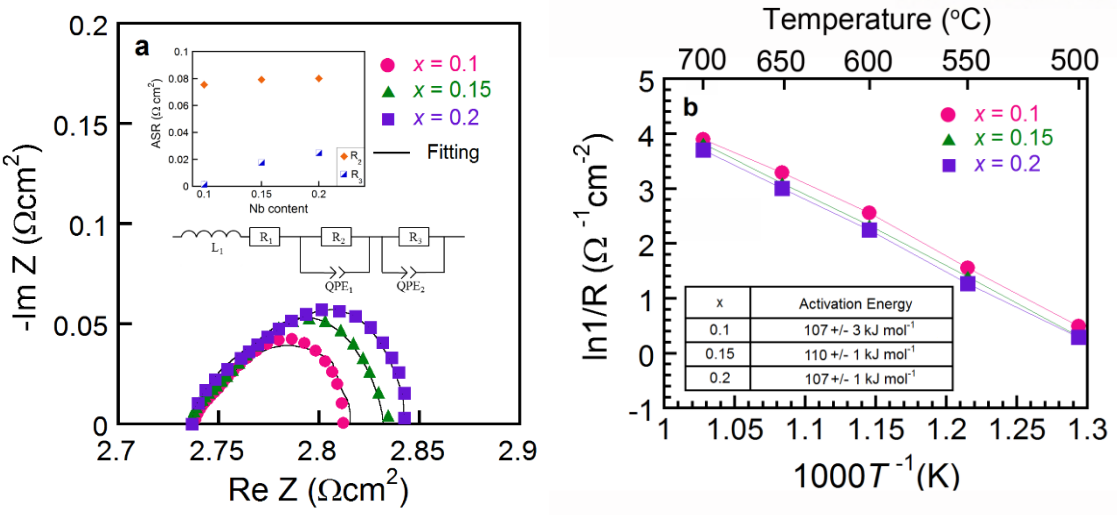

Figure 7.9 (a) Impedance spectra and fitted Nyquist plots with $La_{0.1}Sr_{0.9}Co_{1-x}Nb_xO_{3-\delta}$ (x = 0.1, 0.15, and 0.2) cathode measured under an open-circuit condition at 600 °C in air. (b) Arrhenius plot of the area specific resistance for $La_{0.1}Sr_{0.9}Co_{1-x}Nb_xO_{3-\delta}$ (x = 0.1, 0.15, and 0.2) at various temperatures.

Arrhenius plots of the cathode polarization conductance are provided in Fig. 7.9(b). The non-ohmic resistance values of LSCNbx (x = 0.1, 0.15, and 0.2) symmetrical cells are 0.077 Ω cm^2, 0.097 Ω cm^2, and 0.105 Ω cm^2, respectively at 600 °C. From these data, the apparent activation energies (E_a) of LSCNbx (x = 0.1, 0.15, and 0.2) are calculated to be 107 kJ mol^{-1}, 111 kJ mol^{-1}, and 107 kJ mol^{-1}, respectively. The increase of the ASR with an increase of Nb is possibly due to decreased electrical conductivity and oxygen vacancy concentration.[14,16,31]

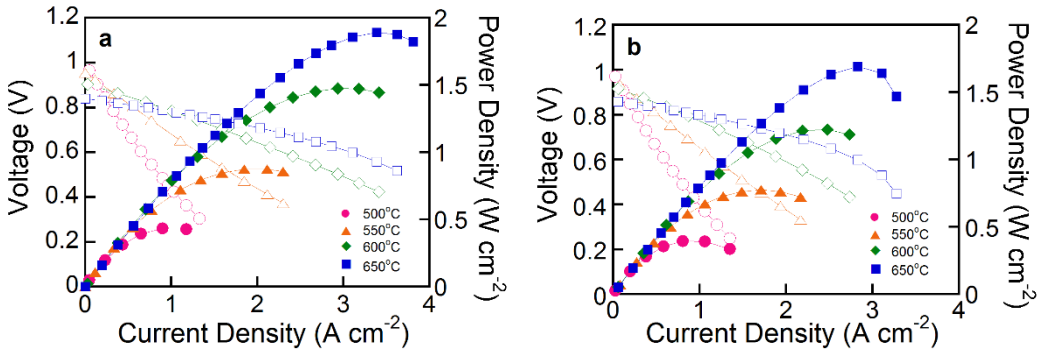

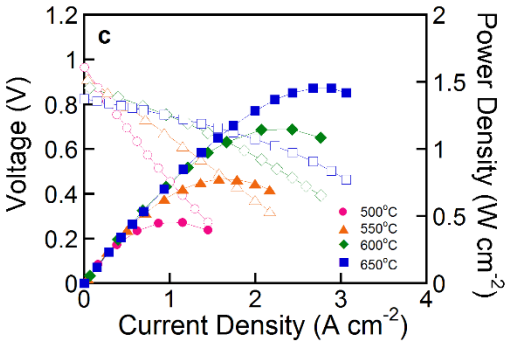

Figure 7.10 *I-V* curves and corresponding power density curves of single cell (Ni-GDC/GDC/ $La_{0.1}Sr_{0.9}Co_{1-x}Nb_xO_{3-\delta}$ at various temperatures; (a) x = 0.1, (b) x = 0.15, and (c) x = 0.2.

The performance of the LSCNb*x* cathodes in SOFCs is measured using the GDC electrolyte with humidified H_2 (3% H_2O) as a fuel and ambient air as an oxidant in a temperature range of 500-650 °C. Figure 7.10 shows the *I-V* curves and the corresponding power density of the LSCNb*x* cathodes. The open-circuit voltages of the LSCNb*x* cells are typically 0.8 V at 700 °C and increase with decreasing operating temperature. The maximum power densities of the LSCNb*x* (x = 0.1, 0.15, and 0.2) cathode material are 1.478, 1.226, and 1.156 W cm^{-2}, at 600 °C, respectively. These results are explained by the higher electrical conductivity of the LSCNb*x* (x = 0.1). Therefore, LSCNb*x* (x = 0.1) is the most favourable cathode material candidate, considering its high electrical conductivity and electrochemical performance for IT-SOFC application.

7.4 Conclusion

LSCNb*x* (x = 0, 0.1, 0.15, and 0.2) perovskite oxides have been investigated as a cathode material for IT-SOFCs. It is observed that Nb doping has a significant effect on the structural stability, electrical conductivity, and electrochemical performance of the LSCNb*x* oxides. A fully stable and cubic perovskite structure could be obtained for the LSCNb*x* oxides with $x \geq 0.1$. LSCNb*x* (x = 0.1, 0.15, and 0.2) oxides show gradually decreasing electrical conductivity with increasing Nb doping at the same temperature. The non-ohmic resistance of LSCNb*x* (x = 0.1, 0.15, and 0.2) symmetrical cells is 0.077 Ω cm^2, 0.097 Ω cm^2, and 0.105 Ω cm^2, respectively, at 600 °C. The increase of the ASR with an increase of Nb (x = 0.1, 0.15, and 0.2), can be explained by the decreased electrical conductivity and oxygen vacancy concentration. The maximum power densities of the single cell are 1.478, 1.226, and 1.156 W cm^{-2}, at 600 °C, respectively, with the LSCNb*x* (x = 0.1, 0.15, and 0.2)-GDC composite cathode showing the best performance at x = 0.1. From these results, the Nb doped LSCNb*x* (x = 0.1) oxide appears to be a favourable IT-SOFC cathode material, considering its structural stability and electrochemical performance.

References

1 Jacobson, A.J.; Materials for solid oxide fuel cells, *Chem. Mater*., **2010**, *22*, 660-674.

2 Lee, K.T.; Manthiram, A.; Comparison of $Ln_{0.6}Sr_{0.4}CoO_{3-\delta}$ (Ln = La, Pr, Nd, Sm, and Gd) as Cathode Materials for Intermediate Temperature Solid Oxide Fuel Cells, *J. Electrochem. Soc*., **2006**, *153*, A794-A798.

3 Zhou, W.; Jin, W.; Zhu, Z.; Shao, Z.; Structural, electrical and electrochemical characterizations of $SrNb_{0.1}Co_{0.9}O_{3-\delta}$ as a cathode of solid oxide fuel cells operating below 600 ^{o}C, *Int. J. Hydrogen Energy*, **2010**, *35*, 1356-1366.

4 Yang, S.; He, T.; He, Q.; $Sm_{0.5}Sr_{0.5}CoO_3$ cathode material from glycne-nitrate process: Formation, characterization, and application in $LaGaO_3$-based solid oxide fuel cells, *J. Alloys Compd.*, **2008**, *450*, 400-404.

5 Zhou, W.; Ran, R.; Shao, Z.; Progress in understanding and development of $Ba_{0.5}Sr_{0.5}Co_{0.8}Fe_{0.2}O_{3-\delta}$-based cathodes for intermediate-temperature solid-oxide fuel cells: A review, J. Power Sources, **2009**, *192*, 231-246.

6 Fukunaga, H.; Koyama, M.; Takahashi, N.; Wen, C.; Yamada, K.; Reaction model of dense $Sm_{0.5}Sr_{0.5}CoO_3$ as SOFC cathode, *Solid State Ionics*, **2000**, *132*, 279-285.

7 Acuña, L.M.; Peña-Martínez, J.; Marrero-López, D.; Fuentes, R.O.; Nuñez, P.; Lamas, D.G.; Electrochemical performance of nanostructured $La_{0.6}Sr_{0.4}CoO_{3-\delta}$ and $Sm_{0.5}Sr_{0.5}CoO_{3-\delta}$ cathodes for IT-SOFCs, *J. Power Sources*, **2011**, *196*, 9276-9283.

8 Choi, S.; Shin, J.; Kim, G.; The electrochemical and thermodynamic characterization of $PrBaCo_{2-x}Fe_xO_{5+\delta}$ (x = 0, 0.5, 1) infiltrated into yttria-stabilized zircornia scaffold as cathodes for solid oxide fuel cells, *J. Power Sources*, **2012**, *201*, 10-17.

9 Shao, Z. P; Haile, S. M.; A high-performance cathode for the next generation of solid-oxide fuel cells. *Nature* **2004**, *431*, 170-173.

10 Petrov, A.N.; Kononchuk, O. F.; Andreev, A. V.; k Cherepanov, V.A.; Kofstad, P.; Self-compensation characteristics of Eu ions in $BaTiO_3$, *Soid State Ionics*, **1995**, *80*, 189.

11 Kawada, T.; Suzuki, J.; Sase, M.; Kaimai, A.; Yashiro, K.; Nigara, Y.; Determination of Oxygen Vacancy Concentration in a Thin Film of $La_{0.6}Sr_{0.4}CoO_{3-\delta}$ by an Electrochemical Method, *J. Electrochem. Soc.*, **2002**, *149*, E252-E259.

12 Deng, Z.Q.; Smit, J.P.; Niu, H.J.; Evans, G.; Li, M.R.; Xu, Z.L.; Claridge, J.B.; Rosseinsky, M.J.; B Cation Ordered Double Perovskite $Ba_2CoMo_{0.5}Nb_{0.5}O_{6-\delta}$ As a Potential SOFC Cathode, *Chem. Mater.*, **2009**, *21*, 5154-5162.

13 Zhou, W.; Jin, W.; Zhu, Z.; Shao, Z.; Structural, electrical and electrochemical characterizations of $SrNb_{0.1}Co_{0.9}O_{3-\delta}$ as a cathode of solid oxide fuel cells operating below 600

°C, *Int. J. Hydrogen Energy*, **2010**, *35*, 1356-1366.

14 Adler, S.B.; Lane, J.A.; Steele, B.C.H.; Electrode Kinetics of Porous Mixed-Conducting Oxygen Electrodes, *J. Electrochem. Soc*., **1996**, *143*, 3554-3564.

15 Kruidhof, H., Bouwmeester, H.J.M.; Doorn, R.H.E.v.; Burggraaf, A. J.; Influence of order-disorder transitions on oxygen permeability through selected nonstoichiometric perovskite-type oxides, *Solid State Ionics*, 1996, **63-65**, 816-822.

16 Deng, Z.Q.; Yang, W.S.; Liu, W.; Chen, C.S.; Relationship between transport properties and phase transformations in mixed-conducting oxides, *J. Solid State Chem*., **2006**, *179*, 362-369.

17 Harrison, W.T.A.; Lee, T.H.; Yang, Y. L.; Scarfe, D. P.; Liu, L.M.; Jacobson, A. J.; A neutron diffraction study of two strontium cobalt iron oxides, *Mater. Res. Bull*., 1995, **30**, 621-630.

18 Lee, S.J.; Muralidharan, P.; Jo, S.H.; Kim, D.K.; Composite cathode for IT-SOFC: Sr-doped lanthanum cuprate and Gd-doped ceria, *Electrochem. Comm*., **2010**, *12*, 808-811.

19 Shen, P.J.; Liu, X.; Wang, H.H.; Ding, W.Z.; Niobium Doping Effects on Performance of $BaCo_{0.7}Fe_{0.3-x}Nb_xO_{3-\delta}$ Perovskite, *J. Phys. Chem. C*, **2010**, 114, 22338-22345.

20 Nagai, T.; Ito, W.; Sakon, T.; Relationship between cation substitution and stability of perovskite structure in $SrCoO_{3-\delta}$ based mixed conductors, *Solid State Ionics*, **2007**, *177*, 3433-3444.

21 Yang, Z.; Yang, C.; Jin, C.; Han, M.; Chen, F.; $Ba_{0.9}Co_{0.7}Fe_{0.2}Nb_{0.1}O_{3-\delta}$ as cathode material for intermediate temperature solid oxide fuel cells, *Electrochem. Comm*., **2011**, *13*, 882-885.

22 Larson, A.C.; Dreele, R.B.v.; General Structural Analysis System (GSAS); Los Alamos National Laboratory: Los Alamos, NM, **1987**.

23 James, M.; Tedesco, T.; Cassidy, D.J.; Withers, R.L.; Oxygen vacancy ordering in strontium doped rare earth cobaltate perovskite $Ln_{1-x}Sr_xCoO_{3-\delta}$ (Ln = La, Pr and Nd; $x > 0.60$), *Mater. Res. Bull*., 2005, **40**, 990-1000.

24 Dieterle, L.; Bach, D.; Schneider, R.; Störmer, H.; Gerthsen, D.; Guntow, U.; Ivers-Tiffée, E.; Weber, A.; Peters, C.; Yokokawa, H.; Structural and chemical properties of nanocrystalline $La_{0.5}Sr_{0.5}CoO_{3-\delta}$ layers on yttria-stabilized zircornia analysed by transmission electron microscopy, *J. Mater. Sci*., 2008, **43**, 3135-3143.

25 A. Weizman, D. Fuks, E.A. Kotomin and D. Gryaznov, *Solid State Ionics*, 2013, **230**, 32

26 R.D. Shannon, *Acta Crystallogr. Sect. A*, 1976, **A32**, 751

27 F. Wang, Q. Zhou, T. He, G. Li and H. Ding, *J. Power Sources*, 2010, **195**, 3772

28 S. Yoo, T.H. Lim, J. Shin, G. Kim, *J. Power Sources*, 2013, **226**, 1.

29 S.B. Adler, X.Y. Chen and J.R. Wilson, *J. Catal*., 2007, **245**, 91

30 D. Chen, R. Ran, K. Zhang, J. Wang and Z. Shao, *J. Power Sources*, 2009, **188**, 96

31 Q. Li, H. Zhao, L. Huo, L. Sun, X. Cheng and J.-C. Grenier, *Electrochem. Commun*., 2007, **9**, 1508

Chapter 8. Investigation of layered perovskite type $NdBa_{1-x}Sr_xCo_2O_{5+\delta}$ (x = 0, 0.25, 0.5, 0.75, and 1.0) cathodes for intermediate-temperature solid oxide fuel cells

8.1 Introduction

Solid oxide fuel cells (SOFCs) have been researched as new power generation devices because of their high conversion efficiency, low emissions, and excellent fuel flexibility. The requirement for high operating temperature (800 to 1000 ^oC), however, give rise to crucial issues such as high costs and high rates of formation of electrical and chemical insulating phases due to the solid state reaction between the SOFC components during the cell fabrication and operation. Therefore, the focus of research on SOFC technology has shifted towards intermediate operating temperatures ranging from 500 ^oC to 700 ^oC.[1-3] This reduction of operating temperature, however, leads to a significant decrease in electrode activity. For intermediate temperature SOFCs (IT-SOFCs), cathode materials with high electrocatalytic activity for the oxygen reduction reaction should be developed, because the cell performances at intermediate temperatures are mostly limited by polarization loss at the cathode.[1-4]

In this regard, mixed oxide-ion and electronic conductors (MIECs) with perovskite oxides have received tremendous attention as potential cathodes for IT-SOFCs, because the oxygen reduction reaction in MIEC electrodes is governed by the oxygen surface exchange and oxygen diffusion.[5,6] The reaction sites of MIECs can extend the electrochemically active area as a result of the oxygen exchange reaction occurring not only on the triple phase boundary (TPB) between the electrolyte, cathode, and gas phase but also on the two phase boundary between the electrode and gas phase.[6,7] Many simple perovskite-type MIECs such as $Pr_{1-x}Sr_xCoO_3$,[8] $Sm_{0.5}Sr_{0.5}CoO_3$,[9] $BaCoO_3$,[10] and $LaFeO_3$[11] have been extensively studied owing to their high electrical conductivity and high catalytic activity for the oxygen reduction reaction.

Recently, several groups have reported a class of layered perovskite oxides, based on their much higher chemical diffusion and surface exchange coefficients relative to those of ABO_3-type perovskite oxides.[12-14] The layered perovskite oxides can be described with the general formula $AA'B_2O_{5+\delta}$, with the A-site being a rare earth element, the A′ site an alkaline earth element, and the B-site a transition element. These oxides consist of sequential layers $[BO_2]$-[AO]-$[BO_2]$-[A′O] stacked along the c-axis.[15] This layered structure reduces the oxygen bonding strength in the [AO] layer and provides a disorder-free channel for ion motion, which enhances oxygen ion diffusivity.[16]

Based on these properties, layered perovskites such as $LnBaCo_2O_{5+\delta}$ (Ln = Pr, Nd, Sm, and Gd) perovskites have been studied for their capability for application as IT-SOFC cathode materials. Kim *et al.*[17] reported that $PrBaCo_2O_{5+\delta}$ (PBCO) offers rapid oxygen ion diffusivity and a surface exchange coefficient at the IT range. These characteristics have strong potential to improve the conductivity and

catalytic activity for the ORR of layered perovskite oxides. In addition, several groups have reported that the substitution of Sr for Ba in $LnBaCo_2O_{5+\delta}$ can improve the conductivity and the catalytic activity for the ORR of layered perovskite oxides.[18-20] Kim *et al*.[14] demonstrated that Sr-doped layered perovskite materials are promising cathode materials for use in IT-SOFC applications. When the Ba site is partially substituted by Sr, it can potentially improve the conductivity of layered perovskite oxides.[21] McKinlay *et al*.[22] reported that the conductivity of the Sr-doped layered perovskite oxide is very high, about 32 times higher than that of a Sr-free sample. The Sr-doped layered perovskite oxide, moreover, showed a lower polarization resistance and could be employed as a cathode material for SOFCs. Their studies, however, focus on only one composition, $x = 0.5$, in $NdBa_{1-x}Sr_xCo_2O_{5+\delta}$ and do not provide a systematic investigation with Sr doping. In this study, we investigate Sr doping on the crystal characteristics, electrical properties, and electrochemical performances of $NdBa_{1-x}Sr_xCo_2O_{5+\delta}$ (x = 0, 0.25, 0.5, 0.75, and 1.0) with regard to its application as an IT-SOFC cathode material. In addition, thermodynamic redox behavior is also examined in order to identify the applicability of the material to IT-SOFCs.

8.2 Experimental

$NdBa_{1-x}Sr_xCo_2O_{5+\delta}$ oxides were synthesized using the Pechini process to form submicron powder particles. Metal nitrates are employed both as metal precursors and oxidizing agents. Stoichiometric amounts of $Nd(NO_3)_3 \cdot 6H_2O$ (Aldrich, 99.9%, metal basis), $Ba(NO_3)_2$ (Aldrich, 99+%), and $Sr(NO_3)_2$ (Aldrich, 99+%), $Co(NO_3)_2 \cdot 6H_2O$ (Aldrich, 98+%) were added into a beaker containing a suitable amount of a concentrated nitric acid solution under continuous heating and stirring. An adequate amount of ethylene glycol was added into the beaker after the mixture was dissolved. After a viscous resin was formed, the mixture was heated around 200 °C. The resultants were pre-calcined at 600 °C for 4 h, ball-milled in acetone for 24 h, and calcined at 1000 °C for 12 h in air. The calcined powders were then ground, pressed into pellets, and sintered at 1100 °C for 12 h in air.

The structure and the morphology of the $NdBa_{1-x}Sr_xCo_2O_{5+\delta}$ were characterized by X-ray diffraction (XRD) and scanning electron microscopy (SEM). X-Ray powder diffraction measurements (Rigaku diffactormeter, Cu Ka radiation) were performed to confirm the structure with a scan rate of 0.5^o min^{-1}.

Coulometric-titration was used to evaluate the exact redox state of the composite as a function of $p(O_2)$.[23,24] In coulometric titration, the $p(O_2)$ of the gases over an equilibrated sample is measured electrochemically with an oxygen sensor. The oxide-YSZ composite was placed in a sealed container at the temperature of interest and equilibrated sufficiently by passing a mixture of gases (for the present study, 5% O_2 in Ar) over it. The sample was then isolated in the tube and the equilibrium $p(O_2)$ was measured with an oxygen sensor. The oxygen sensor was part of the container wall and could also be

used to add or remove oxygen from the system through application of a potential across the ion-conducting YSZ tube. Electrodes on either side of the YSZ tube were used to measure the potential across the membrane, and the potential could be related to the $p(O_2)$ through the Nernst Equation. A precise amount of charge could be passed across the tube using a BioLogic Potentiostat, with 1 Coulomb of charge being equivalent to 2.6 μmol of O_2. A yttria-stabilized zirconia (YSZ) tube (McDanel Advanced Ceramic Technologies, Z15410630) was used both to electrochemically pump oxygen out of the system and to sense the equilibrium $p(O_2)$ inside the tube. The criterion we used for establishing equilibrium in coulometric titration was that the potential of the oxygen sensor changed by less than 1 mV h^{-1}. The electrical conductivity was measured with the four-probe method with a BioLogic Potentiostat.

The glycine-nitrate process (GNP), which can produce fine particles, was used to prepare $NdBa_{1-x}Sr_xCo_2O_{5+\delta}$ for the electrode and electrolyte. The glycine was applied to the solution at a molar ratio of 1:1.5 for metal nitrate and glycine. The electrode powders were blended with a binder (Heraeus V006) to form slurries for the cell performance test.

Electrochemical performances of the $NdBa_{1-x}Sr_xCo_2O_{5+\delta}$ cathode were evaluated with Ni-GDC anode-supported single cells. To measure cell performance**,** the $NdBa_{1-x}Sr_xCo_2O_{5+\delta}$ powders and GDC were mixed at a weight ratio of 6 : 4 and ball-milled for 12 h. A Ni-GDC cermet anode was then fabricated from a mixture of nickel oxide, GDC prepared by GNP, and starch at a weight ratio of 6 : 4 : 1.5. This mixture was ball-milled in ethanol for 24 h. The GDC powder electrolyte was pressed over the pelletized Ni-GDC cermet anode. The Ni-GDC/GDC anode-electrolyte layer was sintered at 1350 °C for 5 h. For the top layer cathode, the $NdBa_{1-x}Sr_xCo_2O_{5+\delta}$ slurries were screen-printed on the GDC electrolyte. The cells, with an active electrode area of 0.36 cm^2, were finally sintered at 950 °C for 2 h under an air atmosphere. Ag wires were attached to both the anode and cathode of a single cell using Ag paste as a current collector. An alumina tube was employed to fix the single cell using a ceramic adhesive (Aremco, Ceramabond 553). H_2 containing 3% H_2O was applied through a water bubbler with a flow rate of 20 mL min^{-1}, while air was applied as an oxidant and supplied to the cathode by ambient air flow during the single cell test. A BioLogic Potentiostat was used to measure impedance spectra and *I-V* curves. Impedance spectra were recorded under OCV in a frequency range of 1 mHz to 500 kHz with AC perturbation of 14 mA at 700 °C.

8.3 Results

The detailed data of the crystal structures of $NdBa_{1-x}Sr_xCo_2O_{5+\delta}$ oxides are shown in Fig. 8.1 and structural data are given in Table 8.1. The XRD patterns present that all $NdBa_{1-x}Sr_xCo_2O_{5+\delta}$ oxides are single phase without any detectable secondary phases. The Rietveld refinement data show that the structure of the $NdBa_{1-x}Sr_xCo_2O_{5+\delta}$ (x = 0, 0.25, 0.5, 0.75, and 1.0) samples changes with increasing Sr content from orthorhombic (space group *Pmmm*) for x = 0, 0.25 to tetragonal (space group *P4/mmm*) for x = 0.5, 0.75.[25] The fully Sr-doped $NdSrCo_2O_{5+\delta}$ has been reported to have an orthorhombic structure with a space group of *Pbnm*. The data in Table 8.1 indicate that the lattice parameters and the unit cell volume of the $NdBa_{1-x}Sr_xCo_2O_{5+\delta}$ samples decrease with increasing Sr content due to substitution of the smaller ionic radii of Sr^{2+} for Ba^{2+}. As an example of refinement of $NdBa_{1-x}Sr_xCo_2O_{5+\delta}$ (x = 0.5), Fig. 8.1(b) shows the measured XRD data, the calculated profile, and the difference between them for $NdBa_{1-x}Sr_xCo_2O_{5+\delta}$ (x = 0.5). There is good agreement between the experimental data and the calculated profiles, suggesting that cations are well ordered between Nd^{3+} and Ba^{2+}/Sr^{2+} ions in the ordered perovskite lattice.

The chemical reactivity of the $NdBa_{1-x}Sr_xCo_2O_{5+\delta}$ (x = 0, 0.25, 0.5, 0.75, and 1.0) cathodes in contact with the GDC electrolyte was assessed by heating the mixed powders at 950 °C for 4 h. Fig. 8.2 compares the XRD patterns of the $NdBa_{1-x}Sr_xCo_2O_{5+\delta}$ (x = 0.5) and GDC cathode slurries painted on the GDC electrolyte. $NdBa_{1-x}Sr_xCo_2O_{5+\delta}$ (x = 0.5) samples with the GDC show no impurity reflections in Fig. 8.2.

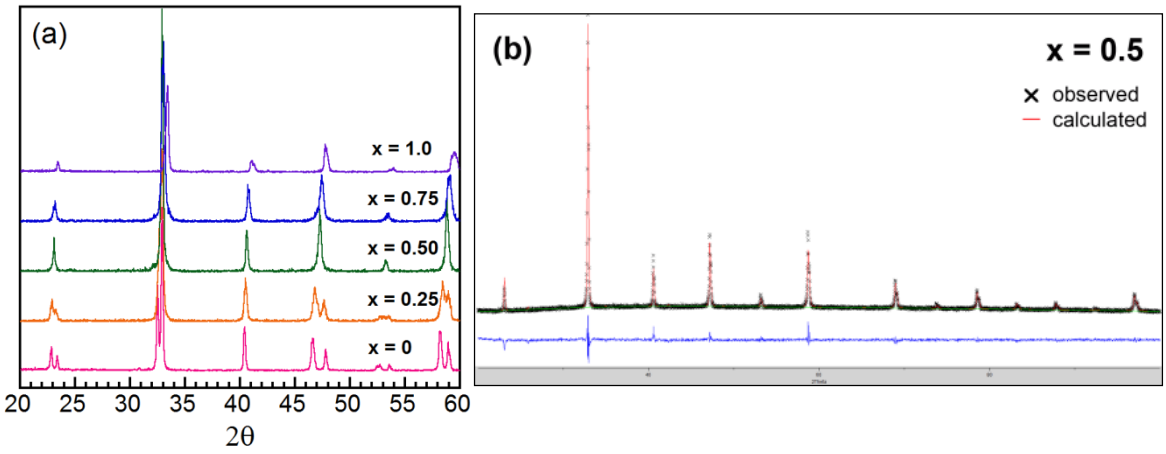

Figure 8.1 (a) XRD pattern of $NdBa_{1-x}Sr_xCo_2O_{5+\delta}$ (x = 0, 0.25, 0.5, 0.75, and 1.0) after being sintered at 1100 °C, and (b) Rietveld refinement of $NdBa_{1-x}Sr_xCo_2O_{5+\delta}$ (x = 0.5) data from room temperature.

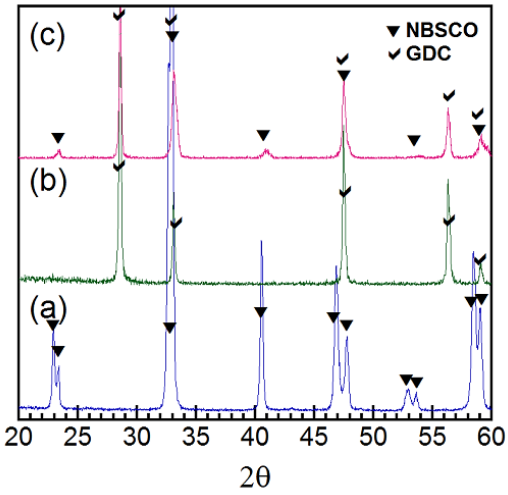

Figure 8.2 Chemical stability of the $NdBa_{1-x}Sr_xCo_2O_{5+\delta}$ (x = 0.25) samples against the GDC electrolyte after being sintered at 950 °C for 4 h. (a) $NdBa_{1-x}Sr_xCo_2O_{5+\delta}$ (x = 0.25), (b) GDC electrolyte, and (c) $NdBa_{1-x}Sr_xCo_2O_{5+\delta}$ (x = 0.25)-GDC composite.

The microstructure of the $NdBa_{1-x}Sr_xCo_2O_{5+\delta}$ (x = 0, 0.25, 0.5, 0.75, and 1.0) cathode was examined by scanning electron microscopy (SEM) in Fig. 8.3. The electrode microstructure is related to the characteristics of the surface area, electrochemically active area, volume fraction of chemical phases present, and electron transport.[26,27] Each sample shows porous morphology properties in the cathode as well as connectivity between the cathode and the GDC electrolyte without cracks or pin holes. The $NdBa_{1-x}Sr_xCo_2O_{5+\delta}$ electrode and GDC electrolyte layers are approximately 20 μm in thickness. The microstructures of all $NdBa_{1-x}Sr_xCo_2O_{5+\delta}$ samples are similar, indicating that the microstructures of the samples are insensitive to Sr substitution.

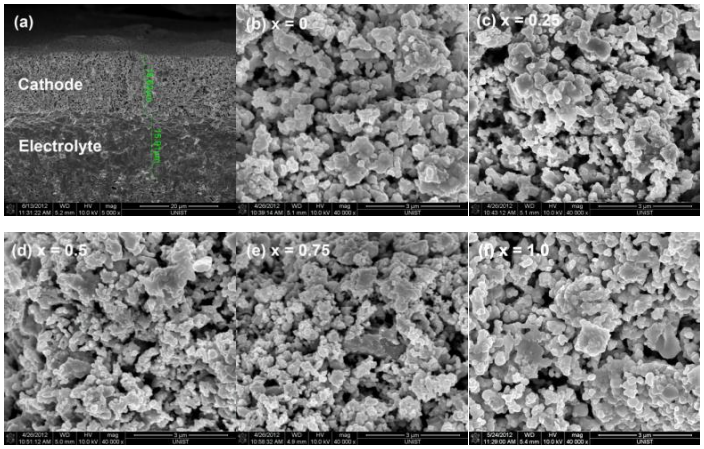

Figure 8.3 SEM images of (a) cross-sectional view of the single cell and $NdBa_{1-x}Sr_xCo_2O_{5+\delta}$ cathode with GDC electrolyte in a single cell configuration; (b) x = 0, (c) x = 0.25, (d) x = 0.5, (e) x = 0.75, and (f) x = 1.0

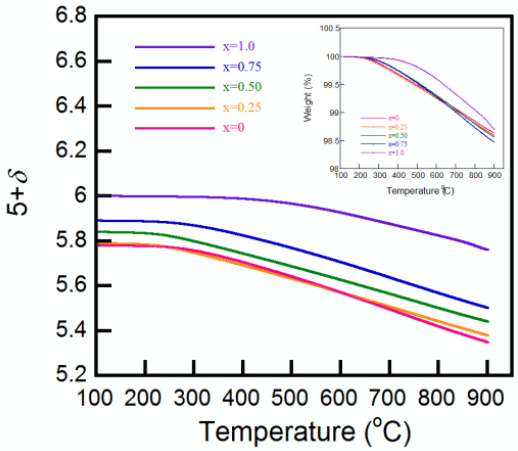

Figure 8.4 Thermogravimetric data of $NdBa_{1-x}Sr_xCo_2O_{5+\delta}$ (x = 0, 0.25, 0.5, 0.75, and 1.0) as a function of temperature.

The results of the thermogravimetric analysis of $NdBa_{1-x}Sr_xCo_2O_{5+\delta}$ cathodes with temperature in air are shown in Fig. 8.4. The inset in Fig. 8.4 shows TGA data collected by the weight change of $NdBa_{1-x}Sr_xCo_2O_{5+\delta}$ samples. All the $NdBa_{1-x}Sr_xCo_2O_{5+\delta}$ samples start to lose oxygen at T > 200 °C, and the weight loss of the samples increases with increasing Sr content, possibly due to loss of interstitial oxygen from the lattice. According to the iodometric titration results presented in Table 1, the initial oxygen content increases from 5.78 to 6.0 with increasing Sr content at room temperature. This can be explained by the increasing coordination number and oxygen content values resulting from the smaller size difference between Nd^{3+} (112 pm) and Sr^{2+} (132 pm) ions compared to that between Nd^{3+} (112 pm) and Ba^{2+} (149 pm) and consequent perturbation of the ordering between the Nd and Ba layers.[22] The high oxygen stoichiometry may be responsible for the high diffusivity of oxide ions in the bulk and the enhanced surface activity toward the ORR.[17]

The electrical conductivity of the $NdBa_{1-x}Sr_xCo_2O_{5+\delta}$ cathodes is presented in the temperature range of 100 to 750 °C under an air condition, as seen in Fig. 8.5. All samples show a decrease in electrical conductivity with increasing temperature, showing metallic behavior over the entire temperature range. Their conductivities start to decrease significantly at about 300 °C due to such lattice defects breaking the Co-O-Co bonds, resulting in a loss of oxygen atoms from the lattice and reduction of Co^{4+} to Co^{3+}.[28]

The predominant defects in $NdBa_{1-x}Sr_xCo_2O_{5+\delta}$ are interstitial oxygens O_i'' and electronic holes $h^\bullet = Co^\bullet{}_{Co}$,[29] according to the Kröger-Vink notation,[30] and the following pseudo-chemical reaction shows the interaction between the defects and the atmosphere.

$$\frac{1}{2}O_2(g) + V_i{}^x + Co^x{}_{Co} \rightleftarrows O_i'' + 2Co^\bullet{}_{Co} \quad (1)$$

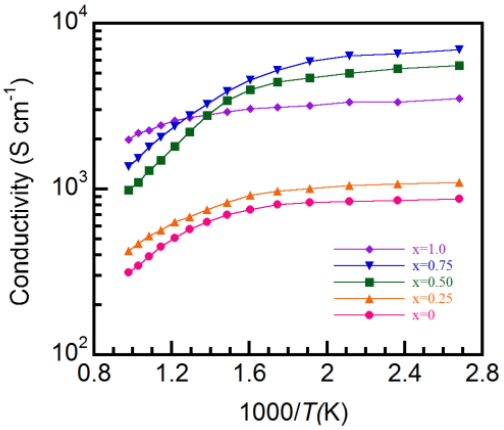

Figure 8.5 The electrical conductivity data for $NdBa_{1-x}Sr_xCo_2O_{5+\delta}$ (x = 0, 0.25, 0.5, 0.75, and 1.0) as a function of temperature in air.

The electroneutrality produces the following equation:

$$2[O_i''] = [Co^{\bullet}_{Co}] \tag{2}$$

At a given temperature, therefore, the electrical conductivity increases with increasing Sr content due to the increasing electronic holes associated with oxygen content, reaching a maximum at x = 0.75 from the higher oxygen content, as determined by the TGA results. A moderate decrease in electrical conductivity compared to other compositions, however, is observed at x = 1.0 and is ascribed to a structural change to a simple perovskite.[22]

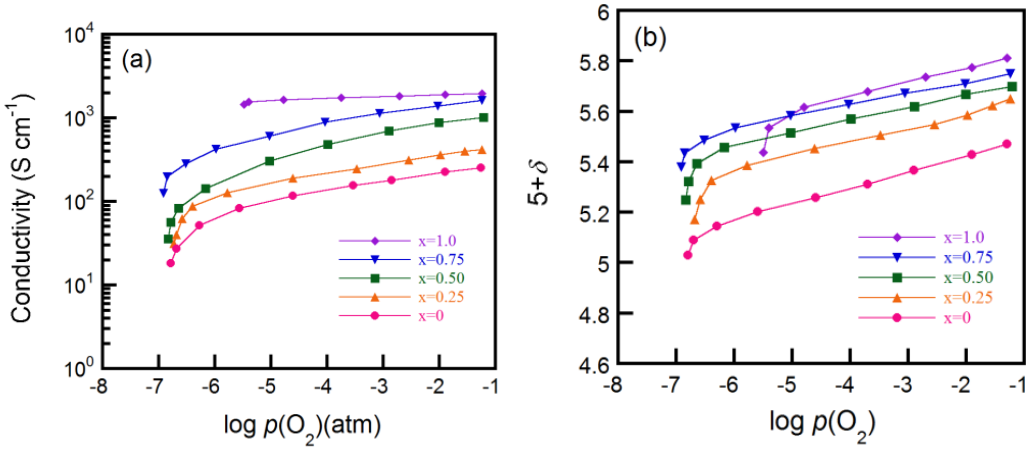

Figure 8.6 The electrical conductivities of the $NdBa_{1-x}Sr_xCo_2O_{5+\delta}$ (x = 0, 0.25, 0.5, 0.75, and 1.0) in various $p(O_2)$ and the isotherms of the $NdBa_{1-x}Sr_xCo_2O_{5+\delta}$ (x = 0.25, 0.5, 0.75, and 1.0) at 700 °C

The interface of SOFCs between the electrolyte and the cathode experiences a lower $p(O_2)$ under operating conditions, which may cause redox degradation of the cathode and affect the long term stability of the cathode performance.[31] Characterization of the basic redox properties is therefore essential, especially under circumstances where the cathode is subjected to relatively low oxygen partial pressures. Basic redox properties including the electrical conductivity and the oxygen nonstoichiometry are also investigated in this study.[9,32] The electrical conductivities of $NdBa_{1-x}Sr_xCo_2O_{5+\delta}$ cathodes over a wide range of $p(O_2)$ at 700 ºC are presented in Fig. 8.6(a). As $p(O_2)$ is lowered, the electrical conductivities decrease due to a reduction of the concentration of the oxygen species in the fluorite layers, showing typical *p*-type electronic conductor behavior, from Equation (1) and (2).

Figure 8.6(b) shows the oxygen nonstoichiometries for $NdBa_{1-x}Sr_xCo_2O_{5+\delta}$ determined by coulometric titration as a function of $p(O_2)$ at 700 ºC. The initial oxygen content of all samples is determined by iodometric titration and TGA data in air at 700 ºC, as seen in Table 8.1. The data show that the isotherms of $NdBa_{1-x}Sr_xCo_2O_{5+\delta}$ at three different temperatures (650, 700, and 750 ºC) have similar shapes, suggesting that the reduction mechanisms are quite similar. All the $NdBa_{1-x}Sr_xCo_2O_{5+\delta}$ samples start to decay at a $p(O_2)$ of approximately 10^{-6} atm and appear to decompose at a $p(O_2)$ of 10^{-7} atm. This indicates that the decomposition begins to affect the electrical characteristics of the $NdBa_{1-x}Sr_xCo_2O_{5+\delta}$ even before the end of the decomposition. The steep change near 10^{-7} atm and 700 ºC implies that the operating $p(O_2)$ of $NdBa_{1-x}Sr_xCo_2O_{5+\delta}$ should be carefully reviewed considering the structural instability predicted from the redox behavior.[33]

The area specific resistance (ASR) is used to describe all resistance terms associated with the electrode, which occur at the gas-cathode interface, within the bulk of the cathode, and at the cathode-electrolyte interface. The typical impedance spectra for the symmetrical cells ($NdBa_{1-x}Sr_xCo_2O_{5+\delta}$-GDC/GDC/$NdBa_{1-x}Sr_xCo_2O_{5+\delta}$-GDC) were obtained by AC impedance spectroscopy under various temperatures in air. In these spectra, the intercepts with the real axis at low frequency designate the total resistance of the cell and the value of high frequency is the ohmic resistance of the cell.

Table 9.1 Space group and structure parameters of $NdBa_{1-x}Sr_xCo_2O_{5+\delta}$ oxides

x	Space group	a (Å)	b (Å)	c (Å)	volume (Å)^3	Oxygen contents
0	*Pmmm*	3.9177	3.9085	7.6348	116.85	5.78
0.25	*Pmmm*	3.8959	3.8834	7.6460	115.67	5.78
0.5	*P4/mmm*	3.8944	3.8943	7.6150	115.48	5.89
0.75	*P4/mmm*	3.8945	3.8945	7.6102	115.42	5.89
1.0	*Pbnm*	5.3740	5.4201	7.6020	221.443	3.0

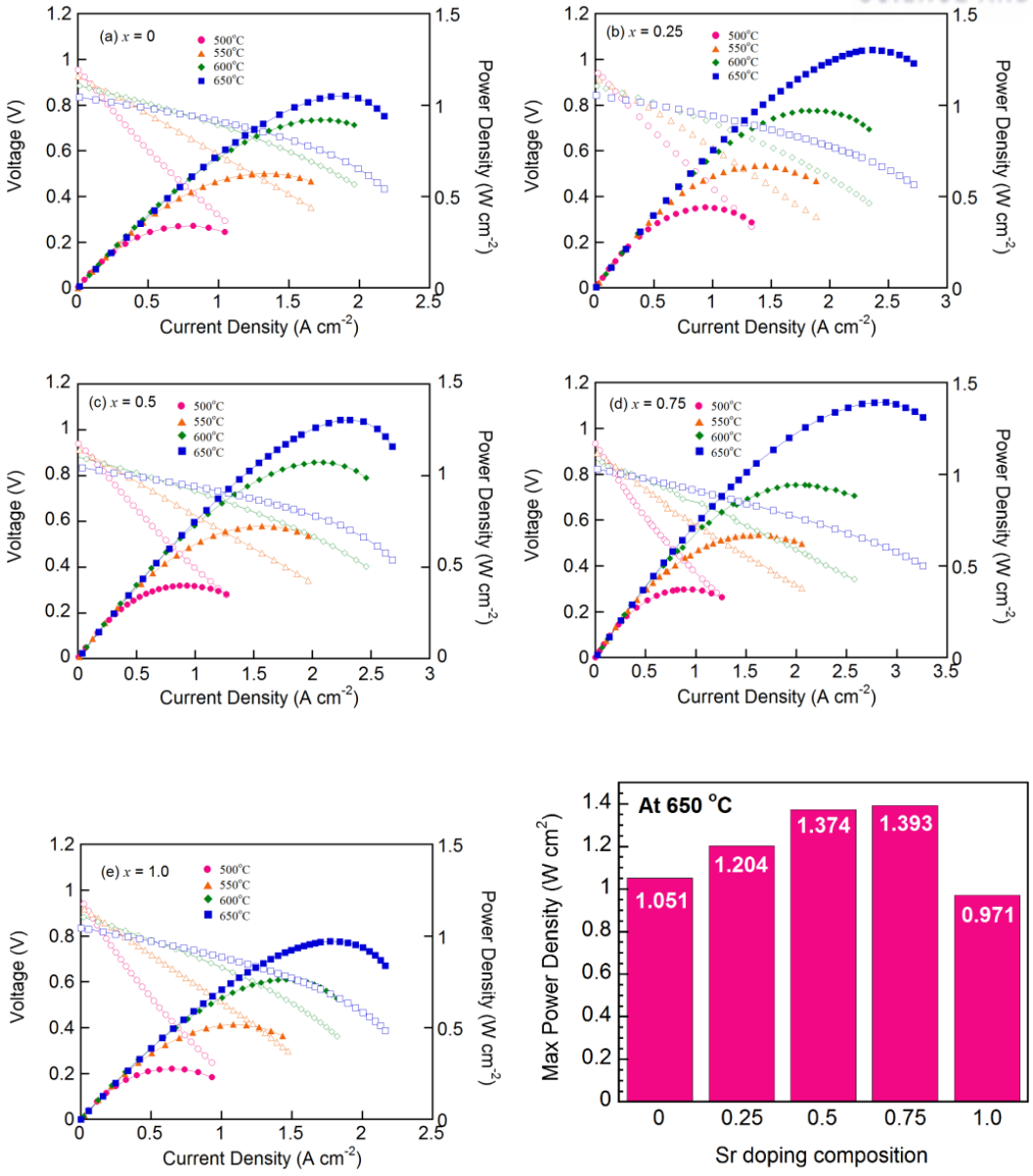

Figure 8.7 *I-V* curves and corresponding power density curves of a single cell (Ni-GDC/GDC /$NdBa_{1-x}Sr_xCo_2O_{5+\delta}$) ($x$ = 0.25, 0.5, 0.75, and 1.0) at various temperatures.

The *I-V* curves and the corresponding power density of $NdBa_{1-x}Sr_xCo_2O_{5+\delta}$-GDC cathodes with humidified H_2 (3% H_2O) as a fuel and static ambient air as an oxidant in a temperature range of 500-650 °C are shown in Fig. 8.7. The open circuit voltages (OCVs) are near the theoretical value derived from the Nernst equation, which shows that the cell is well sealed with a gas-tight electrolyte. The fuel cell performances for $x \leq 0.75$ are improved with increasing strontium content in the $NdBa_{1-x}Sr_xCo_2O_{5+\delta}$ oxides. At 600 °C, the maximum power density is about 1.0 W cm^{-2} at both x = 0.5 and 0.75, which is clear evidence of a strontium effect in $NdBa_{1-x}Sr_xCo_2O_{5+\delta}$ layered perovskites. Based on the data

presented above, the strontium contents at x = 0.5 and 0.75 in $NdBa_{1-x}Sr_xCo_2O_{5+\delta}$ reflect a tetragonal lattice geometry while an orthorhombic geometry is obtained at x = 0 and 0.25 with the layered perovskite structures. The Sr substitution improves the bulk oxygen diffusion, because the tetragonal structure exhibits faster oxygen transport in the bulk and surface and higher catalytic activity for the oxygen reduction reaction as compared to an orthorhombic structure.[17,22,34-36] Therefore, the enhanced catalytic activity of the x = 0.5 and 0.75 samples may be related to faster oxygen transport compared to that in the x = 0 and 0.25 samples.

8.4 Conclusion

$NdBa_{1-x}Sr_xCo_2O_{5+\delta}$ layered perovskite oxides have been investigated as a cathode material for IT-SOFCs. The electrical conductivity improves with increasing Sr content due to the increased concentration of mobile interstitial oxygen and electronic holes. At 700 ^oC, all the $NdBa_{1-x}Sr_xCo_2O_{5+\delta}$ samples start to decay at a $p(O_2)$ of approximately 10^{-6} atm and appear to decompose at a $p(O_2)$ of 10^{-7} atm, as determined from the coulometric titration results. The area specific resistances (ASR) decrease with Sr doping up to x = 0.75 in $NdBa_{1-x}Sr_xCo_2O_{5+\delta}$ oxides; however, the ASR value of x = 1.0 increases due to its structural change to a simple perovskite system. The best performance of x = 0.5 and/or 0.75 was approximately 1.0 W cm^{-2}, which is clear evidence of a positive effect of Sr in $NdBa_{1-x}Sr_xCo_2O_{5+\delta}$ oxides, and is associated with higher electrical conductivity, fast oxygen transport at the surface, and high catalytic activity for the oxygen reduction reaction. Therefore, x = 0.5 and x = 0.75 in $NdBa_{1-x}Sr_xCo_2O_{5+\delta}$oxides are desirable candidate cathode materials in IT-SOFCs in terms of electrochemical performance.

References

1. Shao, Z. P; Haile, S. M.; A high-performance cathode for the next generation of solid-oxide fuel cells. *Nature* **2004**, *431*, 170-173.
2. Tsai, T.; Perry, E.; Barnett, S.A.; Low-temperature solid-oxide fuel cells utilizing thin bilayer electrolytes, *J. Electrochem. Soc.*, **1997**, *144*, L130-L132.
3. Dusastre, V.; Kilner, J. A.; Optimisation of composite cathodes for intermediate temperature SOFC applications, *Solid State Ionics*, **1999**, *126*, 163-174.
4. Huang, Y. H.; Dass, R. I.; Xing, Z. L; Goodenough, J. B.; Double perovskites as anode materials for solid-oxide fuel cells. *Science* **2006**, *312*, 254-257.
5. Chroneos, A.; Yildiz, B.; Tarancón, A.; Parfitt, D.; Kilner, J.A.; Oxygen diffusion in solid oxide fuel cell cathode and electrolyte materials: mechanistic insights from atomistic simulations, *Energy & Environ. Sci*., **2011**, *4*, 2774-2789.
6. Adler, S.B.; Lane, J.A.; Steele, B.C.H.; Electrode Kinetics of Porous Mixed-Conducting Oxygen Electrodes, *J. Electrochem. Soc*., **1996**, *143*, 3554-3564.
7. Ried, P.; Holtappels, P.; Wichser, A.; Ulrich, A.; Graule, T.; Synthesis and Characterization of $La_{0.6}Sr_{0.4}Co_{0.2}Fe_{0.8}O_{3-\delta}$ and $Ba_{0.5}Sr_{0.5}Co_{0.8}Fe_{0.2}O_{3-\delta}$, *J. Electrochem. Soc*., **2008**, *155*, B1029-B1035.
8. Park, S.; Choi, S.; Shin, J.; Kim, G.; Electrochemical investigation of strontium doping effect on high performance $Pr_{1-x}Sr_xCoO_{3-\delta}$ (x = 0.1, 0.3, 0.5, and 0.7) cathode for intermediate-temperature solid oxide fuel cells, *J. Power Sources*, **2012**, *210*, 172-177.
9. Yoo, S.; Shin, J.; Kim, G.; Comparative characterization of thermodynamic, electrical, and electrochemical properties of $Sm_{0.5}Sr_{0.5}Co_{1-x}Nb_xO_{3-\delta}$ (x = 0, 0.05, and 0.1) as cathode materials in intermediate temperature solid oxide fuel cells, *J. Power Sources*, **2013**, *226*, 1-7.
10. Ishihara, T.; Fukui, S.; Nishiguchi, H.; Takita, Y.; La-Doped $BaCoO_3$ as a Cathode for Intermediate Temperature Solid Oxide Fuel Cells Using a $LaGaO_3$ Base Electrolyte, *J. Electrochem. Soc*. **2002**, *149*, A823-A828.
11. Tai, L.-W.; Nasrallah, M.M.; Anderson, H.U.; Sparlin, D.M.; Sehlin, S.R.; Structure and electrical properties of $La_{1-x}Sr_xCo_{1-y}Fe_yO_3$. Part 2. The system $La_{1-x}Sr_xCo_{0.2}Fe_{0.8}O_3$, *Solid State Ionics*, **1995**, *76*, 273-283.
12. Chen, D; Ran, R.; Zhang, K.; Wang, J.; Shao, Z.; Intermediate-temperature electrochemical performance of a polycrystalline $PrBaCo_2O_{5+\delta}$ cathode on samarium-doped ceria electrolyte, J. Power Sources, **2009**, *188*, 96-105.
13. Taskin, A.A.; Lavrov, A.N.; Ando, Y.; Fast oxygen diffusion in A-site ordered perovskites, *Progress in Solid State Chem*., 2007, 35, 481-490.

14. Kim. J.H.; Cassidy, M.; Irvine, J.T.S.; Bae, J.; Electrochemical Investigation of Composite Cathodes with $SmBa_{0.5}Sr_{0.5}Co_2O_{5+\delta}$ Cathodes for Intermediate Temperature-Opertating Solid Oxide Fuel Cell, *Chem. Mater*., **2010**, *22*, 883-892.
15. Ding, H.; Xue, X.; $PrBa_{0.5}Sr_{0.5}Co_2O_{5+\delta}$ layered perovskite cathode for intermediate temperature solid oxide fuel cells, *Electrochim. Acta*, **2010**, *55*, 3812-3816.
16. Taskin, A.A.; Lavrov, A.N.; Ando, Y.; Achieving fast oxygen diffusion in perovskites by cation ordering, *Appl. Phys. Lett*., **2005**, 86, 090910-090913.
17. Kim, G.; Wang, S.; Jacobson, A. J.; Reimus, L.; Brodersen, P.; Mims, C. A.; Rapid oxygen ion diffusion and surface exchange kinetics in $PrBaCo_2O_{5+x}$ with a perovskite related structure and ordered A cations, *J. Mater. Chem*., **2007**, *17*, 2500-2505.
18. Park, S.; Choi, S.; Kim, J.; Shin, J.; Kim, G.; Strontium Doping Effect on High-Performance $PrBa_{1-x}Sr_xCo_2O_{5+\delta}$ as a Cathode Material for IT-SOFCs, *ECS Electrochem. Lett*., **2012**, *1*, F29-F32.
19. Kim, J.H.; Cassidy, M.; Irvine, J.T.S.; Bae. J.-M.; Advanced Electrochemical Properties of $LnBa_{0.5}Sr_{0.5}Co_2O_{5+\delta}$ (Ln = Pr , Sm, and Gd) as Cathode Materials for IT-SOFC, *J. Electrochem. Soc.*, **2009**, *156*, B682-B689.
20. Chang, A.M.; Skinner, S.J.; Kilner, J.A.; Electrical properties of $GdBaCo_2O_{5+x}$ for ITSOFC applications, *Solid State Ionics*, **2006**, *177*, 2009-2011.
21. McKinlay, A.; Connor, P.; Irvine, J.T.S.; Zhou, W.; Structural Chemistry and Conductivity of a Solid Solution of $YBa_{1-x}Sr_xCo_2O_{5+\delta}$, *J. Phys. Chem. C*, **2007**, *111*, 19120-19125.
22. Kim, J.-H.; Proda, F.; Manthiram, A.; Characterization of $GdBa_{1-x}Sr_xCo_2O_{5+\delta}$ ($0 \leq x \leq 1.0$) Double Perovskites as Cathodes for Solid Oxide Fuel Cells, *J. Electrochem. Soc.* **2008**, *155*, B1023-B1028.
23. Yoo, S.; Shin, J.Y.; Kim, G.; Thermodynamic and Electrical Properties of Layered Perovskite $NdBaCo_{2-x}Fe_xO_{5+\delta}$-YSZ ($x$ = 0, 1) Composites for Intermediate Temperature SOFC Cathodes, J. Electrochem. Soc., **2011**, *158*, B632-B638.
24. Yoo, S.; Choi, S.; Shin, J.Y.; Liu, M.; Kim, G.; Electrical properties, thermodynamic behavior, and defect analysis of $La_{n+1}Ni_nO_{3n+1+\delta}$ infiltrated into YSZ scaffolds as cathodes for intermediate-temperature SOFCs, RSC Advances 2 (2012) 4648-4655.
25. Martin, C.; Mainan, A.; Pelloquin, D.; Nguyn, N.; Raveau, B.; Magnetoresistance in the oxygen deficient $LnBaCo_2O_{5.4}$ (Ln = Eu, Gd) phases, Appl. Phys. Lett., 1997, 71, 1421-1424.
26. Nam, J.H.; Jeon, D.H.; A comprehensive micro-scale model for transport and reaction in intermediate temperature solid oxide fuel cells, Electrochimica Acta, 2006, 51, 3446-3460.

27. Andersson, M.; Yuan, J.; Sundén, B.; Review on modeling development for multiscale chemical reactions coupled transport phenomena in solid oxide fuel cells, *Applied Energy*, **2010**, *87*, 1461-1476.
28. Moon, J.-W.; Masuda, Y.; Seo, W.-S.; Koumoto, K.; Influence of ionic size of rare-earth site on the thermoelectric properties of $RCoO_3$-type perovskite cobalt oxides, *Mater. Sci. Eng. B*, **2001**, *85*, 70-75.
29. Vashook, V. V.; Tolochko, S. P.; Yushkevich, I. I.; Makhnach, L. V.; Kononyuk, I. F.; Altenburg, H.; Hauck. J.; Ullmann, H.; Oxygen nonstoichiometry and electrical conductivity of the solid solutions $La_{2-x}Sr_xNiO_y$ ($0 \leq x \leq 0.4$), *Solid State Ionics*, **1998**, *110*, 245-253.
30. Kröger, F.A.; Vink, H.J.; Relations between the Concentrations of Imperfections in Crystalline Solids, *Solid State Physics*, **1956**, *3*, 307-435.
31. Bastidas, D.M.; Tao, S.; Irvine, J.T.S.; A symmetrical solid oxide fuel cell demonstrating redox stable perovskite electrodes, *J. Mater. Chem.*, **2006**, *16*, 1603-1605.
32. Yoo, S.; Shin, J.; Kim, G.; Thermodynamic and electrical characteristics of $NdBaCo_2O_{5+\delta}$ at varous oxidation and reduction states, *J. Mater. Chem*. **2011**, *21*, 439-443.
33. Adler, S. B.; Factors Governing Oxygen Reduction in Solid Oxide Fuel Cell Cathodes. *Chem. Rev*. **2004**, *104*, 4791-4843.
34. Lu, S.; Meng, X.; Ji, Y.; Fu, C.; Sun, C.; Zhao, H.; Electrochemical performances of $NdBa_{0.5}Sr_{0.5}Co_2O_{5+x}$ as potential cathode material for intermediate-temperature solid oxide fuel cells, *J. Power Sources*, **2010**, *195*, 8094-8096.
35. Kim, J.H.; Irvine, J.T.S.; Characterization of layered perovskite oxides $NdBa_{1-x}Sr_xCo_2O_{5+\delta}$ (x = 0 and 0.5) as cathode materials for IT-SOFC, Int. J. Hydrogen Energy, 2012, 37, 5920-5929.
36. Taracón, A.; Skinner, S. J.; Chater, R. J.; Hernández-Ramírez, F.; Kilner, J. A.; Layered perovskites as promising cathodes for intermediate temperature solid oxide fuel cells, *J. Mater .Chem.*, **2007**, *17*, 3175-3181.

Chapter 9. A New Class of Double Perovskite Cathode for Low Temperature Solid Oxide Fuel Cells

9.1 Introduction

Solid oxide fuel cells (SOFCs) are promising fuel cells offering very high efficiency and long-term stability. To make SOFC technology affordable, however, the operating temperature must be reduced so that much less expensive materials can be used for other cell components and balance of plants[1-10]. The requirement for high operating temperature (800-1000 ^{o}C) of conventional SOFCs, however, leads to notable problems such as high costs and high rate of degradation due to the interactions between cell components during cell fabrication and/or operation. To overcome these problems, researchers have strived to lower the SOFC operating temperature toward an intermediate-temperature (IT) range (500-700 ^{o}C). One of the challenges for IT-SOFCs, however, is to develop cathode materials with sufficiently high electrocatalytic activity for oxygen reduction. Intensive research has thus been carried out to explore alternative cathode materials that achieve superior and stable electrochemical performance.[11-13]

In this regard, mixed ionic and electronic conductors (MIECs) containing Mn, Fe, Co, and/or Ni with the capability to conduct oxygen ions and electrons simultaneously are strong candidates for IT-SOFC cathode materials. Among the various MIEC oxides, perovskite oxides such as (La,Sr)CoO_3[14], (Ba,Sr)$CoFeO_3$[15],(La,Sr)(Co,Fe)O_3[16], and (Sm,Sr)CoO_3[17] have drawn strong interest due to their high electrocatalytic activity for the oxygen reduction reaction (ORR). Co-rich perovskites, however, suffer from poor cell stability under actual operating conditions, although they have shown good electrochemical performance including high electrical conductivity and ORR activity[18,19]. Cell degradation with Co-rich perovskites electrodes possibly originates from the thermal and redox stability issues of the cathode. In terms of stability, the interface between the electrolyte and the cathode of SOFCs is subject to lower $p(O_2)$ under operating conditions, which may cause redox degradation of the cathode and affect the long term stability of the cathode performance. The development of a redox stable cathode would thus mitigate this degradation[20].

Recently, many researchers have focused on $LnBaMO_{5+\delta}$(Ln = Pr, Nd, Sm, and Gd, M = Co, Fe, Ni, Cu, etc.) layered perovskite oxides, based on their much higher chemical diffusion and surface exchange coefficients compared to those of ABO_3-type perovskite oxides. In particular, cobalt containing layered oxides, $PrBaCo_2O_{5+\delta}$(PBCO)[21], offers faster oxygen ion diffusion and surface exchange kinetics, leading to very low area specific resistance (ASR) and good cell performance[22-24].

Our group has extensively studied a class of double perovskite oxides, $NdBaCo_2O_{5+\delta}$(NBCO)[25-29], with the aim of exploiting their high electrical conductivity and high catalytic activity for the ORR. We have found that Sr doping into the Ba site enhanced the electrical conductivity and the ORR, improving

the electrochemical cell performance dramatically. However, some drawbacks such as redox instability and formation of secondary phase, *e.g.*, $BaCO_3$ or $SrCO_3$, arise from the reaction with CO_2 in the atmosphere[30]. In order to enhance redox stability, significant efforts have focused on partial substitution of a transition metal such as Fe, Mn, or Cu into the Co-site to unravel the redox instability of the cathode. However, this sacrifices the outstanding electrical conductivity and the ORR originating from Co-rich perovskites. In addition, for practical application, the chemical stability under CO_2 containing atmospheres also should be considered[31]. In this regard, Lee *et al*.[32] demonstrated dopant segregation occurring from the A-site of a perovskite with different dopants such as Ba, Sr, and Ca. They reported that a smaller size mismatch between the host and dopant cations reduced the segregation level of the dopant, leadingto more stable cathode surfaces. Hence, Ca doping at the A-site of NBCO is anticipated to suppress surface segregation, which is formed as carbonated compounds react with CO_2 from the atmosphere, resulting in better long-term stability of the cathode. There is thus strong motivation to utilize the favorable properties of Co-rich material and higher chemical stability originating from the dopants simultaneously.

In this study, we present excellent electrochemical performance and stability under operating conditions via only Ca doping into the A site of the cation-ordered perovskite structure as a potential cathode material. In addition, we study the effects of Ca doping on electrical properties, oxygen kinetics, redox properties, and morphology for application of $NdBa_{1-x}Ca_xCo_2O_{5+\delta}$ as a superior cathode material for IT-SOFCs.

9.2 Experimental

Synthesis of electrode and electrolyte powders

Cathode materials $NdBa_{1-x}Ca_xCo_2O_{5+\delta}$ (x = 0, 0.25) were synthesized by a glycine-nitrate process (GNP). Stoichiometric amounts of $Nd(NO_3)_3{\cdot}6H_2O$(Aldrich, 99.9%, metal basis), $Ba(NO_3)_2$ (Aldrich, 99+%), $Ca(NO_3)_2{\cdot}4H_2O$ (Alfa Aesar, 99.98%), and $Co(NO_3)_2{\cdot}6H_2O$ (Aldrich, 98+%) were dissolved in distilled water with proper amount of glycine. The solutions were heated up to 350 ºC in air and followed by combustion to form fine powders which were calcined at 600 ºC for 4 hours. The resulting powders were then grinded and calcined again at 900ºC for 4 hours. For the measurement of electrical conductivity and coulometric titration, the powders were pressed into pellets at 5 MPa and sintered in air at 1150 ºC for 12 hours (to achieve relative density > 95%). For transmission electron microscopy (TEM), the $NdBa_{1-x}Ca_xCo_2O_{5+\delta}$ (x = 0, 0.25) sample was annealed at 700 ºC for 1000 hours. For the composite cathode, $NdBa_{1-x}Ca_xCo_2O_{5+\delta}$ (x = 0, 0.25) and $Ce_{0.9}Gd_{0.1}O_{2-\delta}$(GDC) powders were thoroughly mixed together at a weight ratio of 6 : 4 and the mixed powders were blended with an organic binder (Heraeus V006) to form slurries thereafter. The $Ce_{0.9}Gd_{0.1}O_{2-\delta}$(GDC) powders for electrolyte and

NiO-GDC powders for anode were also synthesized by the GNP method. For preparation of cathode slurries, pre-calcined cathode and GDC powders (at a weight ratio of 60:40) were mixed by ball milling, together with an organic binder (Heraeus V006).

Fabrication of fuel cells and TEM sample preparation

Symmetrical cells with a configuration of electrode | GDC | electrode were used for impedance spectroscopy. GDC powder was pressed into pellets of ~1 mm thick and sintered at 1350 ºC for 4 hours in air to obtain a dense electrolyte membrane. Cathode slurries were then painted onto both surfaces of dense GDC electrolyte and fired at 1000 ºC for 4 hours.

Ni-GDC anode-supported cells with a configuration of Ni-GDC | GDC | cathode were fabricated by a drop-coating method. NiO powder, GDC powder, and starch (weight ratio of 6:4:1.5) were mixed by ball milling in ethanol for 24 hours. After drying, the NiO-GDC mixture was pressed into a pellet (~0.6 mm thick and 15 mm diameter). Thin GDC electrolyte membranes were prepared by a refined particle suspension coating technique. A GDC suspension was prepared by dispersing GDC powders (Aldrich) in ethanol with a small amount of binder (polyvinyl Butyral, B-98) and dispersant (Triethanolamine, Alfa Aesar) at a ratio of 1:10. The GDC suspension was applied to a NiO-GDC anode support by drop-coating, followed by drying in air and subsequent co-sintering at 1400 ºC for 5 h.

Cross-sectional samples for TEM analysis were prepared using a focused ion beam (FIB, Quanta 3D, FEI).

Isotope exchange and depth profile for estimation of oxygen tracer diffusivity and surface exchange coefficient

Isotope oxygen exchange was carried out using closed circulation system with >96 % $^{18}O_2$. The concentration of $^{18}O_2$ in gas phase was measured by the mass analyzer (Anelva, M-100-QA-F). The measured samples were polished using diamond paste. 200 mbar of natural abundance O_2 was introduced into the system including a measured sample, and it was heated to measurement temperature. The measured samples were annealed for more than ten times longer than that of isotope oxygen exchanging time[44]. The sample was cooled down to the room temperature, and residual oxygen was r emoved from the system. And then, 200 mbar of $^{18}O_2$ was introduced for oxygen exchange. At the meantime, the sample was heated rapidly to measured temperature. After exchanging time had passed, the sample was quenched to room temperature. Obtained sample was cut into bar shape, and the cut surface was polished by diamond paste. The isotope oxygen diffusion profile was obtained by secondary ion mass spectrometry (SIMS) using ATOMICA 4100 quadrupole-base analyzer, with line-scan mode at the cross section of the sample using xenon ion primary source (Xe^+) at 12.5 keV. The tracer diffusion coefficient (D^*) and the oxygen surface exchange coefficient (k) were estimated by

semi-infinite diffusion model[45]. To obtain the exact *k* values, the depth profile measurement from the exchanged surface was performed with 5 keV Xe^+ primary source, and *k* values were corrected using the real surface concentration of ^{18}O.

Electrical and electrochemical testing

Electrical conductivities of the $NdBa_{1-x}Ca_xCo_2O_{5+\delta}$ (x = 0, 0.25) cathode materials were determined in air using a four-electrode measurement. All four electrodes were made of Ag wire and Ag paste. The current and voltage were controlled/measured using a potentiostat (BioLogic) in the temperature range of 100 to 750 ºC with an interval of 50ºC.

For symmetrical cells, two Ag wires were attached to each of the two electrodes using Ag paste. Each cell was mounted on an alumina tube using a ceramic adhesive (Aremco, Ceramabond 552). Impedance spectra were recorded under OCV in a frequency range of 1 mHz to 500 kHz with ac perturbation of 14 mV in the temperature range of 500-650ºC.

For the single cell tests, each cell was mounted on an alumina tube using a ceramic adhesive. Humidified (with 3 vol% H_2O) H_2 was used as the fuel at a flow rate of 100 mL min^{-1} (passing through a water bubbler at 25ºC), whereas ambient air was supplied to cathode as the oxidant. Impedance spectra and *I-V* polarization curves were obtained with a BioLogic Potentiostat. The *I-V* polarization curves were recorded between 500 ºC and 650 ºC.

Redox property and oxygen nonstoichiometric

The redox property and oxygen nonstoichiometry of $NdBa_{1-x}Ca_xCo_2O_{5+\delta}$ (x = 0, 0.25) cathodes were measured using coulometric titration (CT) as a function of the oxygen partial pressure, $p(O_2)$. The detailed CT procedure is as described elsewhere[29,30]. After purging 5% O_2-Ar gas over the sample in the tube for 24 hours, initial $p(O_2)$ was determined from the OCV. The sample was allowed to equilibrate with the surrounding atmosphere until the change in potential was less than 1 mV h^{-1}. Oxygen nonstoichiometry was determined through this procedure at 650, 700, and 750 ºC over a wide range of oxygen partial pressure. Electrical conductivity was measured simultaneously using a four-electrode configuration and a BioLogic Potentiostat.

Other characterization

X-ray powder diffraction (XRD) (Rigaku diffractometer, Cu Ka radiation) analysis was used to confirm the crystalline structures of samples. In situ XRD was also obtained from room to operating temperature (Bruker, D8 Advance). The microstructures and morphologies of LnBSCF cathode samples were observed using a field emission scanning electron microscope (SEM) (Nova SEM). The TEM images were acquired with JEOL JEM 2100F with a probe forming (STEM) Cs corrector at 200 kV. A

thermogravimetric analysis (TGA) was carried out using a SDT-Q600 (TA instrument, USA). TGA experiments were performed from 100 °C to 900 °C with a heating/cooling rate of 2 °C min^{-1} in air. The room-temperature oxygen content values were determined by iodometric titration.

Computational method

The DFT calculations were performed using the projector augmented wave pseudo potential method[46], as implemented in the Vienna *ab* initio simulation package[47]. Exchange and correlation interactions between electrons were described with the generalized gradient approximation formulated by Perdew, Burke, and Ernzerhof[48]. For all calculations, the kinetic energy cutoff of 600 eV was used for the plane-wave basis and k-point mesh of 8×8×8 used for Brillouin zone integration is generated using the scheme of Monkhorst and Pack. Both the unit cell and atomic positions were fully optimized until the residual forces were less than 10^{-5} eV/Å .

9.3 Results

The ideal double perovskite structure of $NdBaCo_2O_{5+\delta}$ compounds can be generated by the stacking sequence . . .$BaO/CoO_2/NdO_x/CoO_2$. . . , which is closely related to the cuprate superconductors depicted in Fig. 9.1a. Mobile oxygen vacancies are located between the NdO layers and may show highly anisotropic oxygen diffusion depending on directions[21]. Figure 9.1b is a bright-field transmission electron microscopy (BFTEM) image of a NBCaCO particle and corresponding selected area electron diffraction (SAED) pattern. The ED pattern clearly shows weak additional spots, indexed with (001) of a tetragonal super lattice, indicating an ordered structure. To directly observe atom arrangements of ordered NBCaCO, we used high-angle annular dark field (HAADF) scanning transmission electron microscopy (STEM) with a probe-side aberration corrector. Because the contrast in STEM images increases with the atomic number of elements, brighter atoms can be matched with a heavy element (Nd) and darker atoms can be assigned as Ba/Ca atoms, as shown in Fig. 9.1c. This STEM image also confirms A-site ordering by Ca doping. It is remarkable that the compositions of NBCaCO remains unchanged after annealing at 700 °C for 1000 hours, in contrast to other Co-rich perovskites, as seen in energy dispersive spectroscopy (EDS) elemental mapping of Fig. 9.1d.

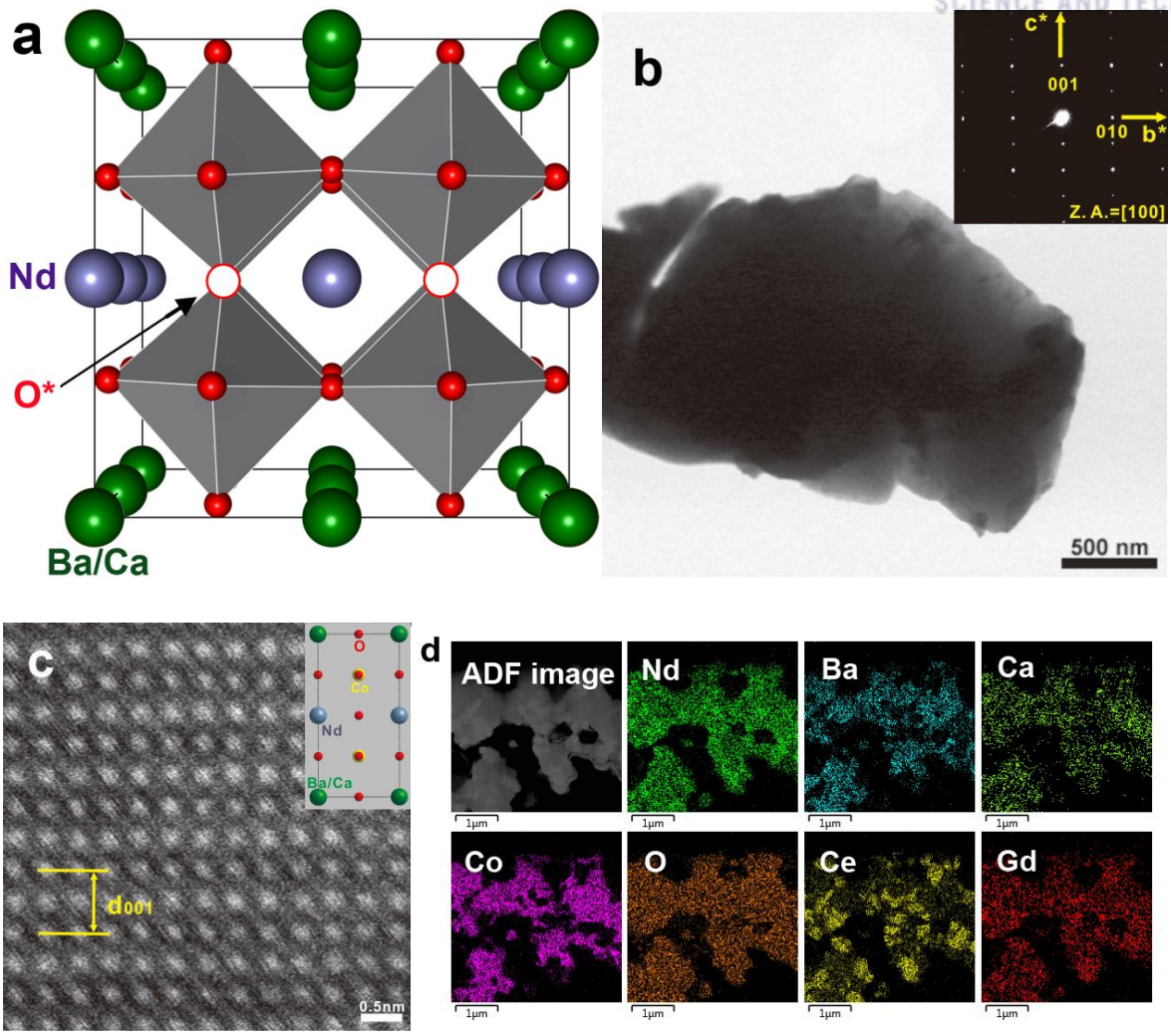

Figure 9.1 The crystal structure andTransmission Electron Microscopy (TEM) analysis a, The crystal structure of $NdBa_{0.75}Ca_{0.25}Co_2O_{5+\delta}$ (NBCaCO) **b**, A BFTEM image and a selected area electron diffraction (SAED) pattern obtained from an as-synthesized NBCaCO sample. **c**, A HAADF STEM image of NBCaCO sample, clearly indicating an ordered structure. **d**, HAADF STEM image of the NBCaCO-GDC composite annealed at 700 ºC for 1000 hours, and EDS elemental mapping of Nd, Ba, Ca, Co, O, Gd, and Ce, with color indicative of the signal intensity.

The development of new cathode materials with high electrocatalytic activity for the oxygen reduction reaction (ORR) is of great importance at intermediate temperature operation. The cathodic reaction involves the reduction of molecular oxygen to oxygen ion, including gas diffusion, surface adsorption, dissociation, charge transfer and so on. In this regard, the impedance spectra for symmetric cells (NBCaCO-GDC|GDC|NBCaCO-GDC) are measured in order to elucidate electrocatalytic activity for ORR by AC impedance spectroscopy at various temperatures in air. As shown in Fig. 9.2a and Fig. 2b,

the ASR values of NBCaCO are dramatically reduced to 0.066 Ωcm^2 at 600 °C compared to that of NBCO (0.091 Ωcm^2). Based on the literature[33-35], the high and intermediate frequencies behavior of impedance are related to ion and electron transfer at the electrode, electrolyte, and collector/electrode interfaces, while the low frequency behavior of impedance is associated with non-charge transfer, such as oxygen surface exchange and gas-phase diffusion inside and outside the electrode layer. Moreover, the large population of mobile oxygen vacancies may contribute to enhanced oxygen kinetics associated with oxygen bulk diffusion and surface exchange[21]. Therefore, higher concentration of mobile oxygen vacancies in the Ln-O layer due to Ca doping may lead to faster oxygen kinetics and better electrochemical performance.

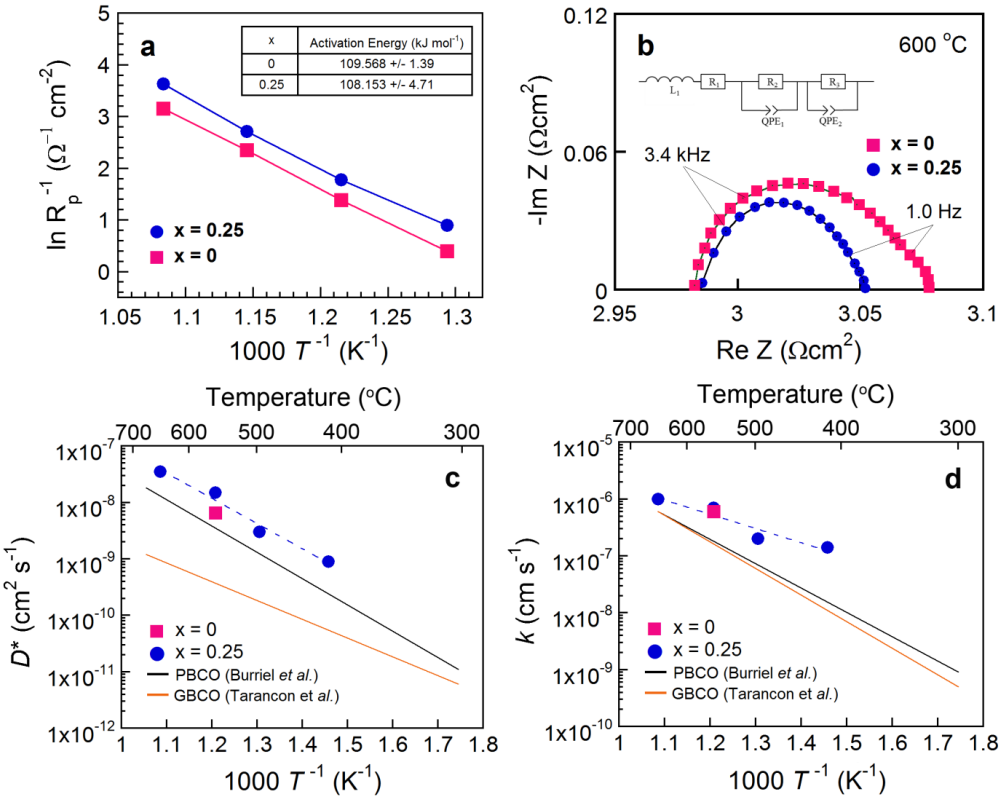

Figure 9.2 The area specific resistance (ASR) and Arrhenius plots of the cathode polarization and the analysis of oxygen diffusion a, Arrhenius plot of reciprocal ASR for $NdBa_{1-x}Ca_xCo_2O_{5+\delta}$($x$ = 0, 0.25)-GDC cathode. **b**, The area specific resistance (ASR) of (a) $NdBa_{1-x}Ca_xCo_2O_{5+\delta}$($x$ = 0, 0.25)-GDC cathodes under open-circuit conditions at 600 °C. **c**, Arrhenius plots of oxygen tracer diffusivity (D*) of $NdBa_{0.75}Ca_{0.25}Co_2O_{5+\delta}$ (NBCaCO) and $NdBaCo_2O_{5+\delta}$(NBCO). **d**, Arrhenius plots of surface oxygen exchange coefficient (k) of NBCaCO and NBCO).

Identification of the surface exchange and oxygen bulk diffusion properties will be helpful in understanding the electrochemical properties required for cathode function. The average oxygen tracer diffusion coefficients of $NdBa_{1-x}Ca_xCo_2O_{5+\delta}$ (x = 0, 0.25) are represented in an Arrhenius plot in Fig. 9.2c for the entire temperature range and compared with the published data in the literature. The measured diffusion coefficients are quite high, ranging from 9.9×10^{-10} to 4.37×10^{-8} $cm^2\ S^{-1}$ at a temperature range from 413 to 648 ℃. These D^* are clearly higher values than those of $PrBaCo_2O_{5+\delta}$ (PBCO) and $GdBaCo_2O_{5+\delta}$ (GBCO) having similar structure[36]. In addition, it can be confirmed that Ca doping imposes a favorable effect on not only electric conductivity but also diffusivity. On the other hands, in the case of the surface exchange coefficients (Fig. 9.2d), the effect of Ca doping does not appear to be substantial. Even though slight changes in surface exchange coefficients with Ca doping, NBCO and NBCaCO exhibits much higher surface exchange coefficients than those of other materials (PBCO and GBCO)[37]. It is thus confirmed that the lower ASR with Ca doping in the NBCO can be partly explained by high oxygen surface exchange and gas-phase diffusion characteristics of NBCaCO.

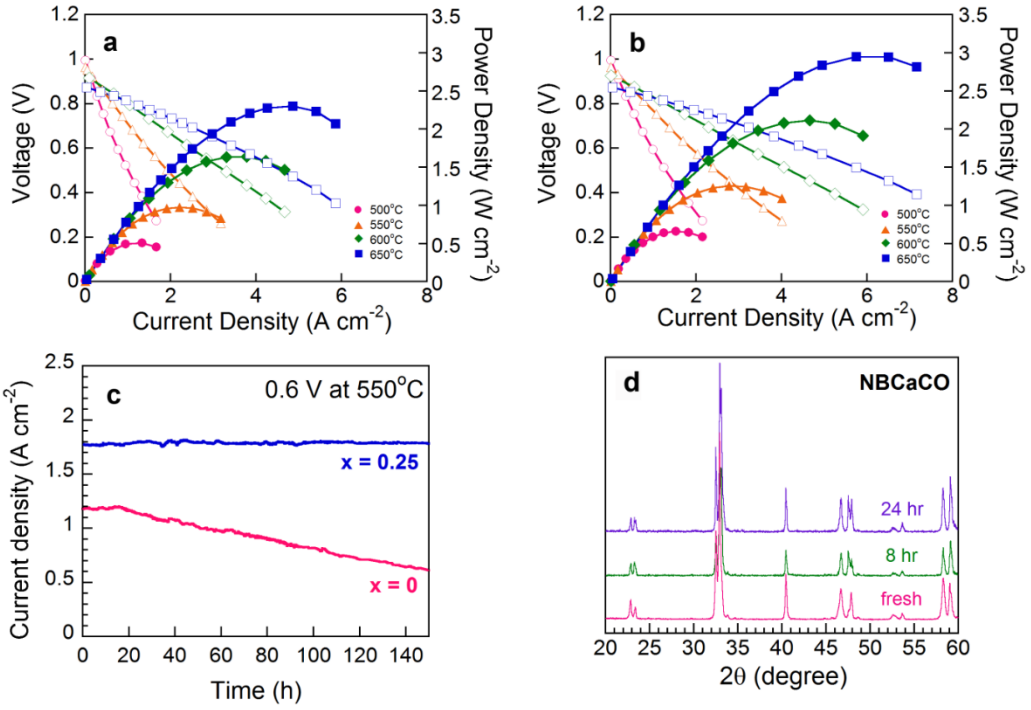

Figure 9.3 Electrochemical performances and long-term stability data of $NdBa_{1-x}Ca_xCo_2O_{5+\delta}$ (x = 0, 0.25) a, *I-V* curves and the corresponding power densities of test cells with NBCO-GDC, **b**, *I-V* curves and the corresponding power densities of test cells with NBCaCO-GDC cathode using humidified H_2 (3% H_2O) as the fuel and ambient air as the oxidant at 500~650 °C. **c**, Long-term stability measurement for a test cell, Ni-GDC | GDC | NBCaCO-GDC, at a constant cell voltage of 0.6 V at 550 °C. **d**, Thermal evolution of the XRD patterns for NBCaCO annealed under CO_2-containing atmosphere at 900 °C for more than 24 hours.

To assess the performance and durability of new NBCaCO cathode materials, the typical single cell performance of the NBCaCO cathodes is measured using a Ni-GDC anode-supported cell based on a ~15 μm thick GDC electrolyte. Fig. 9.3a and Fig. 9.3b present typical *I-V* curves and the corresponding power densities of single cells with NBCO-GDCs and NBCaCO-GDCs as the cathodes at 500-650 ^{o}C, respectively. The peak power densities of the NBCO-GDCs and NBCaCO-GDCs single cells were 1.647 Wcm^{-2}, and 2.114 Wcm^{-2}, respectively, at 600 ^{o}C. The single cell performances are enhanced with Ca doping in NBCO, which can be anticipated from the behavior of the total conductivities and area specific resistance (ASR) with Ca doping.

Stability of SOFC materials is also a key impediment for the commercial success of various intermediate temperature SOFCs, although high power density is still necessary. Regarding the stability issue of a $NdBa_{1-x}Ca_xCo_2O_{5+\delta}$|GDC|Ni-GDC single cell, as shown in Fig. 9.3c, the voltage of NBCaCO-GDCs and NBCO-GDCs single cells was recorded as a function of time under a constant current load of 0.6 V operating in humidified H_2 as the fuel and stationary air as the oxidant at 550 ^{o}C. After operation for 150 hours, the current density of the NBCO single cell decreased dramatically by about 50 %, while that of the NBCaCO-GDCs single cell remained almost constant without observable degradation. The NBCaCO-GDCs single cell was more stable than the NBCO single cell, demonstrating the high potential of NBCaCO as an IT-SOFC cathode material.

Another important aspect for practical applications of Ba-containing perovskite oxides as a cathode in SOFCs concerns the chemical stability under CO_2 containing atmospheres. It is well known that perovskite oxides containing alkaline-earth elements are susceptible to CO_2 attack[38-42]. Degradation of several kinds of perovskites, such as $(Ba,Sr)(Co,Fe)O_{3-\delta}$, $(La,Sr)(Co,Fe)O_{3-\delta}$, has been observed in the presence of CO_2. For example, Yan *et al*. found that the existence even of relatively small quantities of CO_2 can negatively affect the BSCF cathode performance, decreasing the electrochemical reduction of the oxygen and increasing the interface resistance at the same time[30].Thus, the effect of CO_2 on the chemical stability of the NBCaCO cathode in the real reaction environment, *i.e.*, a CO_2 containing atmosphere, was investigated by X-ray diffraction (XRD) measurement. As shown in Fig. 3d, the XRD patterns show that NBCaCO maintains a single phase without any detectable secondary phases after being treated in air containing 10 vol% CO_2 for 24 hours at 900 ^{o}C. Therefore, NBCaCO is suitable for the real reaction environment in terms of chemical stability. Assuming real air with concentrations of CO_2 less than 600 ppm as standard operating conditions for IT-SOFC cathode applications, we can expect excellent stability of NBCaCO in the presence of CO_2 considering the severe fuel cell environment[31].

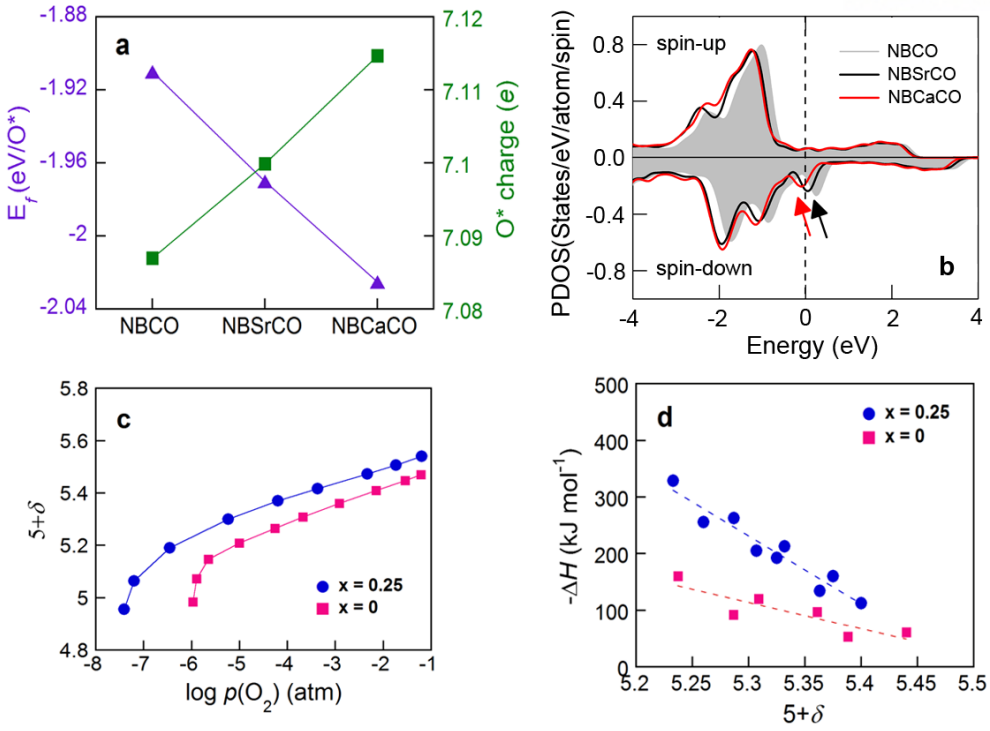

Figure 9.4 **The thermodynamic properties a**, The formation energy E_f (left) and Bader charge (right) of O^* (mobile oxygen vacancies) of NBCO, NBSrCO, and NBCaCO. **b**, PDOS of O^* of NBCO (shaded area), NBSrCO (black/dark line), and NBCaCO (red/light line). The Fermi level is set to zero energy, as denoted by the vertical dashed line. **c**, Oxygen non-stoichiometry of $NdBa_{1-x}Ca_xCo_2O_{5+\delta}$ (x = 0, 0.25) as a function of $p(O_2)$ at 700 °C. **d**, Partial molar enthalpy of oxidation (ΔH) at 700 °C of $NdBa_{1-x}Ca_xCo_2O_{5+\delta}$ (x = 0, 0.25).

In order to predict the stability of mobile oxygen vacancies (O^*) in NBCaCO, we performed first-principles Density Functional Theory (DFT) calculations for the formation energy of O^*, defined as

$$E_f = E_{tot}(\delta = 1) - E_{tot}(\delta = 0) - N \cdot \mu_O \qquad (1)$$

where $E_{tot}(\delta = 1)$ and $E_{tot}(\delta = 0)$ are the total energies of systems with and without O^*, respectively. And N is the number of O^* atoms in the unit cell. μ_O is the chemical potential of an O atom, which is taken as the total energy of an O atom in an isolated O_2 molecule. The calculated formation energy of O^* in NBCaCO is shown in Fig. 9.4(a), and compared to those in NBCO and Sr-doped NBSrCO. It is found that the formation energies are negative for these three systems, and the magnitude increases monotonically from NBCO to NBSrCO to NBCaCO. This indicates that Ca doping for the Ba site leads to better stability for O^* atoms in NBCO.

To further clarify the improved stability of O^* upon Ba site doping, Bader charge analyses for the electronic state of O^* have been carried out; the calculated results are shown as squares in Fig. 9.4(a). A similar trend to that of the formation energy is found; Bader charge increases with doping elements, indicating that O^* atoms accumulate more electrons in the presence of Sr and Ca in NBCO. More detailed analyses can be obtained from the projected density of states (PDOS) in electronic structure calculations, as shown in Fig. 9.4(b). The hybridization between Co 3*d* and O 2*p* orbitals causes spin splitting between the spin subbands, *i.e.*, spin-up and spin-down, in O^* sites. In NBCO, a major peak of the spin-up band is completely occupied, whereas the small spin-down peak is above the Fermi level. The most remarkable change of PDOS upon doping is the downward shift of this spin-down peak, as indicated by arrows in Fig. 9.4(b). The peak of NBSrCO is directly at the Fermi level and that of NBCaCO is just below the Fermi level. Overall, our first-principles calculations show that the enhanced stability of O^* in NBCaCO can be ascribed to the increased electron affinity of O^* of NBCO in the presence of Ca.

While substantial cathode improvements are still necessary to facilitate sufficient power densities for intermediate-temperature SOFCs, an equally important goal is the long-term stability of the cell. For the stability issue, as previously mentioned in the introduction, cathode materials with high redox and thermal stability should be developed for intermediate temperature operation. Under operating conditions, the interface of SOFCs between the electrolyte and the cathode experiences a low $p(O_2)$, which may cause redox degradation of the cathode and affect the long term stability of the cathode performance.[20] If a new electrode material possesses poor redox properties or is decomposed at the fuel cell operating temperature and $p(O_2)$ range, it cannot be used as an electrode. Sufficient electrical conductivity at relatively low $p(O_2)$ is also important to ensure efficient current collection and long-term stability of the cell.

To confirm the redox properties and electrical conductivities at low $p(O_2)$, oxygen nonstoichiometry of the NBCaCO and NBCO samples was investigated as a function of $p(O_2)$ at 700°C (Fig. 9.4c) by coulometric titration. The isotherm of NBCaCO shows a lower $p(O_2)$ for decomposition than that of NBCO, implying that NBCaCO has higher redox stability and sufficient electrical conductivity under cathodic polarization. Its redox properties related to oxygen thermodynamics, such as the oxidation enthalpies and entropies of NBCaCO, are investigated from the results (Fig. 9.4d). The partial molar enthalpy (ΔH) and entropy of oxidation (ΔS) can be calculated from the slopes of the isotherms and related terms such as Gibbs energy. The detailed proofs of related equations have been described elsewhere[25,43]. There are dramatic changes in the oxidation enthalpies according to the extent of reduction.

The values of $-\Delta H$ become lower for a higher oxygen content (δ), implying that lower energy is needed for the evolution of the mobile oxygen vacancies. From this it can be hypothesized that the

lattice structures near the defect sites are destabilized more easily as the oxidation of Co in the lattice proceeds, as shown in Fig. 9.4d. According to the DFT calculation data, the electron affinity of O^* in NBCO is increased after Ca doping, and thus higher O^* stability of NBCaCO is expected. Therefore, through the thermodynamic behaviour, it is also confirmed that NBCaCO is more stable than NBCO, considering its higher oxidation enthalpy near the cathode operating conditions. These results indicate that Ca doping provides favourable properties for practical applications in IT-SOFCs, *i. e.*, higher redox stability of the NBCaCO oxides, which can be a key factor for achieving stable electrochemical properties of a cathode material for viable operation of IT-SOFCs.

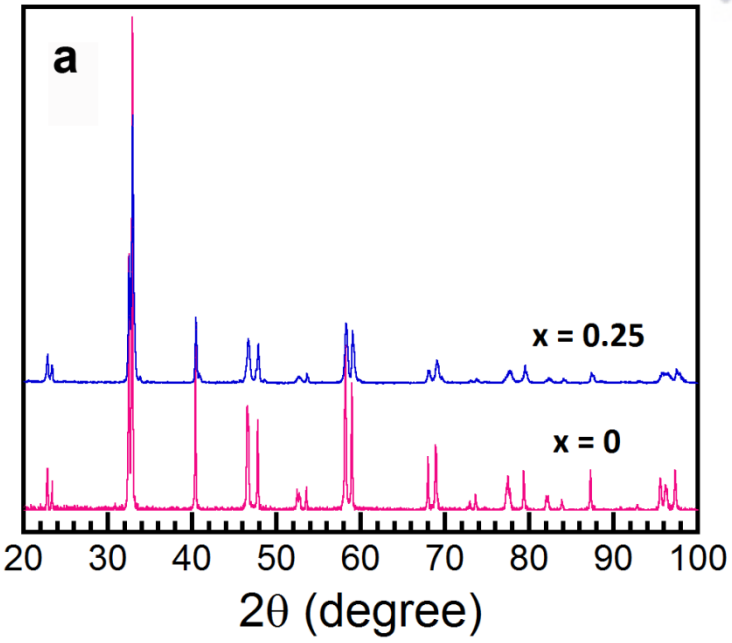

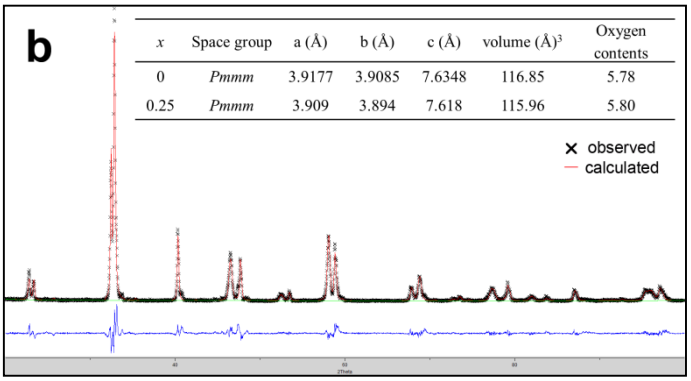

Figure 9.5 (a) X-ray diffraction (XRD) patterns of Ca-doped $NdBa_{1-x}Ca_xCo_2O_{5+\delta}$ (x = 0, 0.25) sample. (b) Rietveld refinement of the data for $NdBa_{0.75}Ca_{0.25}Co_2O_{5+\delta}$.

All samples form a single phase after sintering at 1150 ^oC in air for 12 hours. The XRD patterns were refined using the Rietveld analysis based on the orthorhombic lattice geometry of space group *Pmmm* for all samples. As seen from the data summarized in the inset of Fig.S1b, the unit cell parameter and the volume increase with Ca doped sample due to the replacement of the smaller Ca^{2+} (r = 1.00 Å) ions by the larger Ba^{2+} (r = 1.35 Å) ions.

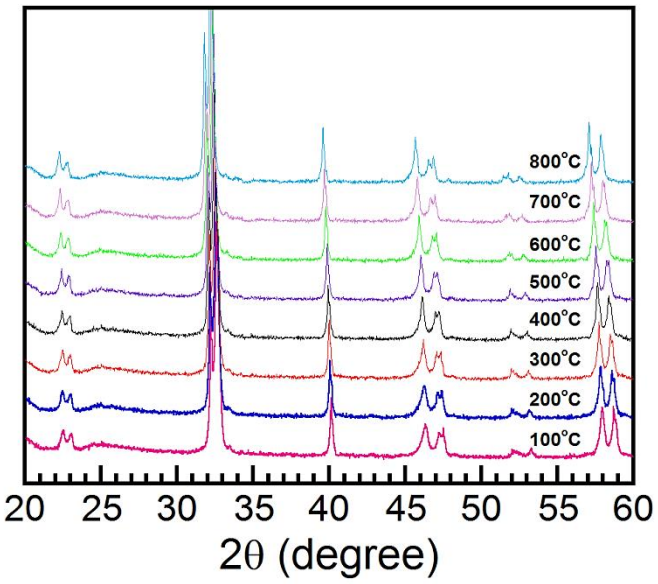

Figure 9.6 In situ X-ray diffraction (XRD) patterns of $NdBa_{0.75}Ca_{0.25}Co_2O_{5+\delta}$

In order to confirm the phase at various temperatures in air, high-temperature XRD measurement was carried out and the results are presented in Fig. S2. The in-situ XRD patterns of the NBCaCO at various temperatures showed that the material retained its double perovskite structure over the temperature range (100 to 800 ^{o}C). High-temperature XRD studies were carried out in air ranging from 100 to 800 ^{o}C with measurements made every 100 ^{o}C.

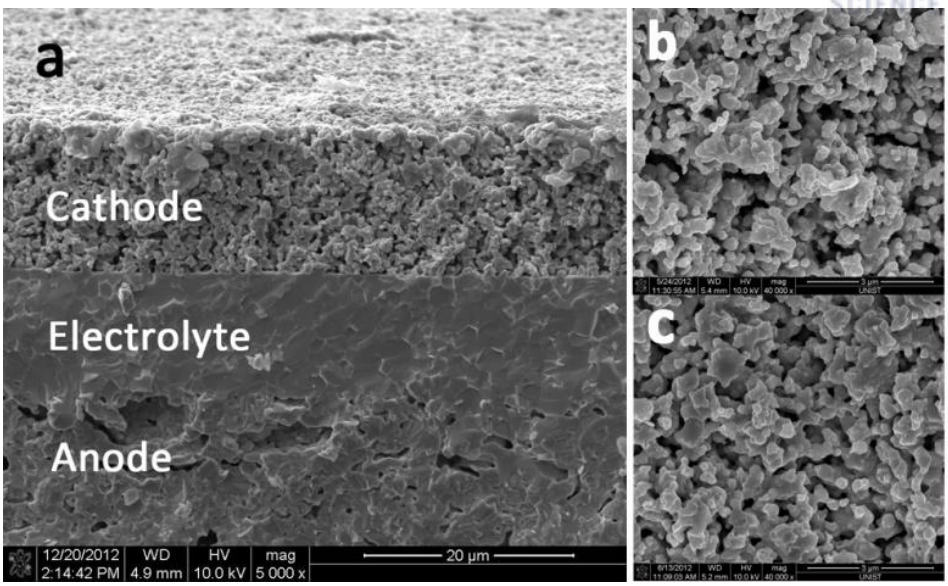

Figure 9.7 Typical microstructure (SEM images) of samples. (a) a cross sectional view of a tri-layer cell with a configuration of Ni-GDC | GDC | $NdBa_{0.75}Ca_{0.25}Co_2O_{5+\delta}$-GDC. The thickness of both the cathode and the GDC electrolyte are ~15 μm. The electrolyte film is dense and free of fabrication flaws (*e.g.*, pinholes, voids, or cracks). Further, the microstructures of the samples seem to be insensitive to the Ca substitution. (b) $NdBaCo_2O_{5+\delta}$ cathode. (c) $NdBa_{0.75}Ca_{0.25}Co_2O_{5+\delta}$ cathode.

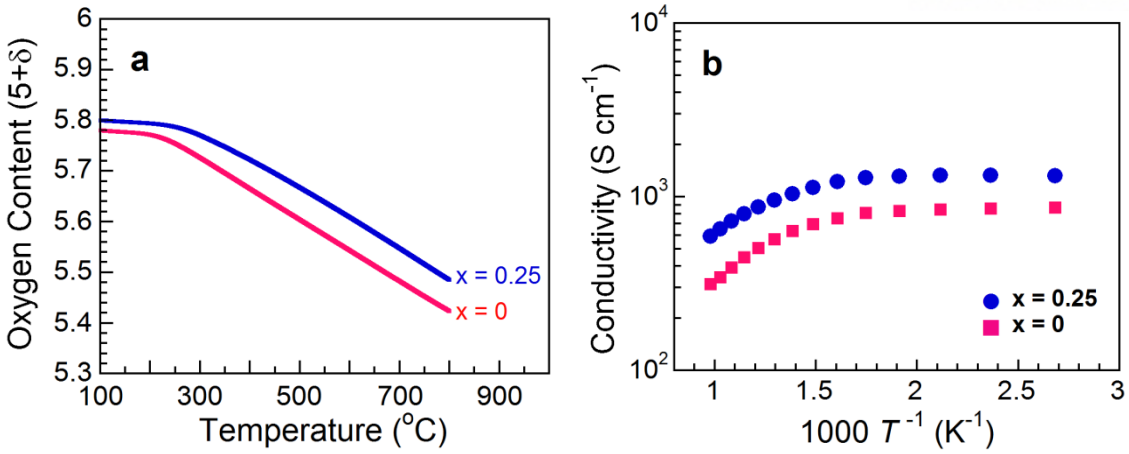

Figure 9.8 The oxygen nonstoichiometry of the $NdBa_{1-x}Ca_xCo_2O_{5+\delta}$ (x = 0, 0.25) as determined using thermogravimetric analysis (TGA) and the electrical conductivities of the $NdBa_{1-x}Ca_xCo_2O_{5+\delta}$ (x = 0, 0.25) samples in air.

The oxygen nonstoichiometry of the Ca-doped $NdBa_{1-x}Ca_xCo_2O_{5+\delta}$ (x = 0, 0.25) samples as a function of temperature in air, as determined using thermogravimetric analysis (TGA). The initial oxygen contents at room temperature are determined by iodometric titration. All samples start to lose the oxygen from the lattice at ~300 °C. The weight loss of the samples increases with Ca doping, possibly due to the loss of mobile oxygen species from the lattice. This can be explained by the increasing coordination number and oxygen content values resulting from the smaller size difference between Nd^{3+} (112 pm) and Ca^{2+} (114 pm) ions compared to that between Nd^{3+} (112 pm) and Ba^{2+} (149 pm) and consequent perturbation of the ordering between the Nd and Ba layers.[49] The high oxygen stoichiometry may be responsible for the high diffusivity of oxide ions in the bulk and the enhanced surface activity toward the ORR.[50]

The electrical conductivity of the $NdBa_{1-x}Ca_xCo_2O_{5+\delta}$ (x = 0, 0.25) is presented in the temperature range of 100 to 750 °C under an air condition. All samples show a decrease in electrical conductivity with increasing temperature, showing metallic behavior over the entire temperature range. Their conductivities start to decrease significantly at about 300 °C due to such as lattice defects breaking the Co-O-Co bonds, resulting in a loss of oxygen atoms from the lattice and reduction of Co^{4+} to Co^{3+}.

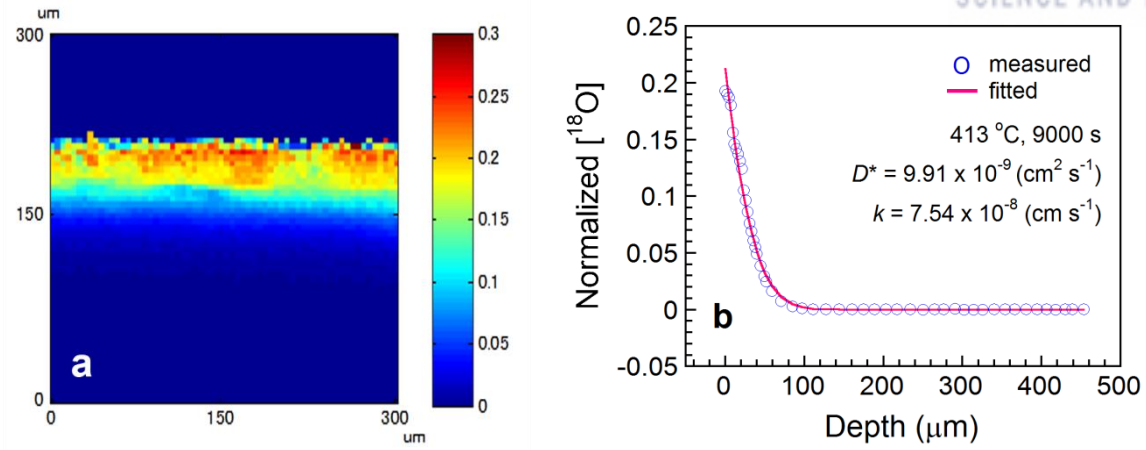

Figure 9.9 Isotope exchange and depth profile for estimation of oxygen tracer diffusivity and surface exchange coefficient: (a) Distribution image of the normalized ^{18}O concentration at the analyzed cross section in exchanged specimen at 413 ^{o}C for 9000 sec. (b) Depth profile of normalized isotope oxygen fraction in $NdBa_{0.75}Ca_{0.25}Co_2O_{5+\delta}$ (NBCaCO) exchanged at 413 ^{o}C for 9000 sec which is obtained by linescan measurement. Symbols and solid line shows the measured results and fitted results, respectively.

Figure (a) shows the distribution image of the normalized ^{18}O concentration in the analyzed cross section in exchanged specimen at 413 ^{o}C. It can be clearly seen how the ^{18}O ions diffuse from the surface of the sample into the bulk. With the image, it can be confirmed the ^{18}O concentration is not completely homogeneous for the whole surface areas measured. The nonuniformity of the ^{18}O distribution suggests that there are areas of the pellet with different surface exchange and oxygen diffusion properties, which could be related to regions with different surface terminations and different grain orientation. By integrating the area of the image along the x direction, the normalized values of the ^{18}O concentration along y for that region can be calculated and fitted to Crank's solution, obtaining the D^* and k fitted values at the exchanged temperature (9.91×10^{-9} cm^2 S^{-1} and 7.4×10^{-8} cm S^{-1}, respectively).

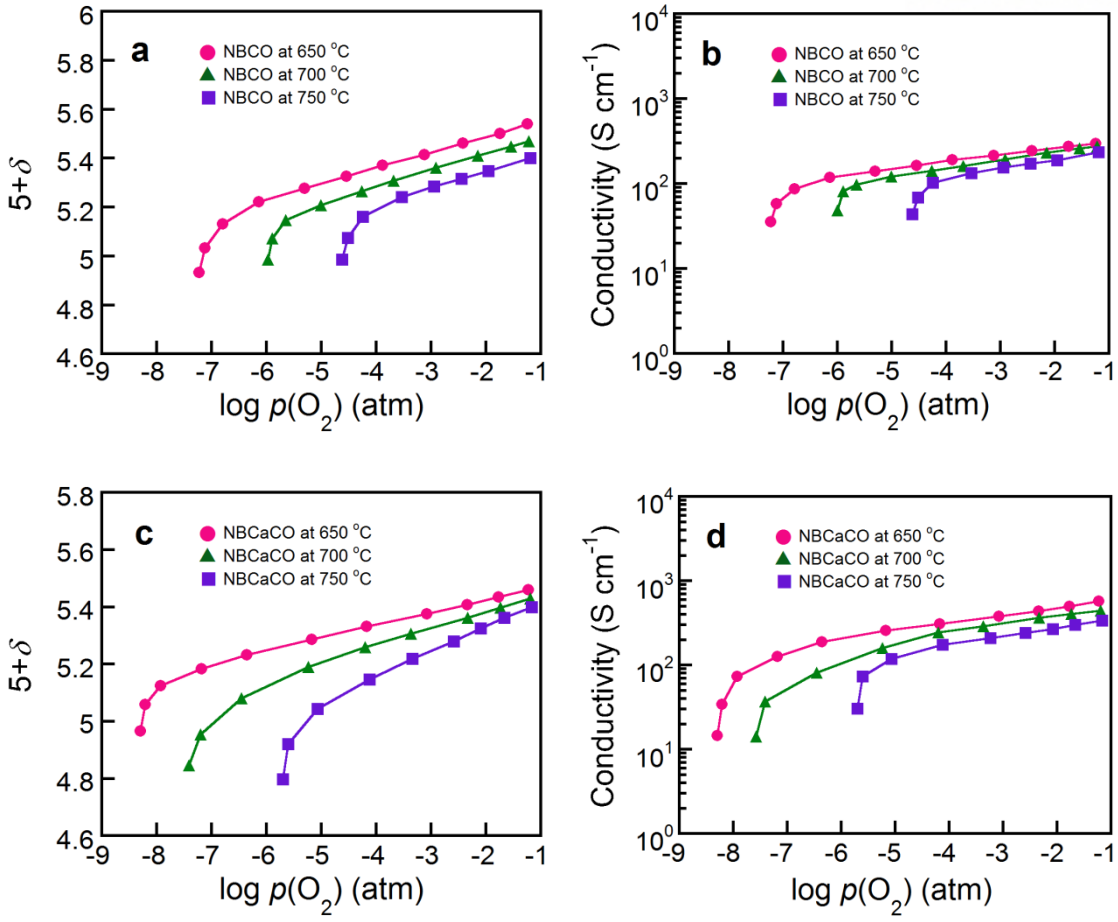

Figure 9.10 The oxygen nonstoichiometries and total conductivities as measured in a wide range of oxygen partial pressure $p(O_2)$ at various temperatures. (a,b) $NdBaCo_2O_{5+\delta}$, (c,d) $NdBa_{0.75}Ca_{0.25}Co_2O_{5+\delta}$. Figures S6(a) and (c) show the oxygen nonstoichiometry of the $NdBa_{1-x}Ca_xCo_2O_{5+\delta}$ (x = 0, 0.25) samples as a function of $p(O_2)$ at various temperatures (650, 700, and 750 °C), as determined using coulometric titration to characterize the redox properties. At 700 °C, $NdBaCo_2O_{5+\delta}$ (NBCO) starts to decompose thoroughly at a $p(O_2)$ of 10^{-6} atm. The decomposition point of NBCaCO samples, however, are lower in $p(O_2)$ than that of NBCO sample, indicating that NBCaCO have higher redox stability and better durability under cathodic polarization. Figure S6(b) and (d) present the total conductivities of $NdBa_{1-x}Ca_xCo_2O_{5+\delta}$ (x = 0, 0.25) samples as a function of $p(O_2)$ at various temperatures. The total conductivities of all samples decrease as $p(O_2)$ is lowered, indicating a typical p-type behavior, due to an increase in oxygen vacancies in the fluorite layers. All conductivities varied from 10 to 10^{-3} S cm^{-1}, which are sufficient for cathode applications under typical operating temperatures.

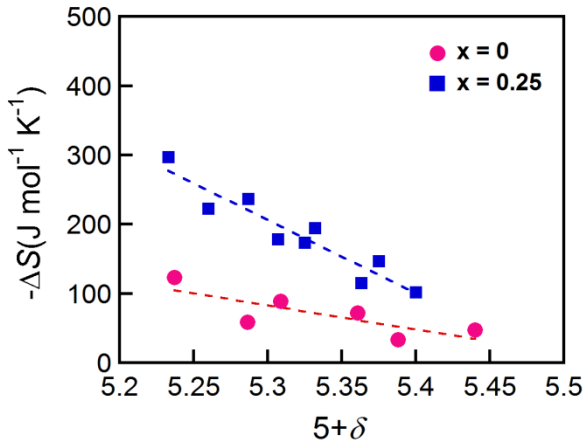

Figure 9.11 Partial molar entropy of oxidation (Δ*S*) at 700 °C of $NdBa_{1-x}Ca_xCo_2O_{5+\delta}$ (*x* = 0, 0.25)

The partial molar enthalpy and entropy of oxidation can be calculated from the slopes of the isotherms. The Gibbs free energy, Δ*G*, is related to the equilibrium constant, *K*, and $p(O_2)$ as follows,

$$\Delta G = -RT\ln K = \frac{1}{2}RT\ln p(O_2)$$

At a constant δ, the partial molar enthalpy of oxidation at various temperatures is shown by the Gibbs-Helmholtz equation.[51]

$$\Delta H = \frac{\partial\left(\frac{\Delta G}{T}\right)}{\partial\left(\frac{1}{T}\right)} = \frac{R}{2}\frac{\partial \ln[p(O_2)]}{\partial\left(1/T\right)}\Bigg|_{\delta}$$

And the partial molar entropy can be obtained by using the Maxwell relation as follows.

$$-\Delta S = \frac{\partial \Delta G}{\partial T} = \left(\frac{R}{2}\right)\left(\frac{\partial\, T\ln[p(O_2)]}{\partial T}\right)\Bigg|_{\delta}$$

The partial molar entropies of oxidation, calculated from the differences in the Gibbs free energies and the enthalpies, are shown in Figure S7. Even though the enthalpy needed for the formation of oxygen mobile vacancies is lower for higher δ, the oxygen mobile vacancies formation reaction itself is suppressed as excess oxygen increases, which is confirmed by the lower entropy at higher δ. In other words, it becomes more difficult for oxygen to exist in the composites as the amount of excess oxygen increases due to the variation of the interaction among randomly distributed defect species.

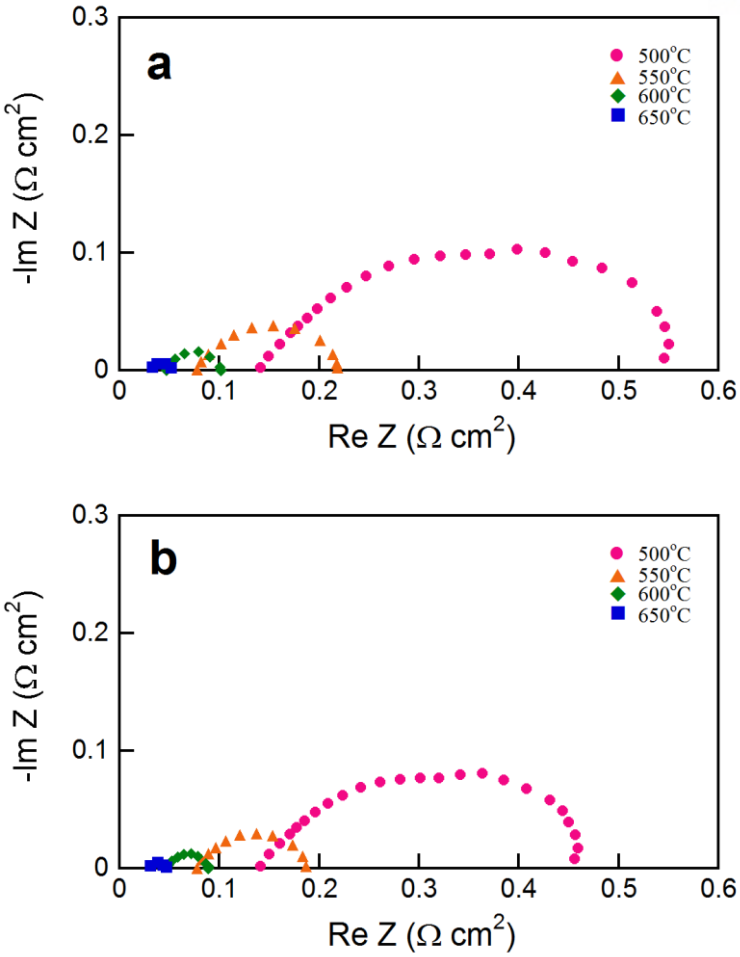

Figure 9.12 EIS spectra of $NdBa_{1-x}Ca_xCo_2O_{5+\delta}$ (x = 0, 0.25) single cell

The electrochemical impedance spectra of NBCO-GDCs/GDC/Ni-GDC and NBCaCO-GDCs/GDC/Ni-GDC single cell corresponding to the *I-V* polarization curve through 500 - 650 ^oC are presented in Fig. S8. In these spectra, the intercepts with the real axis at low frequency designate the total resistance of the cell and the value of high frequency is the ohmic resistance of the cell. The non-ohmic resistance of the cell designating the value between the two intercepts on the real axis determines cell performance associated with oxygen kinetics, such as oxygen diffusion and surface exchange rate. The non-ohmic resistances of the $NdBa_{1-x}Ca_xCo_2O_{5+\delta}$ (x = 0, 0.25) are 0.055, 0.034 Ωcm^2 at 600 ^oC, respectively.

9.4 Conclusion

A class of cation-ordered, double-perovskite compounds display fast oxygen ion diffusion and high catalytic activity toward the ORR at intermediate temperatures while maintaining excellent compatibility with the electrolyte under typical fuel cell operating conditions. The structural characteristics, electrical properties, electrochemical performances, and redox and performance stability of $NdBa_{0.75}Ca_{0.25}Co_2O_{5+\delta}$ (NBCaCO) are investigated with respect to the effects of Ca doping on the Ba site in NBCO and a DFT analysis is carried out to evaluate its cathode material for IT-SOFC applications. The peak power density of the NBCaCO single cell was 2.114 Wcm^{-2} at 600 ºC and the typical cell performance of NBCaCO was very stable at 550 ºC for 150 hours as compared with that of NBCO. The excellent chemical stability of the NBCaCO cathode under the presence of carbon dioxide was also confirmed under real operation conditions. More comprehensive understanding of the mechanistic details may help to envision the design of better double-perovskite cathode materials for a new generation of high-performance SOFCs with enhanced durability.

References

1. Zhan, Z. L.; Barnett, S. A.; An Octane-fueled solid oxide fuel cell. *Science*, **2005**, *308*, 844-847.
2. Liu, M.; Lynch, M.E.; Blinn, K.; Alamgir, F.M.; Choi, Y.M.; Rational SOFC material design: new advances and tools. *Mater. Today*, **2011**, *14*, 534-546.
3. Park, S. D.; Vohs, J. M.; Gorte, R. J.; Direct oxidation of hydrocarbones in a solid- oxide fuel cell. *Nature*, **2000**, *404*, 265-267.
4. Wachsman, E. D.; Lee, K. T.; Lowering the temperature of solid oxide fuel cells. *Science*, **2011**, *334*, 935-939.
5. Xia, C.; Liu. M.; Novel Cathodes for Low-Temperature Solid Oxide Fuel Cells. *Adv. Mater*., **2002**, *14*, 521-523.
6. Yang, L.; Choi, Y.M.; Qin, W.; Chen, H.; Blinn, K.; Liu, M.; Liu, P.; Bai, J.; Tyson, T.A.; Liu, M.; Promotion of water-mediated carbon removal by nanostructured barium oxide/nickel interfaces in solid oxide fuel cells. *Nat. Commun.*, **2011**, *2*, 357-365.
7. Yang, L.; Wang, S.; Blinn, K.; Liu, M.; Liu, Z.; Cheng, Z.; Liu, M.; Enhanced Sulfur and Coking Tolerance of a Mixed Ion Conductor for SOFCs: $BaZr_{0.1}Ce_{0.7}Y_{0.2-x}Yb_xO_{3-\delta}$. *Science*, **2009**, *326*, 126-129.
8. Singhal, S. C.; Advances in solid oxide fuel cell technology. *Soild State Ionics*, **2000**, *135*, 305-313.
9. Huang, Y. H.; Dass, R. I.; Xing, Z. L.; Goodenough, J. B.; Double perovskites as anode materials for solid-oxide fuel cells. *Science*, **2006**, *312*, 254-257.
10. Mogensen, M.; Jensen, K. V.; Jorgensen, M. J.; Primdahl, S.; Progress in understanding SOFC electrodes. *Solid State Ionics*, **2002**, *150*, 123-129.
11. Steele, B. C. H.; Material science and engineering: The enabling technology for the commercialisation of fuel cell systems. *J. Mater. Sci.*, **2001**, *36*, 1053-1068.
12. Horita, T.; Katsuhiko, Y.; Natsuko, S.; Harumi, Y.; André, W.; Ellen, I.-T.; Oxygen reduction mechamism at porous $La_{1-x}Sr_xCoO_{3-\delta}$ cathodes/$La_{0.8}Sr_{0.2}Ga_{0.8}Mg_{0.2}O_{2.8}$ electrolyte interface for solid oxide fuel cells. *Electrochim. Acta* **2001**, *46*, 1837-1845.
13. Adler, S. B.; Factors Governing Oxygen Reduction in Solid Oxide Fuel Cell Cathodes. *Chem. Rev*. **2004**, *104*, 4791-4843.
14. Señarís-Rodríguez, M. A.; Goodenough, J. B.; Magnetic Transport Properties of the System $La_{1-x}Sr_xCoO_{3-\delta}$ ($0 < x \leq 0.50$). *J. Solid State Chem.*, **1995**, *118*, 434-446.
15. Shao, Z. P; Haile, S. M.; A high-performance cathode for the next generation of solid-oxide fuel cells. *Nature* **2004**, *431*, 170-173.
16. Finsterbusch, M.; Lussier, A.; Schaefer, J. A.; Idzerda, Y.U.; Electrochemically driven cation

segregation in the mixed conductor $La_{0.6}Sr_{0.4}Co_{0.2}Fe_{0.8}O_{3-\delta}$. *Solid State Ionics*, **2012**, *212*, 77-80.

17. Xia, C. R.; Rauch, W.; Chen, F.; Liu, M.; $Sm_{0.5}Sr_{0.5}CoO_3$ cathodes for low-temperature SOFCs. *Solid State Ionics*, **2002**, *149*, 11-19.
18. Lv, H.; Wu, Y.; Huang, B.; Zhao, B.; Hu, K.; Structure and electrochemical properties of $Sm_{0.5}Sr_{0.5}Co_{1-x}Fe_xO_{3-\delta}$ cathodes for solid oxide fuel cells, *Solid State Ionics*, **2006**, *177*, 901-906.
19. Lee, S. J.; Muralidharan, P.; Jo, S. H.; Kim, D. K.; Composite cathode for IT-SOFC: Sr-doped lanthanum cuprate Gd-doped ceria, *Electrochem. Comm*., **2010**, *12*, 808-811.
20. Bastidas, D.M.; Tao, S.; Irvine, J.T.S.; A symmetrical solid oxide fuel cell demonstrating redox stable perovskite electrodes, *J. Mater. Chem.*, **2006**, *16*, 1603-1605.
21. Kim, G.; Wang, S.; Jacobson, A. J.; Reimus, L.; Brodersen, P.; Mims, C. A.; Rapid oxygen ion diffusion and surface exchange kinetics in $PrBaCo_2O_{5+x}$ with a perovskite related structure and ordered A cations, *J. Mater. Chem*., **2007**, *17*, 2500-2505.
22. Kim, J.-H.; Manthiram, A.; $LnBaCo_2O_{5+\delta}$ Oxides as Cathodes for Intermediate-Temperature Solid Oxide Fuel Cells, *J. Electrochem. Soc*., **2008**, *155*, *4*, B385-B390.
23. Kim. J.H.; Cassidy, M.; Irvine, J.T.S.; Bae, J.; Electrochemical Investigation of Composite Cathodes with $SmBa_{0.5}Sr_{0.5}Co_2O_{5+\delta}$ Cathodes for Intermediate Temperature-Opertating Solid Oxide Fuel Cell, *Chem. Mater*., **2010**, *22*, 883-892.
24. Chen, D; Ran, R.; Zhang, K.; Wang, J.; Shao, Z.; Intermediate-temperature electrochemical performance of a polycrystalline $PrBaCo_2O_{5+\delta}$ cathode on samarium-doped ceria electrolyte, J. Power Sources, **2009**, *188*, 96-105.
25. Yoo, S.; Shin, J.; Kim, G.; Thermodynamic and electrical characteristics of $NdBaCo_2O_{5+\delta}$ at varous oxidation and reduction states, *J. Mater. Chem*. **2011**, *21*, 439-443.
26. Jun, A.; Kim, J.; Shin, J.; Kim, G.; Optimization of Sr content in layered $SmBa_{1-x}Sr_xCo_2O_{5+\delta}$ perovskite cathodes for intermediate-temperature solid oxide fuel cells, *Int. Hydrogen Energy*, **2012**, *37*, 18381-18388.
27. Park, S.; Choi, S.; Kim, J.; Shin, J.; Kim, G.; Strontium Doping Effect on High-Performance $PrBa_{1-x}Sr_xCo_2O_{5+\delta}$ as a Cathode Material for IT-SOFCs, *ECS Electrochem. Lett*., **2012**, *1*, F29-F32.
28. Yoo, S.; Choi, S.; Kim, J.; Shin, J.; Kim, G.; Investigation of layered perovskite type $NdBa_{1-x}Sr_xCo_2O_{5+\delta}$ (x = 0, 0.25, 0.5, 0.75, and 1.0) cathodes for intermediate-temperature solid oxide fuel cells. *Electrochim. Acta*, **2013**, *100*, 44-50.
29. Choi, S.; Yoo, S.; Kim, J.; Park, S.; Jun, A.; Sengodan, S.; Kim, J.; Shin, J.; Jeong, H.Y.; Choi, Y.M.; Kim, G.; Liu, M.; Highly efficient and robust cathode materials for low-temperature solid oxide fuel cells: $PrBa_{0.5}Sr_{0.5}Co_{2-x}Fe_xO_{5+\delta}$, *Sci. Rep*. **2013**, *3*, 2426-2431.

30. Yan, A.; Vasiliki, M.; Antonino, A.; Cheng, M.; Panagiotis, T.; Investigation of a $Ba_{0.5}Sr_{0.5}Co_{0.8}Fe_{0.2}O_{3-\delta}$ based cathode SOFC II. The effect of CO_2 on the chemical stability. *App. Catal. B: Environmenta.*, **2007**, *76*, 320-327.
31. Tarancón, A.; Peña-Martínez, J.; Marrero-López, D.; Morata, A.; Ruiz-Morales, J.C.; Núñez, P.; Stability, chemical compatibility and electrochemical performance of $GdBaCo_2O_{5+x}$ layered perovskite as a cathode for intermediate temperature solid oxide fuel cells. *Solid State Ionics*, **2008**, *179*, 2372-2378.
32. Lee, W.; Han, J.W.; Chen, Y.; Cai, Z.; Yildiz, B.; Cation Size Mismatch and Charge Interations Drive Dopant Segregation at the Surfaces of Maganite Perovskites. *J. Am. Chem. Soc*. **2013**, *135*, 7909-7925.
33. Adler, S. B.; Lane, J. A.; Steele, B. C. H.; Electrode Kinetics of Porous Mixed-Conducting Oxygen Electrodes. *J. Electrochem. Soc*. **1996**, *143*, 3554-3564.
34. Park, S.; Choi, S.; Shin, J.; Kim. G.; Electrochemical investigation of strontium doping effect on high performance $Pr_{1-x}Sr_xCoO_{3-\delta}$ (x = 0.1, 0.3, 0.5, and 0.7) cathode for intermediate-temperature solid oxide fuel cells. *J. Power Sources*, **2012**, *195*, 172-177.
35. Adler, S. B.; Chen, X. Y.; Wilson, J. R.; Mechanisms and rate laws for oxygen exchange on mixed-conducting oxide surfaces. *J. Catal*. **2007**, *245*, 91-109.
36. Burriel, M.; Peña-Martínez, J.; Chater, R.J.; Fearn, S.; Berenov, A.V.; Skinner, S.J.; Kilner, J.A.; Anisotropic Oxygen Ion Diffusion in Layered $PrBaCo_2O_{5+\delta}$. *Chem. Mater*. **2012**, *24*, 613-621.
37. Taracón, A.; Skinner, S. J.; Chater, R. J.; Hernández-Ramírez, F.; Kilner, J. A.; Layered perovskites as promising cathodes for intermediate temperature solid oxide fuel cells, *J. Mater .Chem.*, **2007**, *17*, 3175-3181.
38. Tofan, C.; Klvana, D.; Kirchnerova. J.; Decomposition of nitric oxide over perovskite oxide catalysis: effect of CO_2, H_2O and CH_4. *Appl. Catal. B*, **2002**, *36*, 311-323.
39. Khromushin, I.V.; Aksenova, T.I.; Zhotabaev, Zh.R.; Mechanism of gas-solid exchange processes for some perovskites. *Solid State Ionics*, **2003**, *162-163*, 37-40.
40. Kharton, V.V.; Yaremchenko, A.A.; Kovalevsky, A.V.; Viskup, A.P.; Naumovich, E.N.; Kerko, P.F.; Perovskite-type oxides for high-temperature oxygen seperation membranes. *J. Membrane Sci*. **1999**, *163*, 307-317.
41. Hibino, T.; Ushiki, K.; Kuwahara, Y.; New concept for simplifying SOFC system. *Solid State Ionics*, **1996**, *91*, 69-74.
42. Carolan, M.F.; Dyer, P.N.; Lavar, J.M.; Thorogood, R.M.; Process for restoring permeance of an oxygen-permeable ion transport membrane utilized to recover oxygen from oxygen-containing gaseous mixtures. *US patent*, **1993**, *5*, 240, 473.

43. Yoo, S.; Choi, S.; Shin, J.Y.; Liu, M.; Kim, G.; Electrical properties, thermodynamic behavior, and defect analysis of $La_{n+1}Ni_nO_{3n+1+\delta}$ infiltrated into YSZ scaffolds as cathodes for intermediate-temperature SOFCs, RSC Advances 2 (2012) 4648-4655.
44. De Souza, R. A.; Chater, R. J.; Oxygen exchange and diffusion mesurements: The importance of extracting the correct initial and boundary conditions. *Solid State Ionics*, **2005**, *176*, 1915-1920.
45. Crank, J.; The Mathematics of Diffusion [2nd ed.] (Oxford Univ. Press, London, **1975**)
46. Blöchl, P. E.; Projector augmented-wave method. *Phys. Rev. B*, **1994**, *50*, 17953–17979.
47. Kresse, G.; Hafner, J.; Ab initio molecular dynamics for liquid metals. *Phys. Rev. B*, **1993**, *47*, RC558–RC561.
48. Perdew, J. P.; Burke, K.; Ernzerhof, M.; Generalized Gradient Approximation Made Simple. *Phys. Rev. Lett*., **1996**, *77*, 3865-3868.
49. Kim, J.-H.; Prado, F.; Manthiram, A.; $GdBa_{1-x}Sr_xCo_2O_{5+\delta}$ $(0 \leqslant x \leqslant 1.0)$ Double Perovskites as Cathodes for Solid Oxide Fuel Cells. *J. Electrochem. Soc*., **2008**, *155*, B1023-B1028.
50. Kim, G.; Wang, S.; Jacobson, A. J.; Reimus, L.; Brodersen, P.; Mims, C. A.; Rapid oxygen ion diffusion and surface exchange kinetics in $PrBaCo_2O_{5+x}$ with a perovskite related structure and ordered A cations, *J. Mater. Chem*., **2007**, *17*, 2500-2505.
51. Nakamura, T.; Yashiro, K.; Sato, K.; Mizusaki, J.; Oxygen nonstoichiometry and defect equilibrium in $La_{2-x}Sr_xNiO_{4+\delta}$, *Solid State Ionics*, **2009**, *180*, 368-376.

List of publications

1. **Seonyoung Yoo**, Areum Jun, Dorj Odkhuu, Young Wan Ju, Junji Hyodo, Hu Young Jeong, Noejung Park, Jeeyoung Shin, Tatsumi Ishihara, Guntae Kim* "A New Class of Double Perovskite Cathode for Low Temperature Solid Oxide Fuel Cells" *Submitted* (2014)
2. **Seonyoung Yoo,** Jiyoun Kim, Seung Yoon Song, Dong Woo Lee, Jeeyoung Shin, Kang Min Ok*, Guntae Kim* "Structural, electrical and electrochemical characteristics of $La_{0.1}Sr_{0.9}Co_{1-x}Nb_xO_{3-\delta}$ as a cathode material for intermediate temperature solid oxide fuel cells" ***RSC Advances*** (2014) 4, 18710
3. Sihyuk Choi, **Seonyoung Yoo**, Jiyoun Kim, Seonhye Park, Areum Jun, Sivaprakash Sengodan, Junyoung Kim, Jeeyoung Shin, Hu Young Jeong, YongMan Choi, Guntae Kim*, Meilin Liu* "Highly efficient and robust cathode materials for low-temperature solid oxide fuel cells: $PrBa_{0.5}Sr_{0.5}Co_{2-x}Fe_xO_{5+\delta}$" ***Scientific Reports*** 3 (2013) 3, 2426
4. **Seonyoung Yoo**, Sihyuk Choi, Junyoung Kim, Jeeyoung Shin, Guntae Kim* "Investigation of layered perovskite type $NdBa_{1-x}Sr_xCo_2O_{5+\delta}$ (x = 0, 0.25, 0.5, 0.75, and 1.0) cathodes for intermediate-temperature solid oxide fuel cells" ***Electrochim. Acta,*** 100, 44-50 (2013)
5. Areum Jun, **Seonyoung Yoo**, Oh-hun Gwon, Jeeyoung Shin, Guntae Kim* "Thermodynamic and electrical properties of $Ba_{0.5}Sr_{0.5}Co_{0.8}Fe_{0.2}O_{3-\delta}$ and $La_{0.6}Sr_{0.4}Co_{0.2}Fe_{0.8}O_{3-\delta}$ for intermediate-temperature solid oxide fuel cells" ***Electrochim. Acta***, 89, 372-376 (2013)
6. **Seonyoung Yoo**, Tak-Hyoung Lim, Jeeyoung Shin, Guntae Kim* "Comparative characterization of thermodynamic, electrical, and electrochemical properties of $Sm_{0.5}Sr_{0.5}Co_{1-x}Nb_xO_{3-\delta}$ (x = 0, 0.05, 0.1) as cathode materials in intermediate temperature solid oxide fuel cells" ***J. Power Sources***, 226, 1-7 (2013)
7. **Seonyoung Yoo**, Sihyuk Choi, Jeeyoung Shin, Meilin Liu, Guntae Kim* "Electrical Properties, Thermodynamic Behavior, and Defect Analysis of $La_{n+1}Ni_nO_{3n+1+\delta}$ Infiltrated into YSZ Scaffolds as Cathodes for Intermediate-Temperature SOFCs" ***RSC Advances***, 2, 4648-4655 (2012)
8. Sihyuk Choi, **Seonyoung Yoo**, Jeeyoung Shin, and Guntae Kim* "High Performance SOFC Cathode Prepared by Infiltration of of $La_{n+1}Ni_nO_{3n+1}$ (n = 1, 2, and 3) in Porous YSZ" ***J. Electrochem. Soc***. 158 (8), B995-B999 (2011)
9. **Seonyoung Yoo**, Jee Young Shin, and Guntae Kim* "Thermodynamic and Electrical Properties of Layered Perovskite $NdBaCo_{2-x}Fe_xO_{5+\delta}$-YSZ ($x$ = 0, 1) Composites for Intermediate Temperature SOFC Cathodes" ***J. Electrochem.Soc.***, 158(6) B632-B638 (2011)
10. **Seonyoung Yoo**, Jee Young Shin and Guntae Kim* "Thermodynamic and electrical characteristics of $NdBaCo_2O_{5+\delta}$ at various oxidation and reduction states" ***J. Mater. Chem.***, 21, 439-443 (2011)

Acknowledgement

I would like to express my deepest gratitude to my advisor, Professor Guntae Kim, for giving me the opportunity generous support, encouragement with patience, and guidance for my research work. Without his commitment this dissertation would not have had the present quality and consistency.

I would also like to thank my committee members Professor Hyun-Kon Song, Professor Soojin Park, Professor Jinyoung Kim, and Professor Jong Shik Chung for their valuable time and thoughtful insight. I was so inspired from their advice based on their expertise and theoretical basics and learned the topic of electrochemistry relevant to my research field.
I am truly grateful to Professor Jeeyoung Shin for his constant inspiration and help given to me during the course of my doctoral study. Prof. Shin always reviewed my tenuous research papers for pointing out misconception and giving critical and valuable comments to me. Absolutely, he have been my great co-supervisors in the PhD study.

I wish to special thanks to our group members of "**gunslab**", who helped me during the course of doctoral study: Sivaprakash Sengodan, Sihyuk Choi, Areum Jun, Seonhye Park, Junyoung Kim, Oh-hun Gwon, Seona Kim, Oh-hoon Kwon, and Changmin Kim. Studying for years would have been impossible without them. I wish you all the best for your work and would be always be happy to hear good news.

Last, but foremost, I would like to appreciate my parents, my sister, and all of my familiy for their endless love, understanding, and support.